Dynamics of correlations and entanglement in cold atomic gases

Youssef Trifa

THÈSE

en vue de l'obtention du grade de

Docteur
délivré par l'École Normale Supérieure de Lyon

Discipline : **Physique**

Laboratoire de physique de l'ENS de Lyon

École Doctorale N°52 Physique et Astrophysique de Lyon

Présentée et soutenue publiquement le 2 juillet 2024
par **Youssef TRIFA**

Dynamiques de correlations et d'intrication dans des gaz d'atomes froids

---

Devant le jury composé de :

M. Luis SANTOS	*Professeur* Leibniz Universität Hannover	Rapporteur
Mme. Alice SINATRA	*Professeure* LKB	Rapportrice
M. Sylvain NASCIMBENE	*Professeur* LKB	Examinateur
M. Johannes SCHACHENMAYER	*Chargé de recherche-HDR* CESQ	Examinateur
Mme. Emilia WITKOWSKA	*Professeure* Polish Academy of Sciences	Examinatrice
M. Tommaso ROSCILDE	*Maître de conférences-HDR* LPENSL	Directeur de thèse

Remerciements

Cette thèse est l'aboutissement de plusieurs années d'études et de travail à l'ENS de Lyon, et n'aurait pas pu voir le jour sans l'aide et le soutien de toutes les personnes que j'ai pu cottoyer pendant toutes ces années.

Tout d'abord, je souhaiterais remercier mon encadrant, Tommaso, pour sa direction, qui m'a permis découvrir un sujet qui était nouveau pour moi et m'a aidé à en apprendre davantage sur les systèmes de grands spins. Mais surtout, je voudrais remercier Tommaso pour son écoute, sa bonne humeur et son enthousiasme à tout épreuve, même dans les périodes où rien ne semblait marcher. Son soutien a été fondamental dans la réalisation de cette thèse.

Plus généralement, je voudrais remercier l'ensemble du laboratoire de physique, en particulier mes cobureaux, les doctorants et post doc de l'équipe 4, le groupe de 11h45, le CMSWM qui est ensuite devenu le TSWM, l'esnemble des chercheurs et chercheuses, ainsi que les gestionnaires, Laurence et Erika. C'est grâce à toutes ces personnes que le laboratoire de physique est un endroit aussi agréable pour y faire une thèse, et j'ai vraiment apprécié les années que j'y ai passées en tant que doctorant.

Au delà de la thèse, l'ENS est également un endroit où j'ai passé beaucoup de temps, notamment via les différentes activités associatives que j'ai pu mener, et grâce auxquelles j'ai pu rencontrer des personnes merveilleuses. Je ne pense pas que j'arriverai à citer tout le monde ici, mais je pense à toutes les personnes que j'ai pu rencontrer au BuL (ou dans les clubs qui le composaient avant sa formation), à ConférENS, à l'impro, au club Headbang, ou simplement au Foyer ou en amphi pour mes cours. Je pense à particulier à mes colocs, mes colocs par alliance, Solène pour tous ces memes sur le doctorat, mes coauteurices préféré · es, Bastien et Solène, ainsi que mes ami · es de lycée ou de prépa que j'ai eu l'occasion de recroiser à Lyon ou ailleurs ces dernières années et toutes celleux qui m'ont permis de me rappeler que l'important, c'est l'essentiel.

Je voudrais également remercier toute ma famille, mes frères, mes parents, mes cousins, mes oncles et tantes, dont ma marraine, mes grands-parents, grands-oncles et grandes tantes pour leur soutien inconditionnel pendant toutes ces années et pour m'avoir supporté (dans tous les sens du terme !).

Enfin, comment ne pas remercier Marlysa, pour tout son amour au quotidien et pour tous ces moments partagés ces dernières années. Merci d'être la personne que tu es, et c'est à mon tour de te souhaiter plein de courage et de bonnes choses pour ta thèse qui va bientôt commencer, et que, j'en suis certain, tu réussiras aussi brillamment.

Abstract:
The quantum many-body problem, and especially the study of dynamical properties of a multipartite quantum system, is one of the hardest problems of modern physics. There exist only a few analytical results and exact numerical simulations require an amount of resources that grow exponentially with the system size.

In this thesis, we studied correlations and entanglement properties for systems composed of magnetic atoms on a lattice, for instance via the generation of spin squeezing. For this purpose we have developed new approximate numerical methods that allow us to study large system sizes. This enabled us to propose protocols to generate an amount of spin squeezing that scales with the system size. The advantage is twofold. Since spin squeezing is an entanglement witness, this would allow for entanglement detection in a system of magnetic atoms - which has yet to be realized experimentally. Moreover, spin squeezing offers an important metrological advantage, as spin-squeezed states can be used for extremely precise measurements of external magnetic fields, far beyond what one can achieve with independent atoms.

Finally, we studied the generation of other forms of entanglement, namely Dicke squeezing (of spin or momentum), in systems of Bose-condensed atoms. This form of entanglement is well-known in spin-1 atomic condensates. Here, we propose a protocol to generalize it to the case of momentum modes, using a time-dependent Hamiltonian. The entangled states generated during the dynamics are potentially useful for the precision measurements of inertial forces.

Résumé :
Le problème quantique à N corps, notamment l'étude des propriétés dynamiques d'un système quantique composite est l'un des problèmes les plus durs de la physique moderne, car il y a peu de résultats analytiques et les méthodes numériques exactes requièrent des ressources numériques exponentielles en la taille du système.

Dans cette thèse, nous avons étudié la mise en évidence de propriétés de corrélations et d'intrication pour des systèmes d'atomes magnétiques sur réseau, par exemple via la compression de spin. Pour cela nous avons mis au point de nouvelles méthodes numériques approchées, qui permettent de simuler des systèmes de grande taille. Cela nous a permis de proposer des protocoles qui permettent de générer de la compression de spin qui croit d'autant plus que le système est grand, ce qui a un double intérêt. D'une part, il s'agit d'un témoin d'intrication, qui permettrait donc de détecter de l'intrication dans un système d'atomes magnétiques, ce qui n'a pas encore été réalisée expérimentalement à ce jour. D'autre part la compression de spin présente un important intérêt métrologique, puisque les états comprimés permettent des mesures extrêmement précises de champs magnétiques par exemple, bien au-delà de ce qui est possible avec des atomes indépendants.

Enfin, nous avons étudié la génération d'autres formes d'intrication, à savoir la compression à deux modes (de spin, ou d'impulsion), cette fois pour des systèmes d'atomes condensés. Connue dans le cas de condensats d'atomes de spin-1, nous avons proposé comment généraliser ce processus au cas de compression en impulsion, en utilisant un Hamiltonien modulé dans le temps. Les états intriqués ainsi produits sont potentiellement très intéressants dans la mesure à haute précision de forces inertielles.

Contents

Introduction

The quantum many-body problem, and especially the study of dynamical properties of a multipartite quantum system, is one of the hardest problems of modern physics. There exist only a few analytical results and exact numerical simulations require an amount of resources that grow exponentially with the system size. Indeed, one of the properties of quantum mechanical systems as opposed to classical one is that the state of a quantum system is described by a number of parameters exponential in the system size, while it is linear in the system size for a classical system. This is due to a famous property of quantum mechanical states, namely superposition. This phenomenon is at the origin of the richness of quantum mechanical states and properties, such as entanglement. This complexity has for long been a major obstacle to study large quantum systems, yet recent developments both in the experimental techniques and in numerical and theoretical methods open new perspectives to study quantum many-body systems in a controlled way. An especially promising arena is that of ultracold atoms, which represent the main source of inspiration for our research work.

In this context, this thesis focuses on the study of dynamical properties of large-S spin systems, related to the properties of ultracold atoms in optical lattices. In this thesis, we will use exact numerical methods, as well as new approximate theoretical approaches, to investigate the build up of correlations and entanglement in spin systems and multi-mode bosonic systems. An important part of this thesis will be dedicated to the presentation of these new theoretical approaches as well as their benchmark versus exact methods. We will discuss the potential use of the states generated in the dynamics for metrological applications, and in particular for precision measurement of magnetic fields or inertial forces. Finally, we propose realistic protocols, suitable for current experimental platforms, to be implemented in future experiments in order to realize highly entangled states.

The organization of the present thesis is the following:

1. In Chapter 1, we introduce the key theoretical notions to study the physical properties of many-body quantum systems. In particular, we present the notion of entanglement and discuss different manner to characterize and detect it as well as its importance for the field of metrology. We also discuss the time evolution of quantum systems and the link with self-thermalization within the framework of the Eigenstate Thermalization Hypothesis. We review different existing numerical methods, both exact and approximate, that are widely used to study the quantum many-body problem, and discuss their strengths and limitations.

2. In Chapter 2, we discuss the specific case of quantum systems made of large-S spins. We

introduce some key notions to investigate the properties of these systems. In particular, we present two Hamiltonians realized by spin systems, the general One-Axis-Twisting Hamiltonian, and the more specific dipolar XXZ Hamiltonian for magnetic atoms. In the case of the OAT Hamiltonian, we review the known results on its dynamics starting from a coherent spin state. Finally, we review recent experimental realization of the dipolar XXZ Hamiltonian using magnetic atoms.

3. In Chapter 3, we study in more details the dynamics induced by the dipolar XXZ Hamiltonian, starting from a coherent initial state for magnetic atoms pinned on a 1D lattice. We start by investigating the case with only $N = 2$ spins, where we can derive exact results and reproduce exactly the OAT Hamiltonian presented in the previous chapter. We then move to larger numbers N of spins and discuss the persistence of dynamical properties obtained in the $N = 2$ case when increasing N.

4. In Chapter 4 we present the main results of this thesis. Introducing two numerical methods, based on an approximate separation of variables and on a truncated cumulant expansion, we are able to study the dynamics of the dipolar XXZ Hamiltonian for very large 1D chains and 2D square lattices. In particular, we show that in the case of a 2D square lattice and starting with a uniform coherent spin state, it is possible to generate spin squeezing in a scalable manner with the atom number N, which offers a clear metrological advantage compared to independent atoms. In particular the scheme based on the separation of variables allows us to reinterpret the results obtained in the previous chapter. We also investigate the equilibrium state properties of the dipolar XXZ Hamiltonian using both a mean-field approach as well as quantum Monte Carlo. Finally, we discuss the link between the dynamical properties of the system (in particular the presence of scalable squeezing) and the thermodynamic properties of the system - namely the existence of long-range ferromagnetic order in the xy plane at finite temperature.

5. Finally, in Chapter 5, we study another form of spin squeezing, namely Dicke squeezing, that can be generated from spin-exchange collisions in a spinor condensate. This form of entanglement is well-known in spin-1 atomic condensates, and we first review the main properties of the dynamics in that case, starting with a condensate of spins in the individual state $m = 0$. Then, we propose a protocol to generalize this entangling dynamics to the case of momentum modes, using a time-dependent Hamiltonian. The entangled states generated during the dynamics are potentially interesting for the high-precision measurement of inertial forces.

Chapter 1

Many-body quantum dynamics

In this first chapter, we introduce some key theoretical notions concerning many-body quantum systems. In section 1.1, we review important properties of quantum mechanical states, from entanglement to out-of equilibrium dynamics. In section 1.2, we present numerical methods to study these properties.

1.1 Quantum many-body physics and entanglement

The quantum many-body problem can be generically formulated as the problem of solving the dynamics of a quantum system composed of a large number of degrees of freedom. As such, it represents one of the hardest problems in physics. A most challenging part of this problem is to predict the evolution of a system after a quantum quench, i.e. the evolution following the preparation of the system in a state which is not a Hamiltonian eigenstate.

1.1.1 Information in a quantum state

The way a quantum state is represented is radically different from the way a classical state is represented. Let us take for instance a chain of spin-$\frac{1}{2}$ spins. At the single-spin level, a classical state would just contain the information of the spin being in the state $\uparrow$ or $\downarrow$, and can be stored using a single bit. A quantum state, on the contrary, is already a superposition of the two possible outcomes and it takes a complex number α to express the quantum state $(|\uparrow\rangle + \alpha|\downarrow\rangle)/\sqrt{(1+|\alpha|^2)}$ of the spin. Depending on the precision one wants, it can correspond to 2 floating numbers, e.g. each with 64 bits. In the language of quantum computation, this is what we call a qubit, and it is already clear at this level that a qubit can store more information than a classical bit.

However, the real difference between classical and quantum arises when looking at the many-body state of the system. In the classical case, the state of N spins is simply expressed by the state of all the individual spins $(\sigma_1, \sigma_2, ...\sigma_N)$ where the σ_i all take values in $\uparrow, \downarrow$, and hence it contains only N classical bits of information. Note that there exist 2^N such classical states. On the other hand, a generic quantum many-body state can not in general be expressed as a tensor product of N independent single-spin states, but it is a complex linear combination of all the possible basis states, which requires 2^N complex numbers to be specified. The main difference between classical and quantum information therefore lies in this huge difference in

scaling with system size. Whereas it is possible to simulate classical systems of millions of particles by using conventional (i.e. classical) computers, it is impossible to simulate exactly the quantum state of more than ≈ 30 quantum $S = \frac{1}{2}$ spins because of the exponential scaling of the quantum information contained in the state. This is one of the main motivations towards quantum simulation [1]: developing experimental platforms that could simulate the dynamics of quantum systems with resources that would not increase exponentially with system size. This would allow one to explore the possibility to scale quantum properties such as entanglement to increasingly large systems; and to possibly address the question about the existence of a quantum-to-classical crossover.

1.1.2 Entanglement and metrology

Separability and entanglement. In terms of mathematical structure, the many-body Hilbert space where the many-body quantum state lives is simply obtained as a tensor product of the single-body Hilbert spaces, for each degree of freedom. This gives rise to an exponential scaling of the Hilbert space dimension with the number of components in the system. The fundamental trait that makes the Hilbert space of N quantum particles astronomically more complex than the phase space of N classical particles is entanglement, stemming from many-body quantum superpositions [2]. Before defining what is entanglement, one must first define what entanglement is not, namely separability. A pure many-body quantum state is said to be separable if it can be written as a tensor product of individual states for the subsystems, namely:

$$|\Psi\rangle = |\psi_1\rangle \otimes |\psi_2\rangle \otimes ... \otimes |\psi_N\rangle. \tag{1.1}$$

With this definition, it is clear that there are no correlations between the different subsystems, and the variance of any collective observable would only be the sum of the variances of individual observables. On the contrary, a state that is not separable is said to be entangled. A typical example of an entangled state in the case of two spins $S = \frac{1}{2}$ is a Bell state such as $\frac{|\uparrow\uparrow\rangle+|\downarrow\downarrow\rangle}{\sqrt{2}}$. This definition can be extended to density matrices. A quantum state is said to be separable if its density matrix can be written as a mixture of product states:

$$\rho = \sum_k p_k \rho_1^{(k)} \otimes \rho_2^{(k)} \otimes ... \otimes \rho_N^{(k)}, \quad \sum_k p_k = 1 \tag{1.2}$$

and is entangled otherwise. Note that for a pure state $|\psi\rangle$, the density matrix is simply $\rho = |\psi\rangle\langle\psi|$.

Entanglement is apparently defined in a negative manner, but in fact one can derive criteria asserting that a given state is entangled. Such entanglement criteria are based on inequalities that are satisfied by all separable states [3]. The violation of such an inequality immediately implies that the state is entangled. Note that this is always a sufficient condition for entanglement, but not a necessary one : a state could be entangled without violating a given inequality. We will give in subsection 2.1.3 an example of such a criterion based on spin squeezing.

Von Neumann and Renyi entanglement entropy. In order to determine the degree of entanglement of a pure quantum state, we often consider a bipartition of the system, by cutting it into two parts A and B. We can then compute the bipartite entanglement of the system, via the Von Neumann entropy of the reduced state:

$$\mathcal{S}_A = -\mathrm{Tr}\left(\rho_A \log \rho_A\right) \tag{1.3}$$

where $\rho_A = \mathrm{Tr}_B \rho_{AB}$ is the partial trace over subsystem B of the full density matrix. In the case of a pure separable state, the density matrix ρ_A is simply $|\psi_A\rangle\langle\psi_A|$, therefore $\mathcal{S}_A$ (and similarly $\mathcal{S}_B$) are equal to zero because ρ_A and ρ_B are just projectors. In order to obtain a general expression for $\mathcal{S}_A$, we can use the Schmidt decomposition of the state $|\psi_{AB}\rangle$:

$$|\psi_{AB}\rangle = \sum_i \alpha_i |u_i\rangle \otimes |v_i\rangle \tag{1.4}$$

where $|u_i\rangle$ and $|v_i\rangle$ are two orthogonal bases for the subsystems A and B diagonalizing the respective reduced density matrices ρ_A and ρ_B, and $\sum_i |\alpha_i|^2 = 1$. In this formalism, the entanglement entropy simply rewrites as:

$$\mathcal{S}_A = -\sum_i |\alpha_i|^2 \log |\alpha_i|^2. \tag{1.5}$$

With this expression, it is easier to see that the entanglement entropy is the same for subsystems A and B. Moreover, we can now clearly see that to maximise this value, one must take all the α_i's equal to $\frac{1}{\sqrt{n}}$ where n is the minimal Hilbert space dimension between the two reduced Hilbert spaces of the two subsystems:

$$|\psi_{AB}^{\max}\rangle = \sum_{i=1}^{n} \frac{1}{\sqrt{n}} |u_i\rangle \otimes |v_i\rangle. \tag{1.6}$$

In that case, the entanglement entropy is equal to $\log n$.

There exist other definitions of entanglement entropy, based on the Rényi entropies, $\mathcal{S}_\alpha$, which are defined in the following way:

$$\mathcal{S}_\alpha(\rho_A) = \frac{1}{1-\alpha} \log\left(\mathrm{Tr}\left(\rho_A^\alpha\right)\right) = \mathcal{S}_\alpha(\rho_B). \tag{1.7}$$

Note that the Von Neumann entropy corresponds to the Rényi entropy for $\alpha = 1$. Entanglement entropies quantify bipartite entanglement of a pure quantum state, but they remain somewhat abstract in the absence of tangible consequences on the physics of the system. In this respect, an important consequence of entanglement is that quantum states can be put to use for some tasks much more efficiently than separate states. Talking about the "usefulness" of entanglement leads one to introduce different forms of certification with respect to entanglement entropies, focused on the multipartite nature of entanglement rather than on its bipartite one. A particularly effective framework in this respect is the one of quantum metrology [4, 5]

Quantum metrology. Quantum metrology explores the fundamental limits imposed by quantum mechanics on the estimation of external fields applied to a system which is subject to measurements. In this respect, a central goal of quantum metrology is to identify states of the system, and measurement protocols, which are most effective at the estimation task.

In this thesis we will focus on a specific, yet very important metrological task, which is the estimation of the parameter of a unitary transformation via interferometry. Consider for instance an unknown magnetic field B along a given axis z, that one wants to estimate. This magnetic field couples to the collective spin J^z. This leads to a unitary evolution of the quantum state with an operator $U = e^{iBJ^z t} = e^{-i\theta J^z}$ where we defined $\theta = -Bt$ the rotation angle. The

Quantum Cramér-Rao bound [6] establishes that the lowest uncertainty on the estimate of θ one can obtain with a given quantum state ρ is bounded from below by:

$$(\delta\theta)^2 \geq \frac{1}{\mathcal{F}(\rho, J^z)} \tag{1.8}$$

where $\mathcal{F}(\rho, J^z)$ is the so-called quantum Fisher information associated with the state ρ and for rotations around J^z. For a pure quantum state $\rho = |\psi\rangle\langle\psi|$, we have the following property:

$$\mathcal{F}(|\psi\rangle, J^z) = 4\mathrm{Var}(J^z) \tag{1.9}$$

with $\mathrm{Var}(J^z) = \langle\psi|(J^z)^2|\psi\rangle - \langle\psi|J^z|\psi\rangle^2$. Therefore, the larger $\mathrm{Var}(J^z)$, the better the estimation will be.

For an individual spin $\frac{1}{2}$, $J^z = S^z$, and one of the states that maximize the variance of S^z is simply the eigenstate of S^x:

$$|x\rangle = \frac{|\uparrow\rangle + |\downarrow\rangle}{\sqrt{2}}. \tag{1.10}$$

The variance is then $\mathrm{Var}(S^z) = \frac{1}{4}$ since $(S^z)^2 = \frac{1}{4}Id$ and $\langle x|S^z|x\rangle = 0$.

Let us now move to the case of N spins, by looking at first to the case of a factorized state. If we take such a state, it can be written as a product of the states of the N spins: $|\psi\rangle = \otimes_{i=1}^{N}|\psi_i\rangle$. We then have the following inequality:

$$4\mathrm{Var}(J^z) = 4\sum_{i=1}^{N}\mathrm{Var}(S_i^z) \leq N. \tag{1.11}$$

Therefore, for a factorized state, the maximum variance is obtained for a product state of N single-spin states similar to Eq. 1.10, and it is proportional to N. Going back to the estimation problem, this leads to a phase uncertainty:

$$\delta\theta \geq \frac{1}{\sqrt{N}} \tag{1.12}$$

which is known as the Standard Quantum Limit (SQL).

However, it is possible to decrease this uncertainty by moving to entangled states. Indeed, the state that maximises the variance of J^z is the so-called GHZ state or cat state:

$$|\psi_{cat,N}\rangle = \frac{|\uparrow,...,\uparrow\rangle + e^{i\phi}|\downarrow,...,\downarrow\rangle}{\sqrt{2}} \tag{1.13}$$

where $|\uparrow,...\uparrow\rangle$ ($|\downarrow,...,\downarrow\rangle$) is the tensor product of N spins in the state $|\uparrow\rangle$ ($|\downarrow\rangle$). It is easy to prove that $4\mathrm{Var}(J^z) = N^2$. In that case the variance is proportional to N^2, and it leads to the so called Heisenberg limit of metrology, related to the best possible estimate:

$$\delta\theta \geq \frac{1}{N}. \tag{1.14}$$

Note that the cat state is far from being a maximally entangled state in the sense of the Von Neumann entanglement entropy (here for any bipartition $\mathcal{S}^{\mathrm{VN}} = \log 2$ instead of $\frac{N}{2}\log 2$). It is also worth mentioning that the variance of the collective spin acts as an entanglement criterion for a pure state, as any factorized state must verify $\mathrm{Var}(J^z) \leq N/4$.

1.1.3 Out-of-equilibrium dynamics

One of the questions that quantum simulation aims to tackle is understanding the out-of-equilibrium dynamics of quantum systems. A relevant example of such dynamics is offered by quantum quenches, corresponding to the unitary evolution of a quantum state governed by a time-independent Hamiltonian of which the state is not an eigenstate. In this context a fundamental question arises : does the system relax to a stationary regime of dynamics, and does this regime correspond to thermal equilibrium? In short, does the unitary dynamics lead to "thermalization"?

Eigenstate thermalisation hypothesis. In order to answer the above questions, the established theoretical framework is known as the Eigenstate Thermalisation Hypothesis (ETH) [7]. Let us consider a Hamiltonian $\mathcal{H}$, with eigenstates $|\lambda\rangle$ and eigenvalues E_λ. Let us define an initial state:

$$|\psi\left(0\right)\rangle = \sum_\lambda c_\lambda |\lambda\rangle. \tag{1.15}$$

Then the evolved state at time t is given by

$$|\psi\left(t\right)\rangle = U\left(t\right)|\psi\left(0\right)\rangle = e^{-it\mathcal{H}}|\psi\left(0\right)\rangle = \sum_\lambda c_\lambda e^{-itE_\lambda}|\lambda\rangle \tag{1.16}$$

where we have set $\hbar = 1$ (as we will do in the following of this thesis). We are interested at the time evolution of an observable $\hat{O}$, which can be expressed in the eigenbasis of $\mathcal{H}$ as:

$$\hat{O} = \sum_{\lambda,\mu} O_{\lambda\mu}|\lambda\rangle\langle\mu|. \tag{1.17}$$

Without loss of generality, the time evolution of the mean value of $\hat{O}$ is then given by:

$$\begin{aligned}
\langle\hat{O}\rangle\left(t\right) &= \langle\psi\left(t\right)|\hat{O}|\psi\left(t\right)\rangle \\
&= \sum_\lambda c_\lambda^* e^{+itE_\lambda}\langle\lambda|\sum_{\lambda',\mu'} O_{\lambda'\mu'}|\lambda'\rangle\langle\mu'|\sum_\mu c_\mu e^{-itE_\mu}|\mu\rangle \\
&= \sum_{\lambda,\mu} O_{\lambda\mu}c_\lambda^* c_\mu e^{+it(E_\lambda - E_\mu)} \\
&= \sum_\lambda O_{\lambda\lambda}|c_\lambda|^2 + \sum_{\lambda\neq\mu} O_{\lambda\mu}c_\lambda^* c_\mu e^{+it(E_\lambda - E_\mu)}.
\end{aligned} \tag{1.18}$$

Let us consider the case of a system for which energy is the only conserved quantity in the dynamics. For the observable $\hat{O}$ to thermalize, its time average has to converge (after some relaxation time) to the value predicted by the canonical ensemble $\langle\hat{O}\rangle_T$ (or the microcanonical ensemble, by equivalence between the different ensembles):

$$\langle\hat{O}\rangle_T = \frac{\mathrm{Tr}\left(e^{-\mathcal{H}/T}\hat{O}\right)}{\mathrm{Tr}\left(e^{-\mathcal{H}/T}\right)} \tag{1.19}$$

with the temperature T adjusted so as to match the thermal energy to the energy of the initial state:

$$\langle\psi\left(0\right)|\mathcal{H}|\psi\left(0\right)\rangle = E = \frac{\mathrm{Tr}\left(e^{-\mathcal{H}/T}\mathcal{H}\right)}{\mathrm{Tr}\left(e^{-\mathcal{H}/T}\right)}. \tag{1.20}$$

T is often called the quench temperature.

This is a priori not straightforward, since the first term in Eq. 1.18 (that should converge to $\langle \hat{O} \rangle_T$) depends on the initial state, and the second term could not vanish due to really close energy levels. However, if the observable matrix elements verify the following ansatz [8]:

$$O_{\mu,\nu} = O\left(\bar{E}\right)\delta_{\mu,\nu} + e^{-S\left(\bar{E}\right)/2} f_O\left(\bar{E}, \omega\right) R_{\mu,\nu} \tag{1.21}$$

then one can show that the observable $\hat{O}$ does thermalize in the sense defined earlier [7]. Here, $\bar{E} = (E_\mu + E_\nu)/2$, $\bar{\omega} = (E_\mu - E_\nu)/2$ and $S\left(\bar{E}\right)$ is the thermodynamic entropy. Finally, $O\left(\bar{E}\right)$ and $f_O\left(\bar{E}, \omega\right)$ must be smooth functions of their arguments, and $R_{\mu,\nu}$ is a random variable with zero mean value and unit variance. Eq. 1.21 is what is often referred as the ETH, and it provides a concrete scenario by which a quantum system, through its own unitary evolution, can relax toward an equilibrium. The next is question one has to ask is then: how general is this hypothesis? And to what kind of systems does it apply?

Typicality vs. violations of ETH. Before considering states of systems that violate the ETH, let us study the case of a typical system that will satisfy the ETH. Let us first consider a local quantum many-body Hamiltonian on a lattice (which is the case of the Hamiltonians we will study in chapters 3 and 4). We define a bipartition A/B of the whole system, and we compute the associated Von Neumann entanglement entropy for each eigenstate of the Hamiltonian. If we do so, we will find two very different scaling behaviours with the size of the subsystem A. In the case of the ground state (or the most excited state), the entanglement entropy exhibit a so-called "area-law" [9], which means that $\mathcal{S}_A$ scales with the area of A. For instance, in the case of 1D systems, it implies an entanglement entropy independent of the size of A. However, if we take a typical excited state (whose energy sits in the middle of the spectrum), then the entanglement entropy will scale as the volume of subsystem A, this is the so-called "volume-law" scaling of the entanglement entropy. A typical state is therefore expected to have an important entanglement entropy, but also an important thermodynamic entropy, which eliminate the off-diagonal term in Eq. 1.21. In fact, it is possible to show that in the case of a typical ergodic system, the two entropies are equivalent [10]. We can now consider the case of an initial state, with energy E_0, which is not an eigenstate of the Hamiltonian, but that has an important overlap with eigenstates at energy around E_0. If all those states have similar entropy, we expect that the expectation value of any observable with respect to the long time unitary evolved state will depend only on its initial energy E_0 as stated by the ETH.

However, there can exist eigenstates of the Hamiltonian, with an energy that sits in the middle of the spectrum, but that exhibit area-law scaling of the Von Neumann entropy (and similarly a low thermodynamic entropy, as for the ground state). These states are called quantum many-body scars, and the expectation value of observables for these states can be very different from the one for other typical states at similar energy. If now our initial state has an important overlap with a quantum many-body scarred state, then its long-time evolution will violate the ETH [11]. Note that this is considered to be a weak violation of the ETH, as only a few eigenstates of the Hamiltonian escape ergodicity. There exists other form of weak ETH violation, such as Hilbert space fragmentation [11, 12], or even stronger violations (quantum many-body localisation [13], integrable models [14]) but we will not review them in details in this manuscript.

1.2 Numerical and theoretical methods for quantum many-body physics

Several numerical and theoretical methods have been developed in the past decades to study the equilibrium and out-of-equilibrium dynamics of quantum systems. In this subsection, we list and briefly describe some of the most successful ones, and in particular those which are relevant for this thesis.

Exact diagonalization. The most straightforward way to study the time evolution of a quantum system is to diagonalize the full Hamiltonian [15]. This is an exact method, which can be applied to any kind of system provided that it is sufficiently small. Indeed, the complexity of this method scales as d^3 for a Hilbert space of dimension d. Since the dimension of the Hilbert space scales exponentially with the number of individual subsystems, it is limited to $\sim O(20)$ $S = 1/2$ spins for instance. A way to push further this method is to diagonalize only partially the Hamiltonian, using a reduced, adaptative basis built from the Krylov space at each time step. This procedure is known as the Lanczos algorithm [16, 17].

Truncated cumulant expansion. This method relies on assumptions on the properties of the time-evolved observables rather than the evolved quantum state. Here, it corresponds to assuming that all high-order correlation functions can be written as a product of cumulant functions of order $n \leq n_0$ [18–22]. For instance, in the case of bosons, one can take $n_0 = 2$ and consider only Gaussian wavefunctions, for which any correlation function satisfies Wick's theorem - i.e. any high order correlation function can be expressed as a product of second-order correlation functions. This allows one to build a close set of coupled differential equations that can be solved easily. In the case of spins, however, we have no guarantee that the evolved state remains Gaussian at all times, which is often not the case for interacting Hamiltonian. Hence deviations from the exact solution will increase in time as the higher order cumulants build up in the exact solution. This limits this method to short time dynamics. We will give more details on this method in chapter 4, section 4.2.

Quantum Monte Carlo. This name refers to several different methods, that all have in common the fact they apply the Monte Carlo sampling technique to study the quantum many-body problem [23–25]. Theses methods can be numerically exact, especially when dealing with bosons, or approximate if coupled with variational approaches. Monte Carlo methods can be used to compute ground states and zero temperature properties of a system (e.g. with Variational Monte Carlo [25]), finite temperature and thermodynamics properties of a system (e.g. with Path Integral Monte Carlo), and even real-time dynamics properties for closed systems (e.g. with Time dependent variational Monte Carlo). In this thesis, we used QMC simulations to determine the thermodynamics of spin models (see chapter 4, section 4.3 for more details).

Spin-wave theory. This method is based on the transformation of local spin operators into local bosonic operators. We will give examples of spin-to-boson transformations in section 2.1.4. We then introduce the spin-wave operators as the Fourier transform of the local bosonic operators. Starting from a coherent spin state - i.e. a classical spin state in the limit $S \to \infty$ -

the spin waves describe the first quantum corrections to the classical limit. At first order, one can keep only quadratic terms in the Hamiltonian, which amounts to describe the excitations from the initial state as a gas of non-interacting bosonic quasi-particles. This is known as the linear spin-wave theory [26, 27]. However it is possible to generalize this method by keeping higher order terms in the Hamiltonian, leading to interactions between these quasiparticles [28]. These corrections are important in the case of high energy quenches for instance, as linear spin-wave theory is limited to small deviations from the initial state.

All these numerical methods offer a complementary approach to the quantum many-body problem, as they can capture different aspects of the quantum dynamics. This is one of the reasons why in this thesis we used all these numerical methods to obtain the results shown in the next chapters. However, it is worth mentioning other methods we did not use in this work, but that have been extensively developed in the past years. In particular, we can evoke the case of variationnal ansatze. These methods rely on reducing the total Hilbert space to a family of wavefunctions dependent on a few parameters, and then describe the time evolution of the system through the time evolution of this parameters [29]. It is quite a powerful method, however it relies on an uncontrolled approximation, that is that there exist at all time a variational state that has an important overlap with the exact evolved state of the system. It is therefore an approximate method that needs to be benchmarked against other numerically exact methods. Among the variationnal ansatze we can cite the Matrix Product States [30], which is very effective at describing the properties of 1D systems and some 2D systems [31]. However this method suffers from important limitations in the case of higher-dimensional systems of for systems with a large local Hilbert space, which are the subject of this thesis.

The second method worth mentioning is the Discrete Truncated Wigner Approximation (DTWA), that sample the quantum noise at the level of the initial state, and then reconstruct the state of the system at time t by averaging over several classical trajectories. This method has been generalized to the case of large-S spins under the name of Generalized DTWA (GDTWA) [32], and it will be interesting to implement this approach and compare its predictions to other numerical methods as part of future work.

While several of these numerical methods are still more precise than experiments (as they do not suffer from various sources of noise), they are still limited in system size. We are now at a threshold where future experimental platforms for quantum simulation might go beyond current numerical methods (at least in terms of system size). Thus it appears that future developments in the field will require close collaboration between experimental and numerical improvements. We will discuss more in details in subsection 2.3.2 the recent experimental developments in the field of quantum simulation with magnetic atoms.

Chapter 2

Dynamics of large-S spin systems

In this chapter, we introduce theoretical concepts to study the physics of large-S spins, we discuss quantum simulation with atoms and we depict the state of the art of the current experimental platforms. In section 2.1, we introduce the physics of large-S spins and give some insight into the properties of different families of large-S spin states. In section 2.2, we discuss a paradigmatic spin Hamiltonian for this work, namely the so-called one-axis twisting Hamiltonian. We show how it can produce relevant entangled state for metrology during the dynamics, and we discuss a few experimental realisations of this Hamiltonian. Finally, in section 2.3, we introduce the dipolar Hamiltonian that governs the dynamics of magnetic atoms. This is the Hamiltonian we will thoroughly study in chapters 3 and 4. We also review some state-of-the-art experiments using this platform and we discuss future challenges in this field.

2.1 Large-S spin physics

Most of the present experimental platforms for quantum simulation realize ensembles of interacting qubits, i.e. $S = 1/2$ spin systems, possessing the smallest possible local Hilbert space. Qubit systems can realize universal models of quantum computation [33], and therefore already allow in principle for the realization of arbitrary quantum states for arbitrary degrees of freedom – in which groups of qubits can be thought of realizing higher-dimensional objects.

However, working directly with qudits [34], i.e. elementary degrees of freedom with a higher-dimensional Hilbert space, offers several advantages, both fundamental as well as practical. Systems of qudits are naturally realized in experiments using e.g. photonic platforms [35]; molecular magnets [36]; and ensembles of large-S magnetic atoms [37]. N qudits can obviously encode an exponentially larger amount of quantum information than N qubits; entangled states of qudits can be more resilient to noise than entangled states of qubits [35]; and using qudits as quantum sensors [38] instead of qubits can be very advantageous, in that single qudits already possess highly non-classical states with increased sensitivity to unitary transformations. The latter aspect also hints at a very intriguing competition that qudit systems (unlike qubit ones) can exhibit between single-qudit non-classical states and many-qudit non-classical (i.e. entangled) states.

2.1.1 Spin algebra

The physics of systems with $S = \frac{1}{2}$ spins has been largely studied both experimentally and theoretically. In fact, it is one of the simplest examples to study and understand quantum properties and effects, and especially the physics of two-level systems which are of utmost importance for quantum information.

The dynamics of quantum spin systems descends from the algebraic structure of the spin operators S^x, S^y and S^z. In the case of spin $\frac{1}{2}$, the spin operators can be written in the $(|\uparrow\rangle, |\downarrow\rangle)$ basis simply as:

$$S^z = \frac{1}{2}\begin{pmatrix}1 & 0\\ 0 & -1\end{pmatrix} \qquad S^x = \frac{1}{2}\begin{pmatrix}0 & 1\\ 1 & 0\end{pmatrix} \qquad S^y = \frac{1}{2}\begin{pmatrix}0 & -i\\ i & 0\end{pmatrix} \qquad \left[S^j, S^k\right] = i\epsilon_{jkl}S^l \tag{2.1}$$

where we took $\hbar = 1$ and ϵ is the totally antisymmetric tensor.

We can also define ladder operators S^+ and S^- which change by one unit the value of the spin projection along the quantization axis (here z):

$$S^+ = (S^x + iS^y) \qquad S^- = (S^x - iS^y) \tag{2.2}$$

such that $S^+|\downarrow_z\rangle = |\uparrow_z\rangle$ and $S^-|\uparrow_z\rangle = |\downarrow_z\rangle$.

For a $S = \frac{1}{2}$ spin all pure quantum states possess a well-defined orientation for the average spin $\langle\psi|\vec{S}|\psi\rangle = \frac{\vec{n}}{2}$, corresponding to a vector $\vec{n}$ on the (unit) Bloch sphere. This means that superposing two states with e.g. opposite orientations produces a new state which has a well-defined orientation as well, e.g. $\frac{|\uparrow_z\rangle + |\downarrow_z\rangle}{\sqrt{2}} = |\uparrow_x\rangle$. However, this property is only true for $S = \frac{1}{2}$.

Let us now consider the case of $S > 1/2$. The spin operators still obey the same commutation relations, but they are now a representation of dimension $d = 2S + 1$ of $SU(2)$. This means that we have $d \times d$ matrices to represent the spin operators, and therefore d possible states along our quantization axis. These states are the eigenstates of S^z and we will label them as $|m_S\rangle$ (with m_S going from $-S$ to S) such that $S^z|m_S\rangle = m_S|m_S\rangle$. These states are the so-called Dicke states, and are often used as the computational basis in numerical simulations. However note that these states are already highly non classical, as we will discuss in the next subsection.

The action of $S^\pm$ on these states is simply given by:

$$S^\pm|m_S\rangle = \sqrt{S(S+1) - m_S(m_S \pm 1)}|m_S \pm 1\rangle \tag{2.3}$$

if $m_S \pm 1 \in [-S, S]$ and 0 otherwise. This is enough to fully write down the three matrices of S^x, S^y and S^z in the $|m_S\rangle$ basis.

The commutation relations of the 3 spin operators lead to Heisenberg-like inequalities that any quantum state must verify, based on the Robertson uncertainty relation. For any state $|\psi\rangle$ in a Hilbert space H and for any two operators A and B acting on H, one must have:

$$\sqrt{\mathrm{Var}(A)\,\mathrm{Var}(B)} \geq \frac{1}{2}|\langle[A, B]\rangle| \tag{2.4}$$

which for the spin operators translates to:

$$\sqrt{\mathrm{Var}(S^y)\,\mathrm{Var}(S^z)} \geq \frac{1}{2}|\langle S^x\rangle| \tag{2.5}$$

valid for any permutation of the indices x, y, z.

2.1.2 Semi-classical and non-classical states of qudits

Whereas a $S = \frac{1}{2}$ spin can always be represented by a single point on a Bloch sphere (with some uncertainty due to the Robertson uncertainty relation), it is not the case for $S > \frac{1}{2}$. In this subsection, we introduce different families of qudits states that are often studied.

We introduced earlier a first family of states, the eigenstates of S^z, also called Dicke states as they were introduced by Dicke in order to study superradiance [39]. These state are non classical, as we will discuss further below.

The closest approximation to classical spin states that we can take as an initial state is represented by coherent spin states (CSS), introduced by Radcliffe in 1971 [40]. This class of states is analogous to classical states as they describe a fully polarized spin in one direction (θ, ϕ) of a generalized Bloch sphere of radius $\sqrt{S(S+1)}$ (θ and ϕ being the canonical angles in spherical coordinates), and they possess minimal uncertainties on the transverse direction in the sense of Eq. 2.5. They can be seen as eigenstates of an operator $S^{\theta,\phi} = \sin(\theta)\cos(\phi)\,S^x + \sin(\theta)\sin(\phi)\,S^y + \cos(\theta)\,S^z$:

$$S^{\theta,\phi}|\theta,\phi\rangle = S|\theta,\phi\rangle \tag{2.6}$$

where S is the length of the spin.

From this property we can derive the expression of these states in the Dicke basis S^z [41]:

$$|\theta,\phi\rangle = \sum_{m_S=-S}^{S} \sqrt{\binom{2S}{S-m_S}} \sin\left(\frac{\theta}{2}\right)^{S-m_S} \cos\left(\frac{\theta}{2}\right)^{S+m_S} e^{-i(S+m_S)\phi}|S,m_S\rangle. \tag{2.7}$$

Indicating with $S^{\perp,1}$ and $S^{\perp,2}$ two spin components orthogonal to $S^{\theta,\phi}$, one has that $\mathrm{Var}\left(S^{\perp,1}\right) = \mathrm{Var}\left(S^{\perp,2}\right) = S/2$, such that the Heisenberg-Robertson inequality Eq. 2.5 becomes an equality.

In our simulation, we will mostly study the cases where the spins are initially polarized along x, $-x$, z or $-z$, which corresponds to $(\theta,\,\phi) = \left(\frac{\pi}{2},0\right)$, $\left(\frac{\pi}{2},\pi\right)$, $(0,0)$ or $(\pi,0)$ respectively. For instance, for x, one obtains:

$$|\frac{\pi}{2},0\rangle = |\mathrm{CSS}_x\rangle = \sum_{m_S=-S}^{S} \sqrt{\binom{2S}{S-m_S}} \frac{1}{2^S}|S,m_S\rangle. \tag{2.8}$$

From the previous expression, it is clear that the state $|\mathrm{CSS}_x\rangle$ is different from the state $\frac{|m_S=+S\rangle+|m_S=-S\rangle}{\sqrt{2}}$ for $S > 1/2$. This last state is a typical example of non-classical state, also called Schrödinger's cat state, that can only be obtained for $S > \frac{1}{2}$.

More generally, instead of a single point on a Bloch sphere, a quantum state for $S > 1/2$ can be represented by a whole function on the sphere. The complete information on the quantum state can be translated into the Wigner function [42], which can take negative values (and hence is not a proper probability distribution). Partial information is instead contained in the Husimi Q function [43] which is defined in each point of the sphere as:

$$Q(\theta,\phi,|\psi\rangle) = \frac{2S+1}{4\pi}|\langle\theta,\phi|\psi\rangle|^2. \tag{2.9}$$

Q only takes positive values, and it is not a proper probability distribution but, being semi-positive definite, it loses some of the information on the phases of the quantum state. We show in figure 2.1 the Husimi Q function for a $|\mathrm{CSS}_x\rangle$, a Dicke state $|S,m=0\rangle$ and a Schrödinger's cat state for an $S = 8$ spin.

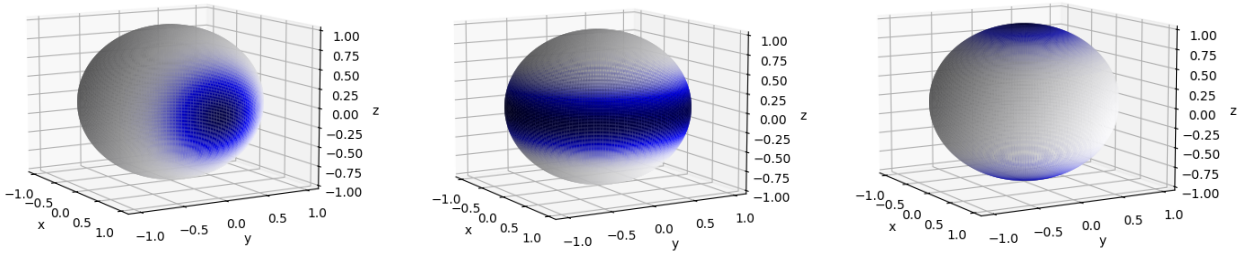

(a) CSS along x (b) Dicke state $|S = 8, 0\rangle$ (c) Schrödinger's cat state

Figure 2.1: Husimi representation of different spin states, for $S = 8$.

As one can see in figure 2.1b the Husimi function for Dicke states corresponds to a non classical state (except for $m = \pm S$) that has a rotational symmetry around the z-axis.

These are only two examples of non-classicality, emphasizing the fact that large-spin systems enjoy a large showcase of non-classical states already at the single spin level.

2.1.3 Squeezed states and entanglement depth

As we discussed above, the state $|\mathrm{CSS}_x\rangle$ is of minimal uncertainty on the transverse spin components $S^\theta = \cos\theta S^y + \sin\theta S^z$, as $\delta S^\theta = \sqrt{\mathrm{Var}\,(S^\theta)}$ is equal to $\sqrt{S}/2$ whatever the angle θ. This leads to an uncertainty region that is shaped like a disk as shown in figure 2.1a. While the Heisenberg-Robertson uncertainty relation bounds the area of this disk from below, nothing prevents the spin state from developing a reduced variance along a given direction θ while increasing it along a perpendicular direction $\theta + \pi/2$, conserving the total area $\mathrm{Var}\left(S^\theta\right)\mathrm{Var}\left(S^{\theta+\pi/2}\right)$. This phenomenon is called spin squeezing, and it is quantified by using the Wineland squeezing parameter [44] :

$$\xi_R^2 = \frac{2S\min_\theta\left[\mathrm{Var}\left(\mathrm{S}^\theta\right)\right]}{|\langle S^x\rangle|^2}. \tag{2.10}$$

The state is said to be squeezed if $\xi_R^2 < 1$. For the $|\mathrm{CSS}_x\rangle$ state instead, $\xi_R^2 = 1$.

This definition can be generalized to the case of N spins of length S:

$$\xi_R^2 = \frac{2SN\min_\theta\left[\mathrm{Var}\left(J^\theta\right)\right]}{|\langle J^x\rangle|^2} \tag{2.11}$$

with $\vec{J} = \sum_i \vec{S}_i$ the collective spin operator.

The above definition of spin squeezing is a property of polarized states, i.e. states with a finite average magnetization $\langle\vec{J}\rangle \neq 0$, which entails that the minimal variance of a spin component transverse to the average orientation must be finite as per the Heisenberg-Robertson inequality. On the other hand Dicke states possess "perfect" squeezing of the uncertainty of a spin component, namely $\mathrm{Var}\,(J^z) = 0$, at the expense of a full depolarisation of the collective spin in the transverse direction, $\langle J^x\rangle = \langle J^y\rangle = 0$. Dicke states can therefore be seen as a limit of squeezed states for which both the minimal variance as well as the transverse polarization vanish.

Squeezed states are very interesting because they allow for more precise measurement of rotation angles, as the variance is reduced for one observable and increased for the conjugate observable [45]. The lower the squeezing parameter is, the more metrological gain one can get

from the state. In particular, for a collection of N coherent spin states $|\mathrm{CSS}_x\rangle^{\otimes N}$, the sensitivity to a rotation around the z axis would be given by the standard quantum limit (SQL) for N spins with length S:

$$\delta\phi^{CSS} = \frac{1}{\sqrt{2SN}}. \tag{2.12}$$

However using a squeezed state, it is possible to go beyond the SQL; since

$$\delta\phi^{sqz} = \frac{\xi}{\sqrt{2SN}} \tag{2.13}$$

giving a better precision when $\xi^2 < 1$, up to the Heisenberg limit $\delta\phi^H = \frac{1}{2SN}$ when ξ^2 scales as $1/N$. It is therefore very appealing to find a protocol that generates squeezing in a scalable manner with system size. In section 2.2 we will give an example of Hamiltonian that can generate such states.

Finally, the squeezing parameter can be used as an entanglement witness to determine the entanglement depth of a given state. A single spin with length $S > 1/2$ can be squeezed; but its squeezing parameter is bounded from below by the inverse spin length as [38]:

$$\xi_R^2 \geq 1/(S+1). \tag{2.14}$$

A collection of N spins of length $S > 1/2$ in a separable state can therefore be squeezed, but its squeezing parameter is bounded in the same way as for a single spin. Entanglement is therefore witnessed by the squeezing parameter when:

$$\xi_R^2 < \frac{1}{S+1} \tag{2.15}$$

since this condition cannot be achieved by any separable state. Repeating the same argument for a collection of k spins, this minimal squeezing parameter is:

$$\left(\xi_R^2\right)_{\min} = \frac{1}{kS+1} \tag{2.16}$$

since the collective spin length is at most kS. Hence, finding

$$\xi_R^2 < \frac{1}{kS+1} \tag{2.17}$$

in an ensemble of $N > k$ spins implies that there exists a block of at least $k+1$ entangled spins, namely the state displays $(k+1)$-partite entanglement [46–48].

Above, we have defined squeezing for spin systems, but it can also be defined for bosonic systems, a paradigmatic example of bosonic squeezed states being squeezed states of light [49]. In order to draw a parallel between the two, it can be interesting to map spins system onto bosonic variables, as we will discuss below.

2.1.4 Spin-boson mappings

Here we will consider two spin-boson mappings that are commonly used, the Schwinger transformation [50] and the Holstein-Primakoff one [51].

Schwinger transformation. In the case of a spin $\vec{J}$, it is possible to represent the spin operators as a function of two bosonic modes $a_\uparrow$ and $a_\downarrow$, such that:

$$\begin{aligned} J^+ &= a_\uparrow^\dagger a_\downarrow \\ J^- &= a_\downarrow^\dagger a_\uparrow \\ J^z &= \frac{1}{2}\left(a_\uparrow^\dagger a_\uparrow - a_\downarrow^\dagger a_\downarrow\right) \end{aligned}$$

with the constraint $a_\uparrow^\dagger a_\uparrow + a_\downarrow^\dagger a_\downarrow = N$. It corresponds to seeing a spin length F, $F \leq N/2$, as an assembly of N bosonic particles of spin 1/2. It is equivalent physically to a Bose-Einstein condensate made of N spin-1/2 particles.

This picture can be generalized by introducing more bosonic modes a_m, $m \in [-S, S]$ corresponding to a Bose-Einstein condensate of spin-S particles:

$$\begin{aligned} J^+ &= \sum_{m=-S}^{S-1} \sqrt{S\left(S+1\right) - m\left(m+1\right)} a_{m+1}^\dagger a_m \\ J^- &= \sum_{m=-S+1}^{S} \sqrt{S\left(S+1\right) - m\left(m-1\right)} a_{m-1}^\dagger a_m \\ J^z &= \sum_{m=-S}^{S} m a_m^\dagger a_m \end{aligned} \tag{2.18}$$

with the constraint $\sum_{m=-S}^{S} a_m^\dagger a_m = N$. The spin operators have now a length $F \leq NS$.

Holstein-Primakoff transformation. A second spin-boson mapping that is often used is the so called Holstein-Primakoff (HP) mapping, that maps a spin of well defined length S onto only one bosonic mode b. It is defined with respect to a given CSS (here $|CSS_{-Z}\rangle = |S, m = -S\rangle$) that corresponds to the bosonic vacuum:

$$\begin{aligned} S^+ &= b^\dagger \sqrt{2S - b^\dagger b} \\ S^- &= \sqrt{2S - b^\dagger b} b \\ S^z &= b^\dagger b - S. \end{aligned} \tag{2.19}$$

HP bosons satisfy the constraint $0 \leq b^\dagger b \leq 2S$.

In the limit $b^\dagger b \ll 2S$, one can linearize the HP transformation, to get:

$$\begin{aligned} S^+ &\approx \sqrt{2S} b^\dagger \\ S^- &\approx \sqrt{2S} b \\ S^z &= b^\dagger b - S \end{aligned}$$

at first order.

This expansion is valid in the limit of a dilute gas of bosons, i.e. if the system remains close to the original CSS. This is the approximation one makes when studying for instance linear spin-waves excitations around a given classical state. We will discuss in chapter 4 a generalization of this method that can describe excitations around non-classical states.

2.2 Many-body spin-squeezing dynamics

2.2.1 The OAT Hamiltonian

Spin-squeezed states can be produced in many different ways, but the most studied squeezing protocol is via a non-equilibrium evolution. The paradigmatic Hamiltonian leading to quantum states with scalable spin-squeezing is the One-Axis Twisting (OAT) Hamiltonian, introduced by Kitagawa and Ueda [52]:

$$\mathcal{H}_{OAT} = \frac{\chi}{N} (J^z)^2 \tag{2.20}$$

where $J^z = \sum_{i=1}^{N} S_i^z$ is the collective spin for a system of N spins S.

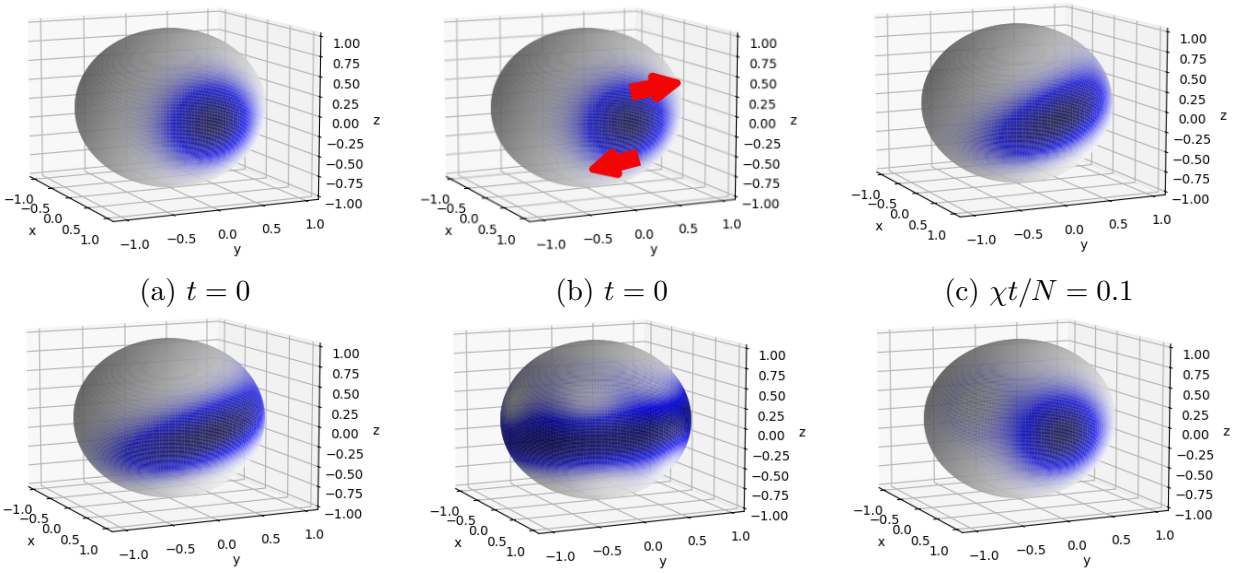

(a) $t = 0$ (b) $t = 0$ (c) $\chi t/N = 0.1$

(d) $\chi t/N = \chi t_{OAT}/N \approx 0.17$ (e) $\chi t/N = 0.5$ (f) $\chi t/N = \chi t_{cat}/N = \pi/2$

Figure 2.2: Husimi representation of the wavefunction for the time evolution of a single spin $S = 8$ with the OAT Hamiltonian at different times.

Starting with a CSS polarized along x, this Hamiltonian will produce squeezing at short times (see figure 2.2). In fact, it can be seen in the form $\mathcal{H}_{OAT} = BJ^z$ with an effective magnetic field $B = \frac{\chi}{N} J^z$ which changes sign from the northern hemisphere to the southern hemisphere of the generalized Bloch sphere. This leads to a deformation of the uncertainty region as depicted in figures 2.2b, 2.2c and 2.2d which generates squeezing. After some point, the state will keep depolarizing, reaching $\langle J^x \rangle = 0$ and the state will lose squeezing (with respect to the Wineland parameter). Remarkably, after a time $t_{cat} = \pi N/2\chi$, the state will evolve into a GHZ state $|\psi_{cat}\rangle = \frac{|\mathrm{CSS}_x\rangle + i|\mathrm{CSS}_{-x}\rangle}{\sqrt{2}}$ (see figure 2.2f).

One can note that the Hamiltonian commutes with $\vec{J}^2$. This means that if the initial state is fully polarized, it will remain on the surface of the Bloch sphere during its time evolution, corresponding to $\langle \vec{J}^2 \rangle = NS\,(NS+1)$. This is why we can represent the state evolution as we did in figure 2.2. For a more generic spin-squeezing dynamics, not conserving $\langle \vec{J}^2 \rangle$, the state of the system would be rather inside the sphere, corresponding to $\langle \vec{J}^2 \rangle < NS\,(NS+1)$.

2.2.2 Scaling of spin squeezing

The OAT Hamiltonian has been largely studied as it is an exactly solvable model. In fact, it only involves the collective spin, which makes it invariant under any permutation of the spins, and it is insensitive to the spatial position of the spins. In particular, Kitagawa and Ueda [52] showed that the optimal squeezing one can achieve with this protocol scales as :

$$\left(\xi^2_{OAT}\right)_{\min} = \frac{1}{2}\left(\frac{3}{2NS}\right)^{\frac{2}{3}} \tag{2.21}$$

in the thermodynamic limit ($N \gg 1$), whereas the time needed to reach this state is:

$$\chi t_{OAT} = 3^{\frac{1}{6}} (2NS)^{\frac{1}{3}} . \tag{2.22}$$

This corresponds to a sensitivity that scales as $\frac{1}{N}^{5/6}$ from Eq. 2.13, which brings us closer to the Heisenberg scaling.

Moreover, the scaling of t_{OAT} is quite favourable with system size, and one can hope to achieve a large amount of squeezing with a large N without exceeding the coherence time of the system at hand. This is to be compared to the scaling of $t_{cat} \sim N$, which requires much longer coherence time. We show in figure 2.3 the time evolution of the squeezing parameter for various system sizes.

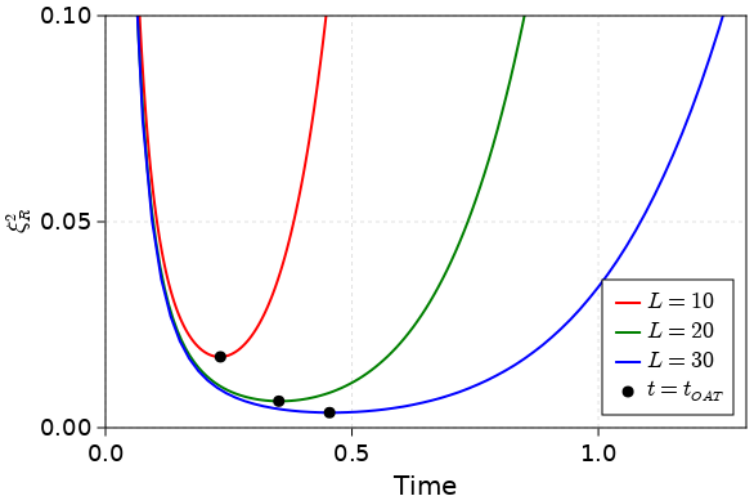

Figure 2.3: Time evolution of the squeezing parameter, for $L \times L$ spins $S = 3$

2.2.3 Experimental realizations of the OAT model

Since the first theoretical proposal of Kitagawa and Ueda to use the OAT model to generate squeezing, there have been many ideas to realize experimentally this Hamiltonian in various platforms.

The first proposals focused on spinor BECs, where the interacting Hamiltonian between $S = 1/2$ bosons in a single spatial mode can be mapped onto a OAT Hamiltonian using the Schwinger transformation [53, 54]. This has been realized experimentally in the past decade in Rubidium condensates [55–58].

Efforts have also been made to realize this Hamiltonian for atoms in a cavity, using light-matter interactions. By adiabatically eliminating the light degree of freedom, it is possible to engineer an effective non-linear spin Hamiltonian that corresponds to the OAT model [59]. This has been realized experimentally in the past few years with atoms [60,61], realizing the highest levels of squeezing ever recorder [62]; as well as with superconducting circuits [63].

2.2.4 Other squeezing dynamics

The OAT Hamiltonian, while being the most famous Hamiltonian for generating spin-squeezed states, is far from being the only one known. First, we can cite the two-axis counter twisting Hamiltonian [52, 64], which is analgous of the OAT model, involving two components of the collective spin operator:

$$\mathcal{H}_{TACT} = \frac{\chi}{2i}\left(\left(J^{+}\right)^{2} - \left(J^{-}\right)^{2}\right) \tag{2.23}$$

.

There are other families of squeezing-generating Hamiltonians, that instead focus on squeezing for states close to Dicke states, for which the squeezed quantity is $\mathrm{Var}\,(J^z)$. This squeezing parameter can be defined in the following manner for an assembly of N spins of length S [65]:

$$\xi_D^2 = (N-1)\,\frac{\left(\tilde{\Delta}J^z\right)^2 + NS^2}{\langle\left(\tilde{J}^x\right)^2\rangle + \langle\left(\tilde{J}^y\right)^2\rangle} \tag{2.24}$$

with $\langle\left(\tilde{J}^\alpha\right)^2\rangle = \langle(J^\alpha)^2\rangle - \langle\sum_{i=1}^{N}(S_i^\alpha)^2\rangle$ and $\left(\tilde{\Delta}J^\alpha\right)^2 = \langle\left(\tilde{J}^\alpha\right)^2\rangle - \langle J^\alpha\rangle^2$. Dicke-squeezed states have $\xi_D^2 < 1$ and are entangled. This parameter is often called Dicke-squeezing parameter as it is able to detect squeezing for Dicke states, which is not the case with the Wineland parameter presented in Eq. 2.11.

This squeezing parameter has been for instance used to detect entanglement and squeezing in spinor BEC of ^{87}Rb [66] where a generalized squeezing parameter of $\xi_D^2 \approx -11.4$ dB was recorded. We will describe with more details examples of Dicke-squeezing dynamics using spinor BEC in Chapter 5.

2.3 Simulation with dipolar atoms

The OAT Hamiltonian involves couplings between all the pairs of spins and hence it is part of the family of long-range interacting models. We can rewrite it in terms of the local spin

operators in the following manner:

$$\begin{aligned}
\mathcal{H}_{OAT} &= \frac{\chi}{N}\left(J^z\right)^2 = \Delta\frac{\chi}{N}\left(J^z\right)^2 + (1-\Delta)\frac{\chi}{N}\left(J^z\right)^2 \\
&= \Delta\frac{\chi}{N}\sum_{i\neq j} S_i^z S_j^z + \Delta\frac{\chi}{N}\sum_i \left(S_i^z\right)^2 + (1-\Delta)\frac{\chi}{N}\left[\vec{J}^2 - \left(J^x\right)^2 - \left(J^y\right)^2\right] \\
&= \Delta\frac{\chi}{N}\sum_{i\neq j} S_i^z S_j^z + \Delta\frac{\chi}{N}\sum_i \left(S_i^z\right)^2 - (1-\Delta)\frac{\chi}{N}\sum_{i\neq j}\left(S_i^x S_j^x + S_i^y S_j^y\right) \\
&- (1-\Delta)\frac{\chi}{N}\sum_i\left(\vec{S}^2 - \left(S_i^z\right)^2\right) + (1-\Delta)\frac{\chi}{N}\vec{J}^2 \\
&= \frac{\chi}{N}\sum_{i\neq j}\Delta S_i^z S_j^z + (1-\Delta)\left(S_i^x S_j^x + S_i^y S_j^y\right) + \frac{\chi}{N}\sum_i\left(S_i^z\right)^2 + \text{cste.} \\
&= \lim_{\alpha\to 0}\frac{\chi}{N}\sum_{i\neq j}\frac{1}{r_{ij}^\alpha}\left[\Delta S_i^z S_j^z + (1-\Delta)\left(S_i^x S_j^x + S_i^y S_j^y\right)\right] + \frac{\chi}{N}\sum_i\left(S_i^z\right)^2 + \text{cste.}
\end{aligned} \tag{2.25}$$

with r_{ij} the distance between the sites i and j. With the last expression obtained above, we can see the similarity between the OAT Hamiltonian and the XXZ model with long-range interactions. The question is now the following: can we mimic the OAT dynamics with long-range interactions when $\alpha > 0$? In order to tackle this question, we will study the case of dipolar systems, for which we have a similar Hamiltonian but with $\alpha = 3$. There exist many experimental platforms that can realise the XXZ dipolar Hamiltonian. In this section, we will focus on the case of magnetic atoms, but we will also give examples of other experimental realisations at the end of the section.

2.3.1 The XXZ Hamiltonian for magnetic atoms

Magnetic atoms offer a unique platform to study the physics of large-S spin ensembles. In this subsection, we detail the type of interactions between those atoms, and introduce the Hamiltonian we will be using in our numerical simulations. In the literature on NMR this treatment goes under the name of "secular approximation" [67].

For an atom in an hyperfine state $|F, m_F\rangle$, if the spin comes from electronic contributions, we can define a magnetic moment $\vec{\mu} = g\mu_B\vec{F}$, where g is the Landé factor and μ_B the Bohr magneton. This magnetic moment will lead to dipolar interactions between atoms. In the following, we will replace F and $\vec{F}$ by S and $\vec{S}$ to make the notation coherent with the previous sections.

We will consider the situation in which atoms are pinned at the sites $\vec{r}_i$ of a lattice, forming a Mott insulator [68]. In this case, atoms interact through dipolar interactions, which couple the atomic spins as follows:

$$\mathcal{H} = d^2\mu_0\sum_{i<j}\frac{\vec{S}_i\cdot\vec{S}_j - 3\left(\vec{S}_i\cdot\hat{r}_{ij}\right)\left(\vec{S}_j\cdot\hat{r}_{ij}\right)}{4\pi r_{ij}^3} - d\sum_i\vec{B}\cdot\vec{S}_i \tag{2.26}$$

where $d = g\mu_B$, $\vec{r}_{ij} = \vec{r}_i - \vec{r}_j$, $\hat{r}_{ij} = \frac{\vec{r}_{ij}}{r_{ij}}$ and $\vec{B}$ is an external magnetic field. The dynamics can thus be computed with spin operators in dimension $2S+1$. For our calculations, let us take $\vec{B}$ along the z axis. We also choose the z axis to be our quantization axis, so we can express S^x

and S^y in terms of the ladder operators:

$$S^x = \frac{S^+ + S^-}{2} \qquad S^y = \frac{S^+ - S^-}{2i}. \tag{2.27}$$

We then move the description to the frame rotating around the z axis at the Larmor frequency $\omega_L = \frac{dB}{\hbar}$ to eliminate the term $-dB\sum_i S_i^z$, but, doing so, we introduce a fast time dependence for all the terms that do not commute with $J^z = \sum_i S_i^z$. If $|\psi(t)\rangle$ is the solution of Schrödinger's equation $i\hbar\frac{\mathrm{d}}{\mathrm{d}t}|\psi\rangle = \mathcal{H}|\psi\rangle$, then the state $|\tilde{\psi}\rangle = U|\psi\rangle$ in the rotating frame is evolved by the Hamiltonian:

$$\tilde{\mathcal{H}} = U\mathcal{H}U^\dagger + i\hbar\frac{\partial U}{\partial t}U^\dagger \tag{2.28}$$

where $U = \exp\left[-\frac{i}{\hbar}dBJ^z t\right]$ is the operator transforming to the frame which rotates at the Larmor frequency around z. The unitary transformation for the spins reads:

$$US^\pm U^\dagger = e^{\mp i\omega_L t}S^\pm. \tag{2.29}$$

As a consequence, all the terms in $\tilde{\mathcal{H}}$ that do not conserve the total magnetization along z oscillate at a frequency ω_L or $2\omega_L$ for $S^\pm S^z$ and $S^\pm S^\pm$ terms respectively. If $\hbar\omega_L$ is taken to be much larger than the energy scale of the dipolar coupling $\frac{d^2\mu_0}{4\pi a^3}$ (a being the minimal distance between two spins, i.e. the lattice spacing), then the rotating terms will average to zero over a time shorter than the characteristic time of the Hamiltonian dynamics. As a consequence they can be neglected in the spirit of the rotating-wave approximation (RWA).

For instance, by expanding the term $US_i^xS_j^xU^\dagger$ we find:

$$\begin{aligned} US_i^xS_j^xU^\dagger &= \frac{1}{4}U\left(S_i^+S_j^+ + S_i^-S_j^+ + S_i^+S_j^- + S_i^-S_j^-\right)U^\dagger \\ &= \frac{1}{4}\left(S_i^-S_j^+ + S_i^+S_j^-\right) + \text{rotating terms.} \end{aligned}$$

The same thing goes for the $S_i^yS_j^y$ term which also reduces to $\frac{1}{4}\left(S_i^-S_j^+ + S_i^+S_j^-\right)$. We will be using later that $S_i^yS_j^y = S_i^xS_j^x$ up to rotating terms.

The last term we must consider is $\left(\vec{S}_i\cdot\hat{r}_{ij}\right)\left(\vec{S}_j\cdot\hat{r}_{ij}\right)$. First, one can notice that all the products of S^z with either S^x or S^y will be discarded (because we will only get terms of the kind S^+S^z or S^-S^z). We are thus left with five terms, containing $S_i^xS_j^x$, $S_i^yS_j^y$, $S_i^zS_j^z$, $S_i^xS_j^y$ and $S_i^yS_j^x$. Computing the last two terms, we finally find:

$$\begin{aligned} US_i^xS_j^yU^\dagger &= \frac{1}{4i}\left(-S_i^+S_j^- + S_y^-S_j^+\right) + \text{rotating terms} \\ US_i^yS_j^xU^\dagger &= \frac{1}{4i}\left(S_i^+S_j^- - S_y^-S_j^+\right) + \text{rotating terms} \end{aligned}$$

thus the two terms cancel each other (because they share the same prefactor $\hat{r}_{ij}^x\hat{r}_{ij}^y$).

Finally, putting all these results together, we have :

$$\mathcal{H} = d^2 \sum_{i<j} \frac{\mu_0}{4\pi r_{ij}^3} \left[S_i^z S_j^z + 2 S_i^x S_j^x - 3 \left(\left(\left(\hat{r}_{ij}^x\right)^2 + \left(\hat{r}_{ij}^x\right)^2 \right) S_i^x S_j^x + \left(\hat{r}_{ij}^z\right)^2 S_i^z S_j^z \right) \right] \tag{2.30}$$

where we used that $S_i^y S_j^y = S_i^x S_j^x$ in the RWA. Now we can rewrite $\left(\hat{r}_{ij}^x\right)^2 + \left(\hat{r}_{ij}^x\right)^2 = 1 - \left(\hat{r}_{ij}^z\right)^2$ because $\hat{r}_{ij}$ is of unit norm. We finally obtain:

$$\begin{aligned} \mathcal{H} &= d^2 \sum_{i<j} \frac{\mu_0}{4\pi r_{ij}^3} \left[\left(1 - 3 \left(\hat{r}_{ij}^z\right)^2 \right) S_i^z S_j^z + \left(1 - 3 \frac{1 - \left(\hat{r}_{ij}^z\right)^2}{2} \right) \left(S_i^x S_j^x + S_i^y S_j^y \right) \right] \\ &= d^2 \mu_0 \sum_{i<j} \frac{1 - 3 r_z^2}{4\pi r_{ij}^3} \left(S_i^z S_j^z - \frac{1}{2} \left(S_i^x S_j^x + S_i^y S_j^y \right) \right). \end{aligned} \tag{2.31}$$

Given the fact that our magnetic field $\vec{B}$ is along z, $\hat{r}_{ij}^z$ can be seen as the cosine of the angle between $\vec{B}$ and $\vec{r_{ij}}$ which we write as $\cos(\theta_{ij})$. We also define $J = \frac{d^2 \mu_0}{4\pi a^3}$ and $J_{ij} = J a^3 \frac{1 - 3\cos(\theta_{ij})}{r_{ij}^3}$. Finally, if we consider a one dimensional chain of spins along the x axis, or a two dimensional square lattice in the Oxy plane (as we will do for the rest of this thesis), then all the $\vec{r}_{ij}$ are also in the Oxy plane, which leads to $\theta_{ij} = \frac{\pi}{2}$ and thus $\cos(\theta_{ij}) = 0$. We can then rewrite our Hamiltonian as:

$$\mathcal{H} = \sum_{i<j} J_{ij} \left(-\frac{1}{2} \left(S_i^x S_j^x + S_i^y S_j^y + \Delta S_i^z S_j^z \right) \right) \tag{2.32}$$

where $\Delta = -2$. This Hamiltonian corresponds to the so-called dipolar XXZ model (two directions with the same coupling and an anisotropy for the third axis). Finally, we must also take into account a quadratic Zeeman term which comes from the magnetic field, as well as from a tensor light shift caused by the optical lattice on the atomic spectrum [69]:

$$\mathcal{H} = \sum_{i<j} J_{ij} \left(-\frac{1}{2} \left(S_i^x S_j^x + S_i^y S_j^y + \Delta S_i^z S_j^z \right) \right) + B_q \sum_i \left(S_i^z \right)^2. \tag{2.33}$$

Apart from the geometry of the lattice, B_q is the only free parameter in the Hamiltonian which can be potentially tuned in an experiment. As we will see in the next chapters, the value of this parameter will have a crucial role on the dynamics of the spin system. Finally, one can note that this last term corresponds to a OAT Hamiltonian acting only on the individual spins, and it is a term that was already present in the expression we gave of the OAT Hamiltonian in Eq. 2.25.

2.3.2 Experimental realisations of the dipolar XXZ model

In the past few years, an increasing number of experiments have been set up using large-spin magnetic atoms. The recent interest in this field can be explained both by the technological advances which allow for trapping and precise measurements of the states of those atoms; as well as their interest as quantum simulators of quantum magnetism and long-range interactions in general.

Among the experimental platforms, we can cite the ones on Chromium atoms ($S = 3$), in which dipolar interactions play a crucial role in spin dynamics [70–73] and allow to study

strongly interacting systems thanks to the high spin value (interactions are ~ 36 times stronger than for spin $\frac{1}{2}$, and ~ 9 times stronger than spin 1, assuming a fixed gyromagnetic factor g).

Other experiments with fermionic states of Erbium ($S = \frac{19}{2}$) have achieved a significant control over the quadratic Zeeman term B_q [69]. Moreover, we can cite experiments on Dysprosium ($S = 8$) [74–76]. Those experiments have worked with thermal atoms, so that their dipolar interactions are negligible. They have shown that by using the tensorial light shift, one can create spin-squeezed and cat-like states of single spins [41], and have demonstrated the gain in sensitivity of quantum sensing using such non-classical states [74] [77].

Finally, many techniques have been developed to monitor and measure with precision the quantum state of individual or few atoms. One of the most promising ones are the so-called quantum-gas microscopes, which are now able to measure quantum states of single atoms with high precision [78] [79]. In a recent experiment with Erbium atoms, it was possible to study the spatial structure of the ground state of a Hubbard model at half filling [80]. By tuning the orientation of the dipoles with an external magnetic field, it was possible to modify the anisotropy of dipole-dipole interactions. This lead to the emergence of a variety of different stripe phases - also called dipolar quantum solid phases - depending on the orientation of the dipoles with respect to the lattice axes.

All these experiments have been able to measure the evolution of spin populations [69] and of the collective spin [72], global correlations along the quantization axis [73] and even bipartite correlations [81]. However, the certification of entanglement in these systems is still lacking, and part of the work presented in this thesis is directed toward this effort. In the next chapter, we will propose various protocols to generate and detect highly entangled states of a few magnetic atoms. In the following chapter, we will see how to generate scalable squeezing - i.e. stronger the larger the number of atoms - in 2D arrays of magnetic atoms.

There exist many other platforms to implement and study the dipolar XXZ model. For instance, Rydberg atoms offer a promising alternative to magnetic atoms thanks to their large dipole moment in the Rydberg state [82, 83]. The lattice configuration can be controlled with very high precision using arrays of optical tweezers [84], and they have been used as a quantum simulator to study different spin Hamiltonians, such as the quantum Ising model with Van der Waals interactions [85–87], the XY model [88, 89] and even the XXZ model with dipolar interactions [90]. Among the other existing platforms realizing long-range XXZ models, it is worth mentioning trapped ions [91, 92] and polar molecules [93–95].

Chapter 3

Few-qudit entangled states with dipolar interactions

In this chapter, we study the entanglement dynamics of a few qudits under unitary evolution with the dipolar XXZ Hamiltonian presented in the previous chapter. At first, we detail our results in the case of only two spins, and we show that for specific parameter values the Hamiltonian is equivalent to a OAT Hamiltonian. Secondly, we present results for an increasing number of qudits (from 3 to 6) and discuss how the entangled states seen in the two-qudit case persist upon scaling up the system size.

3.1 Entanglement dynamics for two qudits

We start by studying the unitary dynamics of an initial factorized state, with only two spins, with the dipolar XXZ Hamiltonian presented in the previous chapter. For our initial state, we may consider either the case where both spins are in a given Dicke state along z, or in a coherent spin state (CSS) along a given direction. If the initial state is a given Dicke state $|S, m\rangle$ for both spins, as soon as $B_q \neq 0$, the spin-changing interaction becomes off-resonant, and the ensuing evolution of spin populations is rather small. A much more interesting spin dynamics is instead observed when considering the case of coherent spin states (CSS) as initial states, which are a superposition of several Dicke states. A uniform coherent spin state along $\pm z$ is an eigenstate of the Hamiltonian, so this is not a good choice for the initial state. On the other hand, a staggered CSS along z leads to almost no dynamics in the presence of the term B_q. These considerations suggest that the most interesting initial state to consider is a coherent spin state in the xy plane. Since our Hamiltonian is $U(1)$ symmetric, we choose coherent spin states pointing along the $\pm x$ axis without loss of generality. Both the uniform CSS (both spins aligned with $+x$) and the staggered CSS (one spin aligned with $+x$, the other aligned with $-x$) lead to non trivial dynamics, leading to highly entangled states. In this first section, we will study this dynamics with two spins, starting either with a coherent or a staggered CSS along $\pm x$. In particular, we will investigate the role played by B_q in the appearance of highly entangled states, and the origin of this entangling dynamics in relationship with that of the one-axis twisting model.

In the case of only two qudits, the dipolar XXZ Hamiltonian takes the form:

$$\mathcal{H}_2 = -\frac{J}{2}\left(S_1^x S_2^x + S_1^y S_2^y - 2S_1^z S_2^z\right) + B_q\left((S_1^z)^2 + (S_2^z)^2\right). \tag{3.1}$$

We investigate the dynamics of the system after a quench from a factorized initial state, and we consider two cases : first, the case where the initial state is a staggered CSS along the x axis, $|\psi_{stag}\rangle = |S_x\rangle \otimes |-S_x\rangle$ with $S^x|\pm S_x\rangle = \pm S|\pm S_x\rangle$, and secondly the case where the initial state is uniform along the x axis, $|\psi_{uni}\rangle = |S_x\rangle \otimes |S_x\rangle$. The two selected states are both states of maximal collective-spin length, when defining appropriately the collective spin. In the case of the uniform CSS, the collective spin of maximal length can be chosen as simply the sum of the two spins $\vec{J} = \vec{S}_1 + \vec{S}_2$. In the case of the staggered CSS, instead, the collective spin of maximal length can be chosen as $\vec{J}_{stag} = (S_1^x - S_2^x, S_1^y - S_2^y, S_1^z + S_2^z)$.

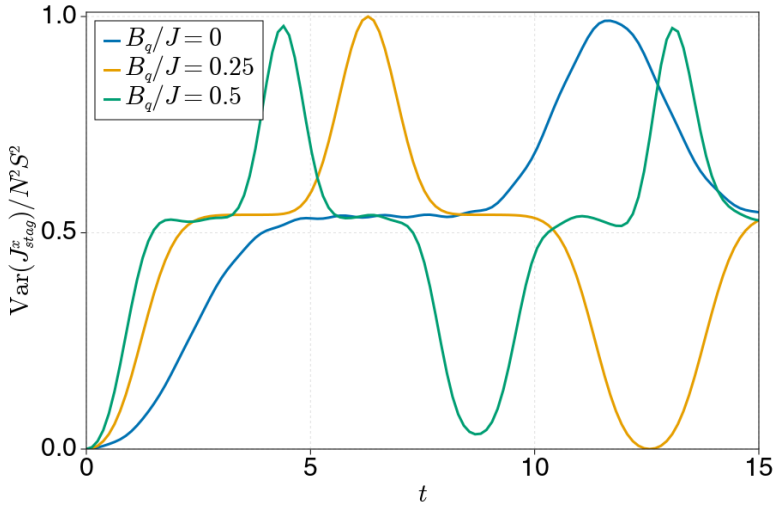

Figure 3.1: Time evolution of the variance of J^x_{stag}, starting with a staggered CSS along x, with the dipolar XXZ Hamiltonian for $N = 2$ spins with length $S = 3$, and for different values of B_q.

3.1.1 Emergence of the one-axis twisting dynamics from a staggered initial state

In the case of a staggered initial state, we show the time evolution of the variance of $J^x_{stag} = S_1^x - S_2^x$ for three different values of B_q in figure 3.1. One can immediately observe that the dynamics is closely reminiscent to that generated by dynamics obtained with the OAT Hamiltonian (see figure 2.2 in the previous chapter). In order to draw a parallel between the dipolar Hamiltonian and the OAT one, we can rewrite the dipolar Hamiltonian in terms of the

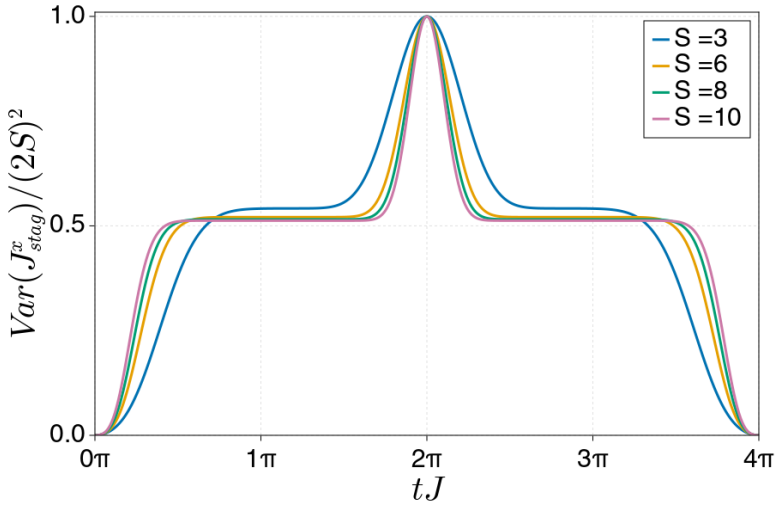

Figure 3.2: Time evolution of the variance of J^x_{stag} for different values of S at $B_q = J/4$.

staggered collective spin:

$$\begin{aligned}\mathcal{H}_2 &= \frac{J}{4}\left[\left(J^x_{\text{stag}}\right)^2 + \left(J^y_{\text{stag}}\right)^2 + \left(J^z\right)^2\right] \\ &- \frac{J}{4}\left[\left(S^x_1\right)^2 + \left(S^x_2\right)^2 + \left(S^y_1\right)^2 + \left(S^y_2\right)^2 + \left(S^x_2\right)^2 + \left(S^z_2\right)^2\right] \\ &+ \frac{J}{2}S^z_1 S^z_2 + B_q\left(\left(S^z_1\right)^2 + \left(S^z_2\right)^2\right) \\ &= \frac{J}{4}\left[\vec{J}^2_{\text{stag}} - \vec{S}^2_1 - \vec{S}^2_2\right] + \frac{J}{4}\left(J^z\right)^2 + \left(B_q - \frac{J}{4}\right)\left(\left(S^z_1\right)^2 + \left(S^z_2\right)^2\right). \end{aligned} \tag{3.2}$$

For the special value $B_q = J/4$, we the have:

$$\mathcal{H}_2 = \frac{J}{4}\left[\vec{J}^2_{\text{stag}} - 2S\left(S+1\right)\right] + \frac{J}{4}\left(J^z\right)^2. \tag{3.3}$$

Since $\left(J^z\right)^2$ commutes with $\vec{J}^2_{\text{stag}}$, $\vec{J}^2_{\text{stag}}$ is a conserved quantity in the dynamics. The initial state is an eigenstate of this operator with maximal eigenvalue $2S\left(2S+1\right)$. The dipolar Hamiltonian becomes therefore proportional to a OAT Hamiltonian up to a constant.

We can then ask ourselves if the value of S plays a role in the dynamics of the system. Clearly for $B_q = J/4$ we expect to recover the OAT dynamics for a collective spin of length $2S$, and with a coupling constant $J/4$ independent of the spin length. This is clearly shown in figure 3.2, where the variance of J^x_{stag} is seen to reach the maximal value associated with the formation of a cat state at the same time for any S. For practical reasons, we will focus in the following of this chapter on the case $S = 3$, but all the results obtained here can be generalized to arbitrary integer S. The case of half-integer S is quite similar, and in the case of $B_q = J/4$, the dynamics is just slowed down by a factor 4, therefore we will not discuss the case of half integer S in this chapter further.

The next question we address is how robust this dynamics is when changing the value of B_q away from the fine-tuned value $B_q = J/4$. Figure 3.1, already suggests that the OAT dynamics survives when B_q differs from $J/4$, but we want to investigate this in a more quantitative way. In particular, we want to determine if we can still produce a cat-like state during the unitary

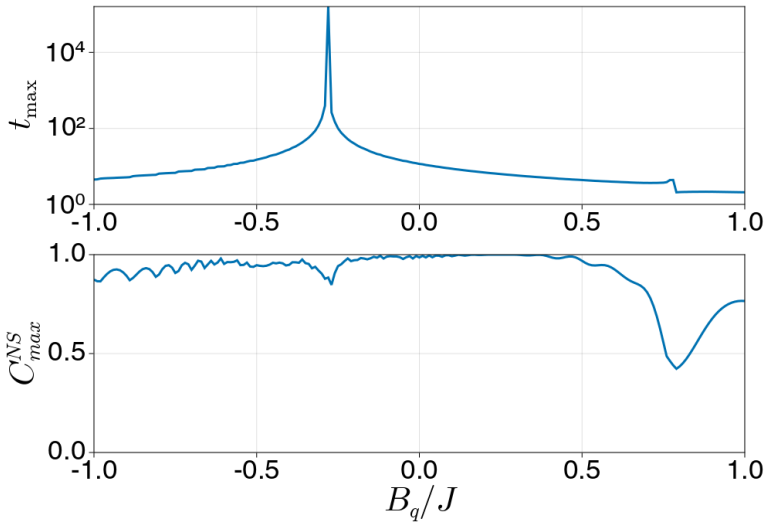

Figure 3.3: Evolution of t_{cat} (top) and C^{2S}_{max} (bottom) for different values of B_q/J for $S = 3$. Note that the vertical axis is in log scale for t_{cat}.

time evolution, and determine how close it is to a perfect cat state. For this purpose, we introduce the $2S$-th order coherence C^{2S}:

$$C^{2S}(t) = |\langle\psi(t)|\left(S_1^+ S_2^-\right)^{2S}|\psi(t)\rangle|/\mathcal{N}_{cat} \tag{3.4}$$

with $\mathcal{N}_{cat}$ the coherence of the cat state, defined by:

$$\mathcal{N}_{cat} = |\langle\psi_{cat}|\left(S_1^+ S_2^-\right)^{2S}|\psi_{cat}\rangle| = \frac{1}{2}\prod_{m=-S}^{S-1}\left(S(S+1) - m(m+1)\right). \tag{3.5}$$

This coherence probes whether $|\psi(t)\rangle$ is a coherent superposition of states with opposite spin orientations along x. Note that here $S^{\pm}$ are defined with respect to x as the quantization axis, and the normalization $\mathcal{N}_{cat}$ is here such that C^{2S} is always between 0 and 1, and is equal to 1 if the state $|\psi(t)\rangle$ is a cat state of the form:

$$|\psi_{cat}\rangle = \frac{|S_1^x = S, S_2^x = -S\rangle + e^{i\phi}|S_1^x = -S, S_2^x = S\rangle}{\sqrt{2}} \tag{3.6}$$

for any value of ϕ. Note also that $C^{2S} < |\langle\psi(t)|\psi_{cat}\rangle| = \mathcal{F}_{cat}$, where $\mathcal{F}_{cat}$ is the fidelity with respect to the cat state, which means that requesting $C^{2S} \approx 1$ is a more strict criterion for the realization of a cat state than that of requesting $\mathcal{F}_{cat} \approx 1$. At the same time C^{2S} is more significant from a metrological point of view, as it expresses the contrast of parity oscillations under rotation of the state - see subsection 3.2.1. We then look at the maximum value of C^{2S} in time, $C^{2S}_{\max}$ for different values of B_q and the time needed to reach this maximum t_{max}. Results are shown in figure 3.3. The first striking result is that we get almost perfect cat states ($C^{2S}_{max} > 0.9$) for a broad range of values for negative B_q, and for positive B_q values up to $3J/4$.

The second result of interest is the behaviour of the time t_{max} when B_q is close to the critical value $B_q^c \approx -0.285J$. Around this value, the dynamics becomes very slow, and the time is found to diverge as $t_{max} \sim 1/|B_q - B_q^c|$, leading to the freezing of the dynamics. We will give in the next chapter an explanation of this divergence, based on an approximate separation of variables

for the dipolar Hamiltonian. By controlling B_q one could in principle build a two-qudit gate that would produce a cat state by first setting $B_q \approx J/4$, then almost freezing the dynamics in that state by switching to $B_q \approx -0.285J$. We show in figure 3.4 the resulting dynamics, and we verify that it indeed leads to a long-lived cat-like state.

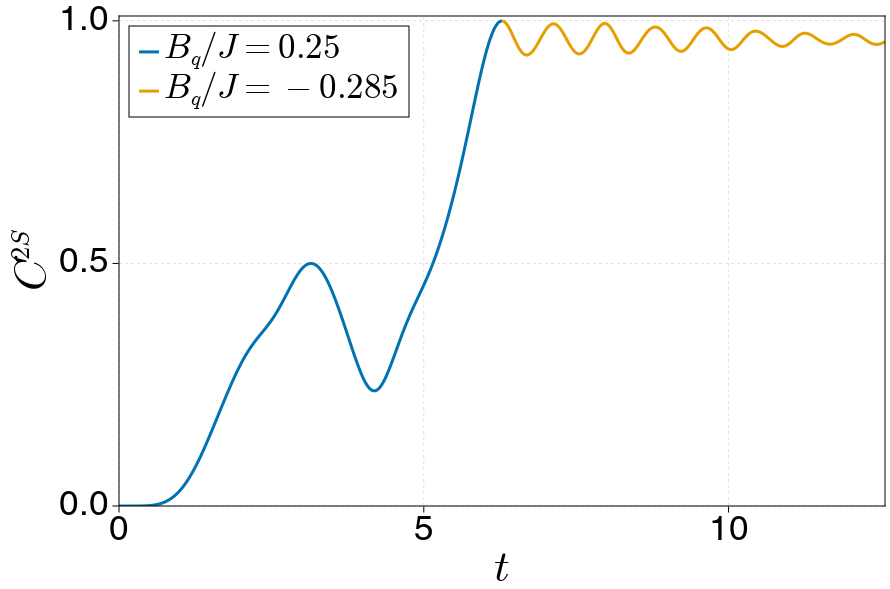

Figure 3.4: Time evolution of C^{2S}, starting with a staggered initial state and $B_q = 0.25$, then switching to $B_q = -0.285$ at $t = t_{cat}$ for $S = 3$.

Finally, we observe in figure 3.3 a sharp dip in C^{2S}_{max} around $B_q = 3J/4$. We will comment on this result more in details in subsection 3.1.2 when studying the uniform initial state as we will provide by then an explanation for this behaviour. We will also try to generalise these results to the case of a larger number N of spins in section 3.2.

3.1.2 Emergence of the one-axis twisting dynamics from a uniform initial state

We now study the case of a uniform initial state. First, we try to determine if there exists a specific value of B_q for which we can map our Hamiltonian onto a OAT one for the uniform collective spin, similarly to the staggered case. In order to do so, we rewrite our Hamiltonian as:

$$\begin{aligned}\mathcal{H}_2 &= -\frac{J}{4}\left[(J^x)^2 + (J^y)^2\right] + \frac{J}{2}(J^z)^2 + \frac{J}{4}\left[(S_1^x)^2 + (S_2^x)^2 + (S_1^y)^2 + (S_2^y)^2\right] \\ &\quad - \frac{J}{2}\left[(S_1^z)^2 + (S_2^z)^2\right] + B_q\left((S_1^z)^2 + (S_2^z)^2\right) \\ &= -\frac{J}{4}\left[\vec{J}^2 - \vec{S}_1^2 - \vec{S}_2^2\right] + \frac{3J}{4}(J^z)^2 + \left(B_q - \frac{3J}{4}\right)\left((S_1^z)^2 + (S_2^z)^2\right). \end{aligned} \tag{3.7}$$

As we can see, for $B_q = 3J/4$, a uniform initial state fixes the value of $\vec{J}^2$ to its maximum $2S(2S+1)$ and we reconstruct exactly a OAT Hamiltonian up to constant terms. The next step is then to determine how robust the cat-state formation dynamics is when tuning the value

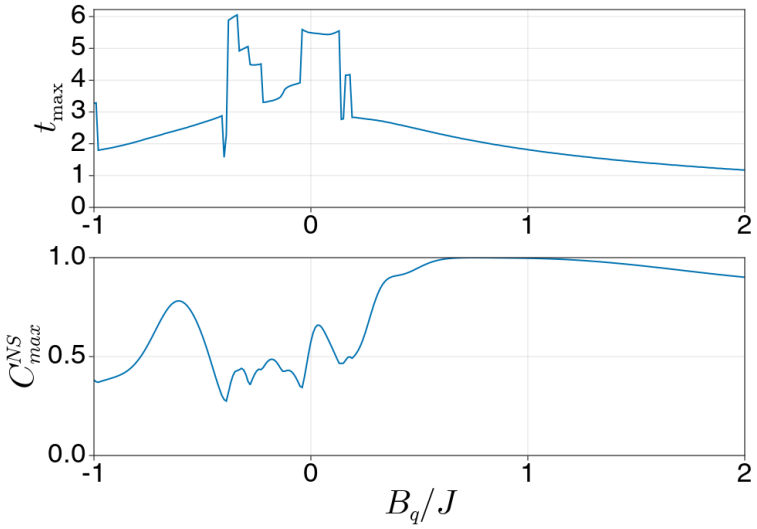

Figure 3.5: Evolution of t_{cat} (top) and C^{2S}_{max} (bottom) in the case of a uniform initial state for different values of B_q/J for $S = 3$.

of B_q away from this fine-tuned value. Figure 3.5 shows the B_q dependence of C^{2S}_{max} and t_{max}, starting with a uniform initial state - using exactly the same method as for figure 3.3. Note that, in the case of the uniform initial state, C^{2S} is defined as:

$$C^{2S}(t) = |\langle\psi(t)| \left(S_1^+ S_2^+\right)^{2S} |\psi(t)\rangle| / \mathcal{N}_{cat}. \tag{3.8}$$

As we can see in figure 3.5, there is a range of values of B_q, $0.5 \lesssim B_q/J \lesssim 1.5$ for which the dynamics produces a cat-like state with high fidelity. However, unlike the case of the staggered initial state, we do not have a value of B_q for which t_{max} diverges. Again, we will give an explanation of this result in the next chapter, based on an approximate separation of variables for the dipolar Hamiltonian.

Reducing instead B_q towards $B_q = J/4$, a cat-like state no longer appears in the dynamics, and we observe rapid variations of t_{max}, because the absolute maximum is one out of several local maxima with comparable height. This behaviour is reminiscent of the dip in C^{2S}_{max} and the jump in t_{max} observed in figure 3.3 for the dynamics starting from the staggered initial state around $B_q = 3J/4$, and we discuss its origin in the following subsection.

3.1.3 Generation of a "twin-spin" state

The dipolar XXZ dynamics offers in fact an alternative paradigm of entanglement generation with respect to the one of the OAT model. In this paradigm, that we indicate here as "twin-spin state" generation, the length of the collective spin maximized by the initial state is not conserved. The general Hamiltonian for this dynamics takes the following form:

$$\mathcal{H}_\alpha = \frac{\chi}{N}\left[(J^z)^2 + \alpha\left(\vec{J}_{stag}\right)^2\right] \tag{3.9}$$

where the initial state is the uniform coherent spin state. Alternatively, when starting from the staggered initial state one can consider the Hamiltonian:

$$\tilde{\mathcal{H}}_\alpha = \frac{\chi}{N}\left[(J^z)^2 + \alpha\left(\vec{J}\right)^2\right] \tag{3.10}$$

which results from the previous one by the unitary transformation flipping the x and y spin components of one of the two spins. We have already seen that the Hamiltonian of Eq. 3.9 is reproduced by the dipolar Hamiltonian (up to additive constant) when $B_q = J/4$, with $\alpha = 1$; while the Hamiltonian of Eq. 3.10 is reproduced by the dipolar one for $B_q = 3J/4$, this time with $\alpha = -1/3$. It is then instructive to consider the dynamics generated by $\mathcal{H}_\alpha$ starting from the state where collective spin is *not* conserved. Interestingly, the dynamics has a salient feature which is independent of the value of α. We show in figure 3.6 the time evolution of the variance of J^x, the variance of J^x_{stag} and the mean value of $\vec{J}^2$ with $\mathcal{H}_\alpha$, for different values of α. For $\alpha = 0$, we recover the usual OAT model, which produces a cat state at $t_{cat} = N\pi/2\chi$ if we start with a coherent spin state along x at $t = 0$. For any non-zero α, we clearly see that $\vec{J}^2$ is no longer conserved. However, we notice that for all values of α (and for an even N), starting with the uniform initial state, the state obtained at $t = t_{cat}$ has a vanishing variance of J^x_{stag}. This is a very interesting property since the state we obtain at $t = t_{cat}$ is not separable. Indeed it indicates that the state we obtain at $t = t_{cat}$ is a superposition of states with the same projections along the x axis for the individual spins.

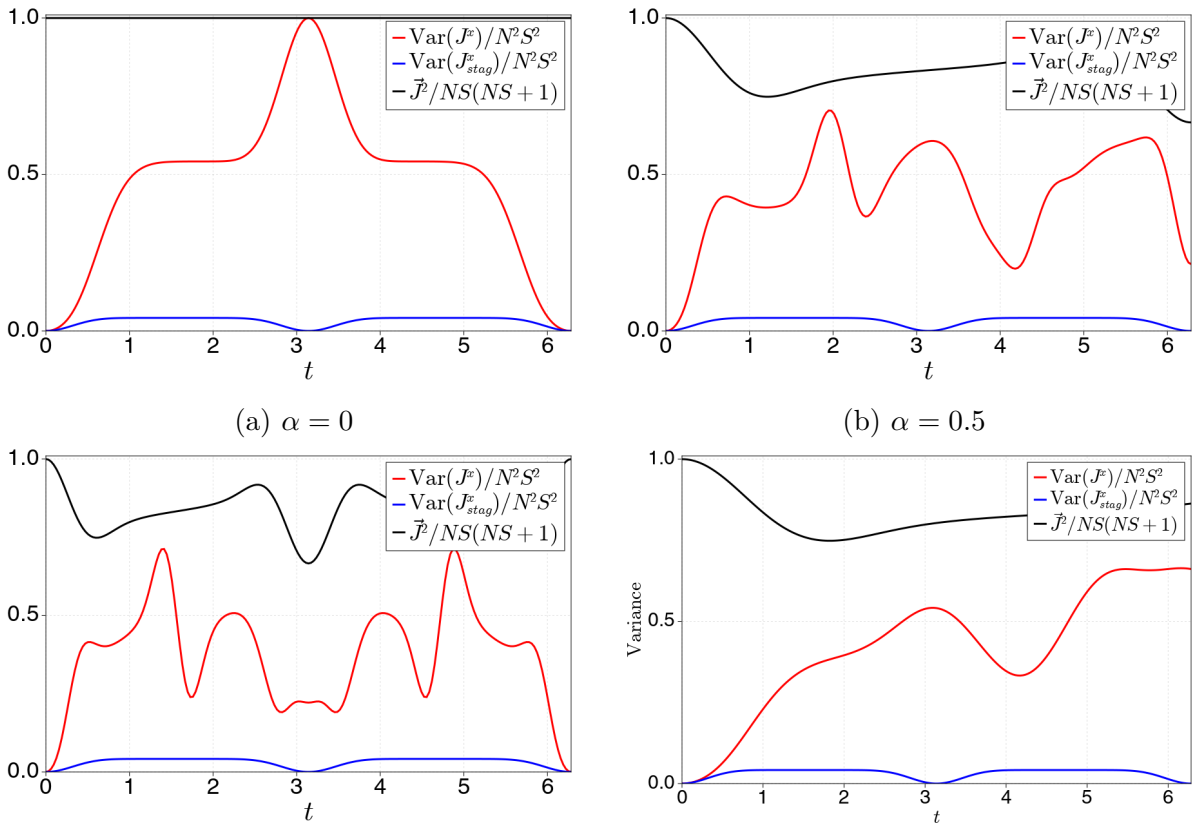

(a) $\alpha = 0$ (b) $\alpha = 0.5$

(c) $\alpha = 1$ (d) $\alpha = -1/3$

Figure 3.6: Time evolution of the variance of J^x and J^x_{stag} with $\mathcal{H}_{ST}$, starting from a uniform CSS along x, with $N = 2$, $S = 3$, $\chi = 1$ and (a) $\alpha = 0$, (b) $\alpha = 0.5$, (c) $\alpha = 1$ and (d) $\alpha = -1/3$.

In order to visualise better this property, we plot in figure 3.7 the full state tomography in the x and z bases. As we can see, the state obtained at $t = t_{cat}$ is always diagonal in the joint basis S^x_1, S^x_2. This numerical observation can be proven analytically. Indeed, our Hamiltonian

is the sum of two commuting operators, $\frac{\chi}{N}\left(J^z\right)^2$ and $\alpha\frac{\chi}{N}J^2_{stag}$. At $t = t_{cat}$, we have:

$$\begin{aligned}|\psi\left(t_{cat}\right)\rangle &= e^{\frac{-it_{cat}}{\hbar}H}|\psi_0\rangle \\ &= e^{\frac{-i\alpha\chi t_{cat}}{N\hbar}\vec{J}^2_{stag}}e^{\frac{-i\chi t_{cat}}{N\hbar}(J^z)^2}|\Psi_0\rangle \\ &= e^{\frac{-i\alpha\chi t_{cat}}{N\hbar}\vec{J}^2_{stag}}|\psi_{cat}\rangle.\end{aligned}$$

where $|\psi_{cat}\rangle$ is the uniform cat state, i.e. $|\psi_{cat}\rangle = \frac{|S_x,S_x\rangle+i|-S_x,-S_x\rangle}{\sqrt{2}}$. Since $\vec{J}^2_{stag}$ commutes with J^x_{stag}, we finally have:

$$\begin{aligned}\langle\psi\left(t_{cat}\right)|J^x_{stag}|\psi\left(t_{cat}\right)\rangle &= \langle\psi_{cat}|e^{\frac{i\alpha\chi t_{cat}}{N\hbar}\vec{J}^2_{stag}}J^x_{stag}e^{\frac{-i\alpha\chi t_{cat}}{N\hbar}\vec{J}^2_{stag}}|\psi_{cat}\rangle \\ &= \langle\psi_{cat}|J^x_{stag}|\psi_{cat}\rangle \\ \langle\psi\left(t_{cat}\right)|\left(J^x_{stag}\right)^2|\psi\left(t_{cat}\right)\rangle &= \langle\psi_{cat}|\left(J^x_{stag}\right)^2|\psi_{cat}\rangle\end{aligned}$$

which means that we have exactly the same variance for J^x_{stag} at $t = t_{cat}$ as for the cat state ($\alpha = 0$), this variance being equal to 0.

In particular, for $N = 2$ and $\alpha = 1$ - which is the case obtained with the dipolar Hamiltonian, with $B_q = J/4$ - we obtain in the dynamics a very particular state, in which the two spins have always identical S^x spin components, but the latter components can take several different values. We will call this state a Twin Spin State (TSS).

The specificity of the twin-spin state is to have perfectly correlated S^x components for the two spins, so that we can write it in the basis of eigenvectors of the local S^x spin operators as:

$$|TSS\rangle = \sum_{m_x} c_{m_x}|m_x\rangle \otimes |m_x\rangle \tag{3.11}$$

where $S^x|m_x\rangle = m_x|m_x\rangle$. We can look at the distribution of weights along the diagonal, namely the $|c_{m_x}|^2$ distribution, and we find that it obeys a Gaussian law centred around $m_x = 0$ and with a standard deviation $\sigma \approx 0.85\sqrt{S}$ (see figure 3.8).

These states can be seen as a generalization to larger spins S of Bell-states - even though they are not maximally entangled with respect to entanglement entropy. We will discuss in the next subsection the entanglement properties of these states.

3.1.4 Entanglement certification

In order to show that the quench dynamics with the dipolar XXZ Hamiltonian - starting with a uniform of staggered initial state - produces entanglement, we can use the following criterion for large-S spins [96], that detects entanglement if:

$$\langle\left(\tilde{J}^\alpha\right)^2\rangle + \langle\left(\tilde{J}^\beta\right)^2\rangle - N\left(N-1\right)S^2 > \left(N-1\right)\left(\tilde{\Delta}J^\gamma\right)^2 \tag{3.12}$$

with $\langle\left(\tilde{J}^\alpha\right)^2\rangle$ and $\left(\tilde{\Delta}J^\alpha\right)^2$ defined as follows:

$$\langle\left(\tilde{J}^\alpha\right)^2\rangle = \langle(J^\alpha)^2\rangle - \sum_{i=1}^{N}\langle(S^\alpha_i)^2\rangle$$

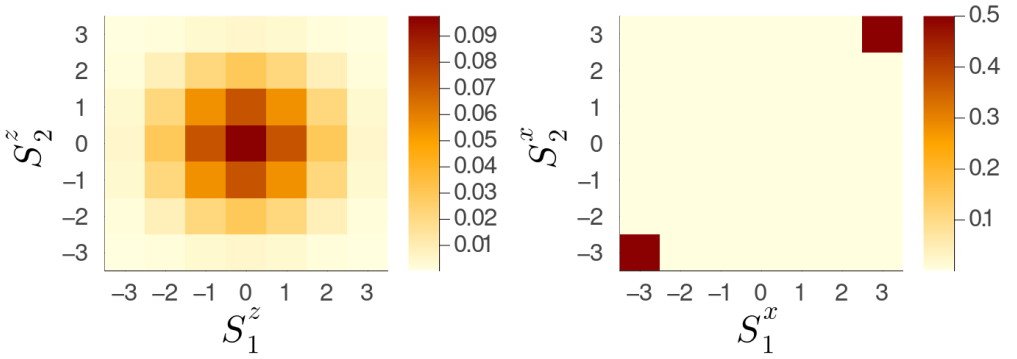

(a) $\alpha = 0$

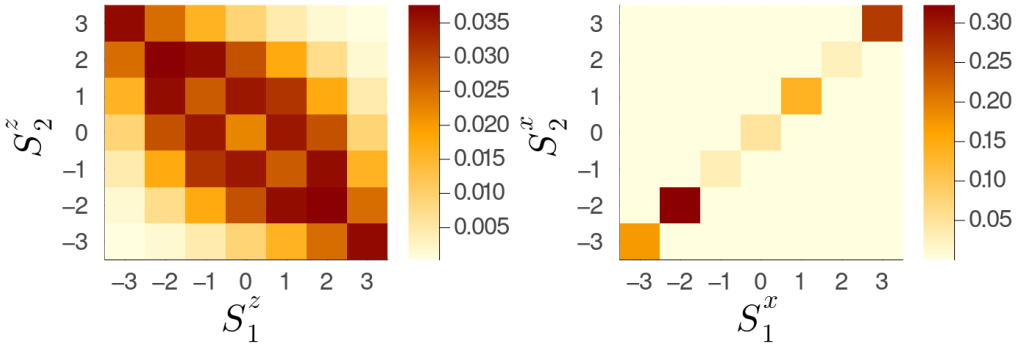

(b) $\alpha = 0.5$

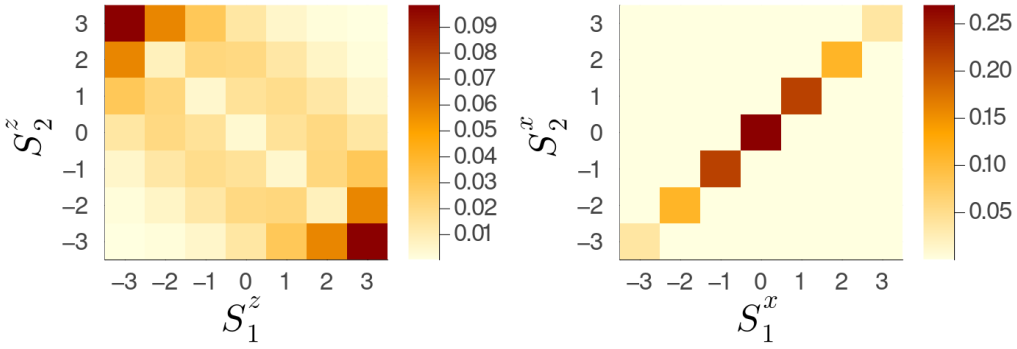

(c) $\alpha = 1$

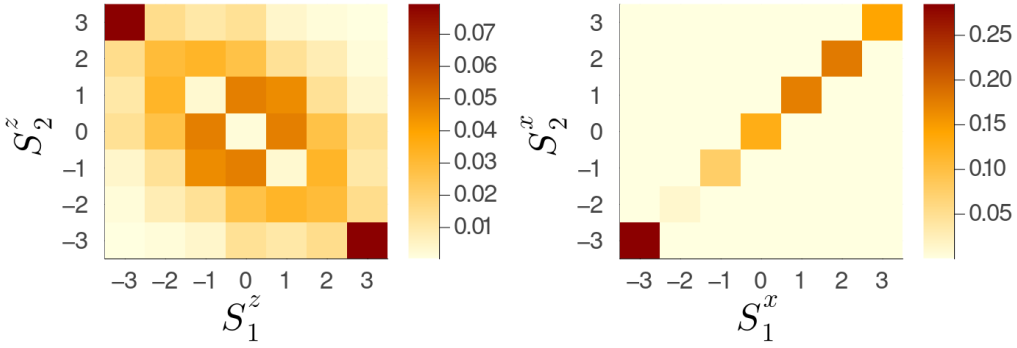

(d) $\alpha = -1/3$

Figure 3.7: Tomography of the state obtained at $t = t_{cat}$, for $N = 2$ spins of length $S = 3$ for (a) $\alpha = 0$, (b) $\alpha = 0.5$, (c) $\alpha = 1$ and (d) $\alpha = -1/3$ starting with a uniform initial state.

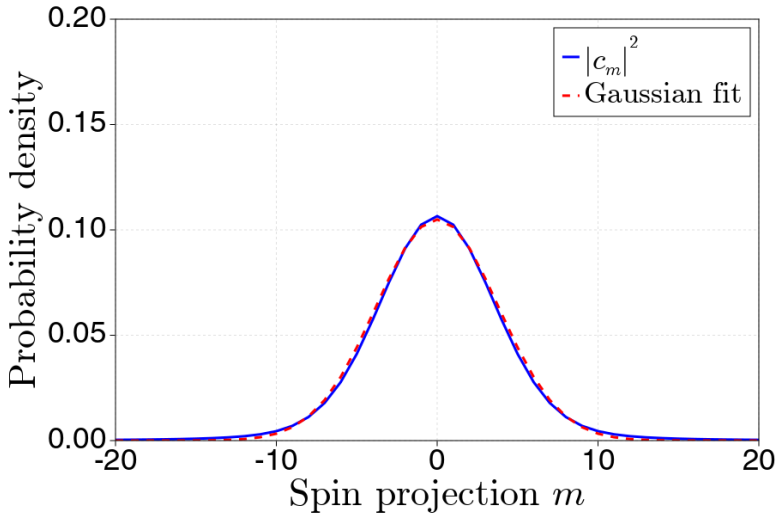

Figure 3.8: Weights $|c_m|^2$ of the wavefunction of the TSS along the $m_x^1 = m_x^2$ diagonal, with a gaussian fit, for $S = 20$. With our fit we have estimated that we have here a standard deviation $\sigma \sim 0.85\sqrt{S}$.

$$\left(\tilde{\Delta} J^{\alpha}\right)^2 = \mathrm{Var}\left(J^{\alpha}\right) - \sum_{i=1}^{N} \langle (S_i^{\alpha})^2 \rangle$$

and where α, β, γ is a permutation of x, y, z. There exist many such criteria, depending on which spin components we choose to be staggered, and which spin component we isolate in the right-hand term. We choose the following criterion:

$$\langle \left(\tilde{J}^{y}\right)^2 \rangle + \langle \left(\tilde{J}^{z}_{stag}\right)^2 \rangle - N\left(N-1\right) S^2 > \left(N-1\right) \left(\tilde{\Delta} J^{x}_{stag}\right)^2 . \tag{3.13}$$

This entanglement criterion is equivalent to the one obtained with the Dicke-squeezing parameter of Eq. 2.24, $\xi_D^2 < 1$, but with a different choice for α, β and γ. The authors of [96] present other criteria, but the one mentioned in Eq. 3.12 is the only one that detect entanglement during the dynamics with the dipolar Hamiltonian. In the case of only two spins, it can be rewritten in the following way:

$$E_{ent} = \mathrm{Var}\left(J^{x}_{stag}\right) + 2\langle S_1^z S_2^z \rangle - 2\langle S_1^y S_2^y \rangle - \langle (S_1^x)^2 \rangle - \langle (S_2^x)^2 \rangle + 2S^2 < 0. \tag{3.14}$$

Any separable state has $E_{ent} \geq 0$, so that finding $E_{ent} < 0$ for a given quantum state means that this state is entangled. From this expression, it is clear why the TSS state is a good candidate for an entangled state for this criterion, as it has a vanishing variance of J^x_{stag}, anticorrelations along z - which leads to a negative $\langle S_1^z S_2^z \rangle$ - and a non-zero variance of S_1^x and S_2^x.

In order to verify this assumption, we study the temporal evolution of this quantity for different values of B_q, first starting with a uniform initial state. We show the results for a few values of B_q between 0 and J in figure 3.9. As we can see, for the cases where we expect to form a cat state or a TSS state during the time evolution - namely $B_q = J/4$ and $B_q = 3J/4$ - we clearly have E_{ent} that becomes negative, which signals entanglement in the system. Surprisingly, E_{ent} vanishes at the time at which we expect the cat state or the TSS to form. This means that the above criterion is not able to detect entanglement for those states event though they are clearly entangled - for instance the TSS has a finite entanglement entropy, which grows as

$\log(S)$ with the spin length S. Still, we can see that the above entanglement criterion detects entanglement when the time evolution leads to a cat-like state (even though not in the case of the perfect cat state for $B_q = J/4$), while it remains positive at almost all time when this is not the case - see e.g. the case $B_q = 0$.

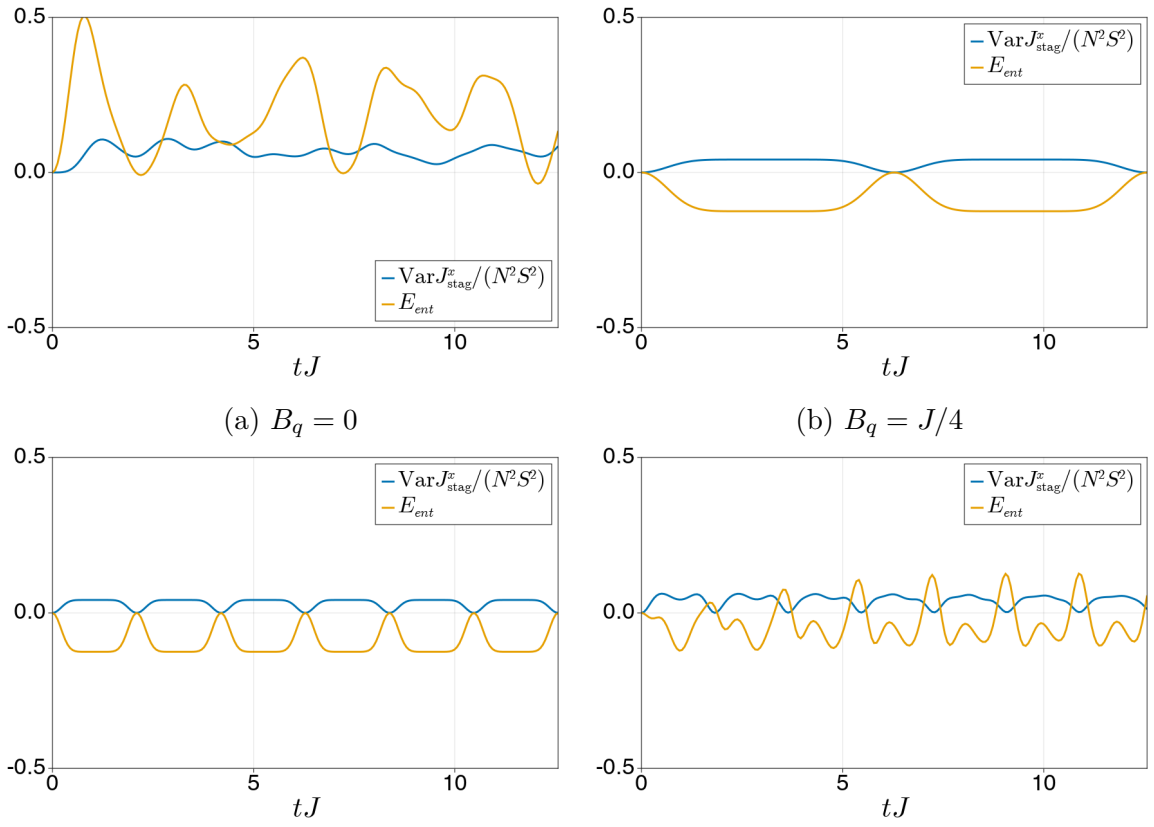

(a) $B_q = 0$ (b) $B_q = J/4$

(c) $B_q = 3J/4$ (d) $B_q = J$

Figure 3.9: Time evolution of Var $\left(J^x_{stag}\right)$ and E_{ent} starting with a uniform initial state, with the XXZ dipolar Hamiltonian with $N = 2$ spins of length $S = 3$ and for different values of B_q.

In a similar manner, we also studied the entanglement generated in the dynamics, starting with a staggered initial state. For this purpose, we define a second entanglement criterion, taking a different staggered spin:

$$\langle\left(\tilde{J}^y_{stag}\right)^2\rangle + \langle\left(\tilde{J}^z_{stag}\right)^2\rangle - N\left(N-1\right)S^2 > \left(N-1\right)\left(\tilde{\Delta}J^x\right)^2 \tag{3.15}$$

which leads to:

$$E^{stag}_{ent} = \text{Var}\left(J^x_{stag}\right) + 2\langle S^z_1 S^z_2\rangle - 2\langle S^y_1 S^y_2\rangle - \langle (S^x_1)^2\rangle - \langle (S^x_2)^2\rangle + 2S^2 < 0. \tag{3.16}$$

We show the time evolution of Var (J^x) and E^{stag}_{ent} in figure 3.10. Again, we can verify that the criterion detects entanglement in the dynamics leading to a cat-like state for $B_q < 0.75$, while it does not detect entanglement otherwise ($B_q = 1$).

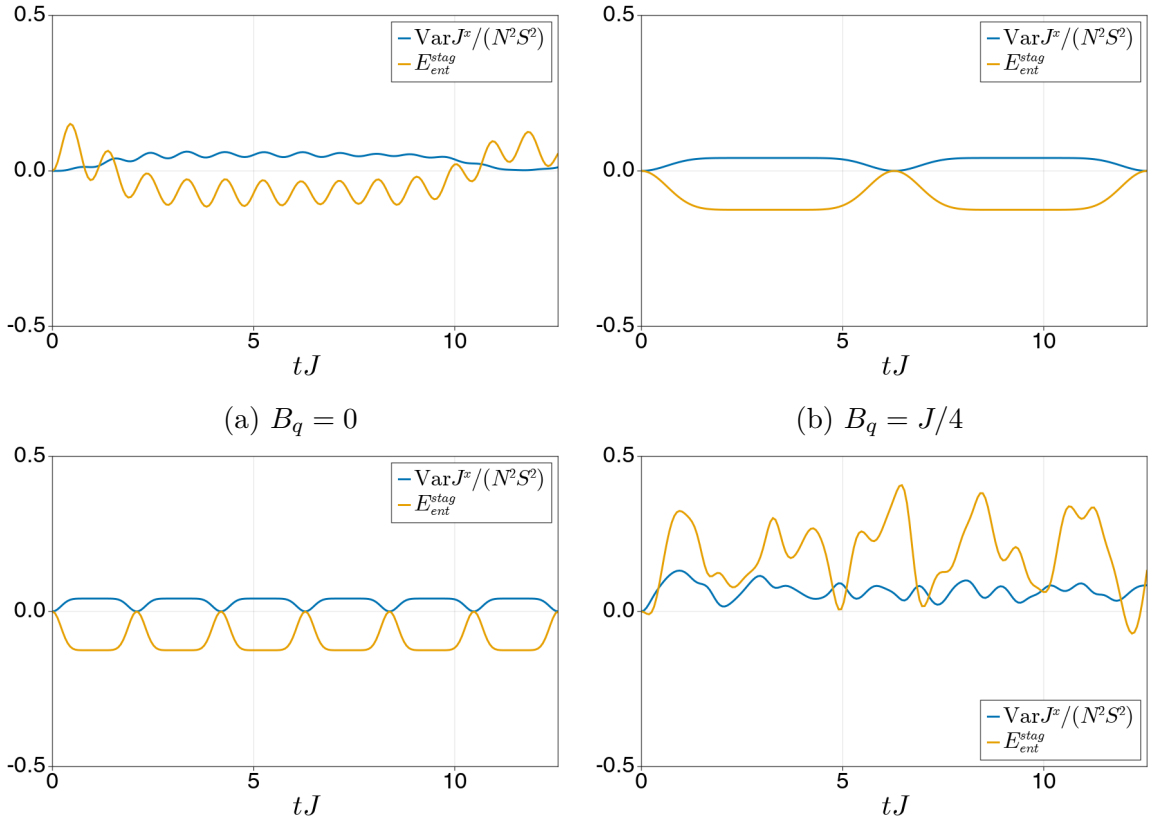

(a) $B_q = 0$ (b) $B_q = J/4$

(c) $B_q = 3J/4$ (d) $B_q = J$

Figure 3.10: Time evolution of $\mathrm{Var}(J^x_{stag})$ and E^{stag}_{ent} starting with a staggered initial state, with the XXZ dipolar Hamiltonian with $N = 2$ spins of length $S = 3$ and for different values of B_q.

3.2 Extension to 1D chains

In this section, we consider the case of a 1D chain of spins, and we investigate which of the properties of the $N = 2$ case resist when going to the case of a 1D chain with larger N. First, we study the time evolution starting from the uniform and staggered initial state with the dipolar XXZ Hamiltonian. In particular, we will determine to what extent this dynamics can still produce cat-like states depending on the value of B_q, and show that it is possible to realise larger and larger cat states in the staggered case. We will then contrast these results with what would be expected in the presence of thermalization.

3.2.1 Time evolution after a quench

Dynamics from a staggered initial state. In order to study the case of N spins initialized in the staggered coherent spin state $|S_x\rangle \otimes |-S_x\rangle \otimes |S_x\rangle \otimes \ldots$, we first define a generalisation of C^{2S}, namely the coherence of NS-th order:

$$C^{NS}(t) = |\langle\psi(t)| \left(S_1^+ S_2^- S_3^+ \cdots S_N^{\pm}\right)^{2S} |\psi(t)\rangle| / \mathcal{N}_{cat} \tag{3.17}$$

with S_N^+ for N odd and S_N^- for N even, and $\mathcal{N}_{cat}$ the normalization factor defined by:

$$\mathcal{N}_{cat} = \frac{1}{2} \prod_{m=-S}^{S-1} \sqrt{S\,(S+1) - m\,(m+1)}^{N}. \tag{3.18}$$

We show in figure 3.11 the time evolution of C^{NS} in the case of $N = 3$ spins, for different values of B_q, and the evolution of C^{NS}_{max} and t_{max} versus B_q.

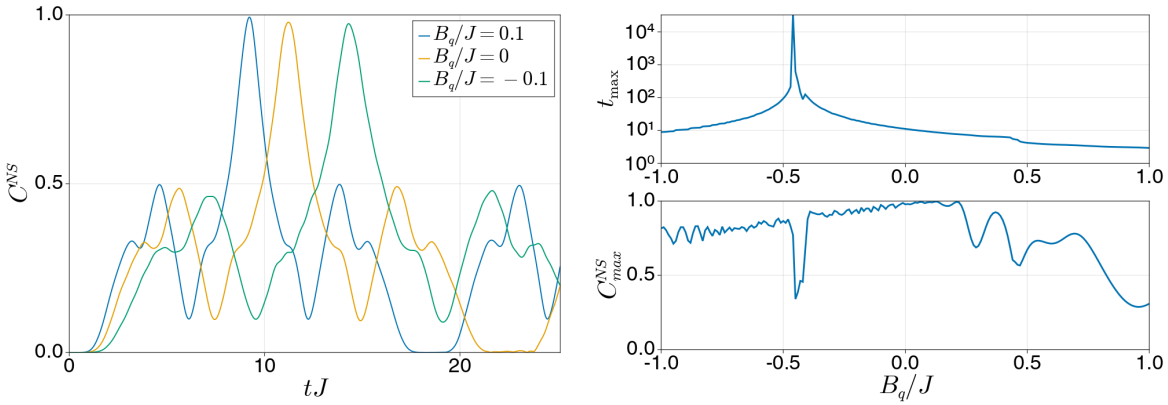

(a) (b)

Figure 3.11: (a) Time evolution of C^{NS} for different values of B_q, starting with a staggered initial state, with the XXZ dipolar Hamiltonian with $N = 3$ spins of length $S = 3$; (b) evolution of t_{max} and C^{NS}_{max} versus B_q for the same initial state and Hamiltonian.

As we can see, it is still possible to find values of B_q for which we can generate cat-like states (now with $N = 3$ spins), even though there is no value of B_q for which we have an exact OAT Hamiltonian, due to the power law decay of the interactions. Still, we can produce an almost perfect cat state for $B_q = 0.1J$, and we find a value $B_q^c \approx -0.46J$ for which dynamics slows down drastically (with a seemingly divergent t_{max} time as $t_{max} \sim 1/|B_q - B_q^c|$). The global picture is therefore very similar to the one of the $N = 2$ case, and we can wonder if it remains the same if we keep increasing N, or if it breaks down after a finite value of N.

We were able to study the evolution of C^{NS}_{max} with B_q in the case $N = 4$, and we show our results of figure 3.12. Again, we could find a few values of B_q, for which the unitary dynamics starting from a staggered CSS can produce a state close to a perfect cat state.

Due to numerical limitations, we could not study larger system sizes in a systematic way. Still, we were able to study the time evolution of C^{NS} for a few values of B_q, up to $N = 6$, using Lanczos algorithm instead of the full diagonalization of the Hamiltonian. As shown in figure 3.13, for each N up to $N = 6$ we could find a value of B_q for which we generate during the unitary dynamics a state close to a cat state. It is clear from the figure that the larger N, the longer the time needed to reach a cat state, but also the lower the maximum value of C^{NS} is. For larger values of N the value of B_q leading to a cat-like state in the dynamics needs to be increasingly fine-tuned. For $N = 6$, changing $B_q = -0.3J$ by an amount $\pm\delta B = 0.1J$ was enough to eliminate completely the cat-generating dynamics.

Even though our exact diagonalization results are limited to small system sizes, we will discuss in the next chapter an approximate theoretical scheme that will allow us to study a larger number of spins N, and determine whether we can have OAT-like dynamics for longer 1D chains or not.

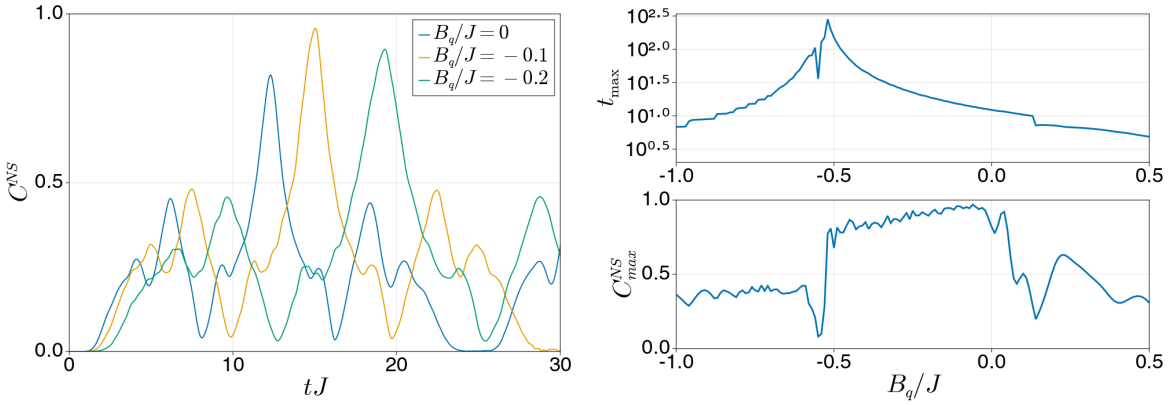

(a) (b)

Figure 3.12: (a) Time evolution of C^{NS} for different values of B_q, starting with a staggered initial state, with the XXZ dipolar Hamiltonian with $N = 4$ spins of length $S = 3$; (b) evolution of t_{max} and C^{NS}_{max} versus B_q for the same initial state and Hamiltonian.

Dynamics from a uniform initial state. In the uniform case, we define in a similar way a generalization of C^{2S}:

$$C^{NS}(t) = |\langle\psi(t)| \left(S_1^+ S_2^+ S_3^+ \cdots S_N^+\right)^{2S} |\psi(t)\rangle| / \mathcal{N}_{cat}. \tag{3.19}$$

As in the staggered case, we show in figure 3.14 the time evolution of C^{NS} for a few values of B_q, as well as the dependence of C^{NS}_{max} with B_q. As we can see, the situation seems to degrade faster upon increasing the system size for the uniform initial state than for the staggered initial state when increasing N. Even for $N = 3$, we could not find a value of B_q for which we had $C^{NS}_{max} > 0.9$.

We expect that we find an even lower C^{NS}_{max} when increasing N, starting from a uniform initial state, therefore we will not study the case $N \geq 4$ here. It appears that it is not possible to form a cat-like state in 1D chains for a large number of sites N, starting with a uniform CSS. We will provide in the next chapter arguments that explain this observation, making use of an approximate separation of variable.

Metrologic interest of the generated state. As discussed in the first chapter, cat states are very interesting for metrology, since they allow for the most precise measurement of external fields via interferometric measurements. Indeed, we can show that the quantity C^{NS} is closely related to the metrological potential of the state under rotation along the x axis. If we consider a parity measurement, after a rotation of angle ϕ, defined by $U(\phi) = e^{-i\phi J^x}$, we get for a uniform cat state:

$$\langle\psi_{cat}|U^\dagger(\phi) \prod_{i=1}^{N} (2S_i^z)^{2S} U(\phi) |\psi_{cat}\rangle = 4\mathcal{N}_{cat} \cos(2NS\phi). \tag{3.20}$$

On the other hand, for a general state $|\psi\rangle$, we would get, for the fastest rotating terms:

$$\langle\psi|U^\dagger(\phi) \prod_{i=1}^{N} (2S_i^z)^{2S} U(\phi) |\psi\rangle = 4\mathcal{N}_{cat} C^{NS} \cos(2NS\phi) + \ldots \tag{3.21}$$

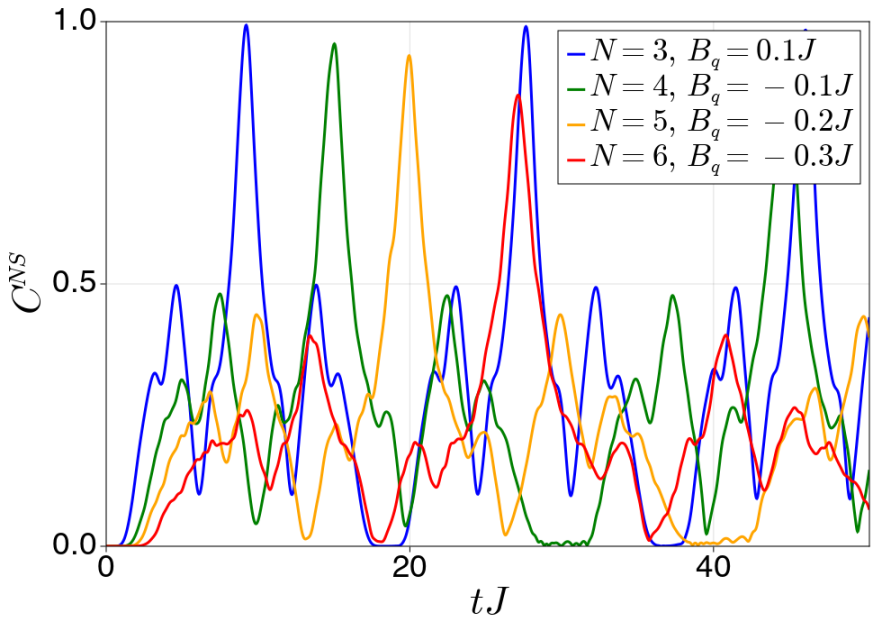

Figure 3.13: Time evolution of C^{NS} for different values of N and B_q starting from a staggered CSS.

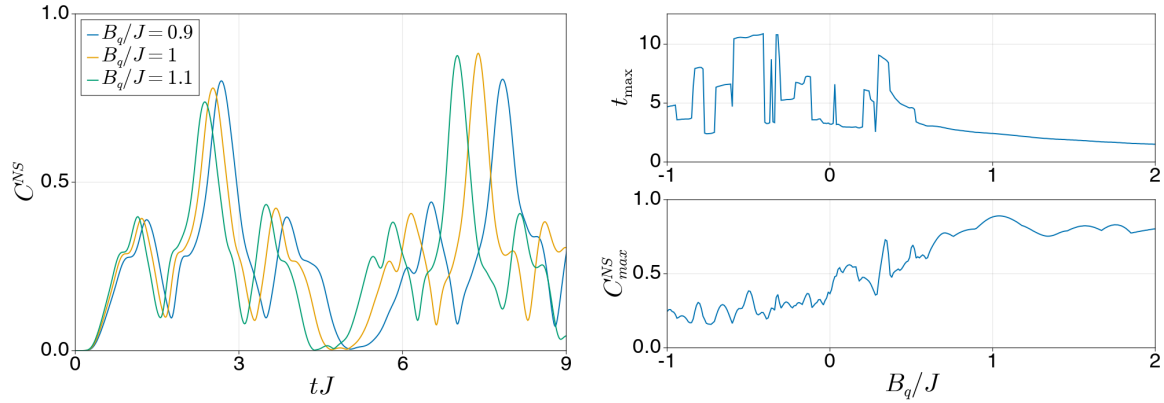

(a) (b)

Figure 3.14: (a) Time evolution of C^{NS} for different values of B_q, starting with a uniform initial state, with the XXZ dipolar Hamiltonian with $N = 3$ spins of length $S = 3$; (b) evolution of t_{max} and C^{NS}_{max} versus B_q for the same initial state and Hamiltonian.

with the slower rotating terms not expressed here. From this it is clear that the quantity C^{NS} we studied in this chapter expresses the contrast of parity oscillations under rotation of the state. In the case of N spins of length S, the uncertainty on the estimate of a rotation angle, $\delta\theta$, satisfies:

$$\delta\theta \gtrsim \frac{1}{2SN}, \tag{3.22}$$

since the quantum Fisher information for pure states is upper bounded by $4\mathrm{Var}\,(J^\mu) \leq 4N^2S^2$. However, as we saw in this section, trying to increase N by extending the linear size of the system leads to states that are further and further apart from an ideal cat state, reducing their metrological potential, in particular when taking a uniform CSS as initial state. Even though

extending linearly the system size is not a good way to increase the metrological potential of the state, there is another way to achieve this goal.

In fact, one could imagine reproducing this experiment with two spatially separated BEC, realizing de facto two giant spins with a very large effective S that would then be subjected to the ideal case presented before. This would be a way to realize giant cat states at long times, or highly squeezed states at short times - since the long-time dynamics can be quite sensitive to losses induced by dipolar relaxation [97]. An experiment with two separate dipolar BECs has already been realized [98], although it was initialized in a different state - namely a staggered CSS along z. Another advantage of this setup is that the time needed to reach a cat state - and other entangled states in the dynamics - only depends on the number of giant spins, and not their length, which makes it more advantageous to have two giant spins of size NS than a chain with $2N$ sites and a spin S on each site.

3.2.2 Time evolution vs. thermal equilibrium

As we saw in the previous subsection, starting with a staggered initial state, and choosing a proper value of B_q, it seems possible to generate cat-like states in chains of arbitrary length N. This result raises a lot of questions, especially regarding the thermalization of the system. On the one hand, cat states are non typical states at finite energy density, since they have very low entanglement entropy and extremely strong correlations for a thermal state, and we would not expect them to appear in the dynamics of systems obeying the ETH [7] (as presented in Chapter 1), and not conserving the total spin $\vec{J}^2_{stag}$. Indeed, ideal cat states are defined in the manifold of maximal collective-spin length, in which the initial state also lives. On the other hand, we know that whatever the value of B_q for $N \geq 3$, we should expect $\langle \vec{J}^2_{stag} \rangle$ to evolve in time. Also, for $N \geq 4$, with $S = 3$ or $S = 6$, the Hilbert space becomes sufficiently large for us to expect that the unitary dynamics of the system might display some features of thermalization. In this subsection we will try to address this apparent contradiction, by studying the time evolution of $\langle \vec{J}^2_{stag} \rangle$ and compare it to its expected thermal value. We will also study the properties of the eigenstates of the Hamiltonian for different values of B_q and determine which eigenstates are effectively involved in the dynamics starting from coherent spin states.

Evolution of $\langle \vec{J}^2_{stag} \rangle$. In order to determine if the system undergoes thermalization, we study the time evolution of the mean value of $\vec{J}^2_{stag}$ during the quench dynamics, for various values of B_q, and compare it to the thermal average (as expected if the system would thermalize) at a temperature corresponding to the energy of the initial state of the evolution. In particular, this will allow us to evaluate to what extent the dynamics leaks out of the sector of maximal spin length.

As introduced in chapter 1, we first define the temperature associated with the initial state of the evolution, T_0, verifying that the thermal average of $\mathcal{H}$ corresponds to the energy of the initial state:

$$\mathrm{Tr}\left(\rho\left(T_0\right)\mathcal{H}\right) = E_0 = \langle \psi_0 | \mathcal{H} | \psi_0 \rangle \tag{3.23}$$

with $\rho(T)$ the density matrix of the thermal state at temperature T. We can then compute the thermal average of any observable (i.e. the value it would take if the system reached thermalization) as $\langle \mathcal{O} \rangle = \mathrm{Tr}\left(\rho\left(T_0\right)\mathcal{O}\right)$. The staggered initial state is a very high energy state and it would correspond to a negative temperature. Nonetheless, we can consider in all this

subsection the spectrum of $-\mathcal{H}$ instead of $\mathcal{H}$. This will change the spectrum but not the time evolution of observables of interest.

We compare the thermal average of $\vec{J}^2_{stag}$ to the time evolution of the same operator for different values of B_q and different chain lengths N, and we show our results in figure 3.15. As we can see, in the $N = 2$ case, we always have $\vec{J}^2_{stag}$ that remains very close to its initial value, and it is never close to the thermal value (even though $N = 2$ may be too small to see proper thermalization). However, for $N = 4$, we can see a clear difference between the dynamics at $B_q = 0$ or $B_q = -0.2J$ on the one hand, and the dynamics at $B_q = 0.25J$ or $B_q = 0.5J$ on the other hand. In the first case - for which we generate cat-like states during the dynamics - the mean value of $\vec{J}^2_{stag}$ is almost conserved; while in the second case it quickly relaxes to a value that is close to the thermal expectation value, and never goes back to its initial value. Note that in the second case we never form cat-like states during the dynamics. Therefore we can clearly see the crossover (when varying B_q) from a dynamics that seems to display thermalization to a dynamics not showing it at all. It is worth noticing that in both cases $\vec{J}^2_{stag}$ is never an exactly conserved quantity, hence the absence of thermalization is not the simple result of a conservation law. In order to understand this strange behaviour, we inspect the structure of the spectrum of our Hamiltonian.

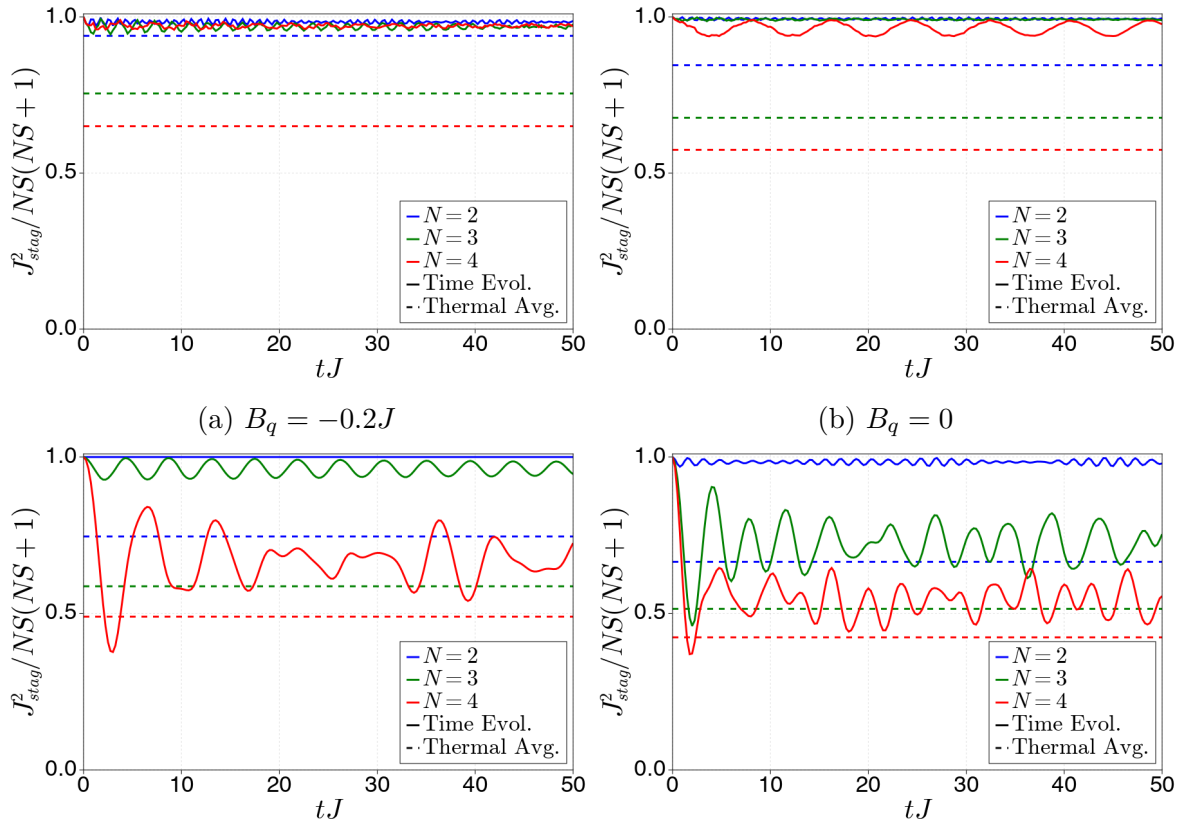

(a) $B_q = -0.2J$ (b) $B_q = 0$

(c) $B_q = 0.25J$ (d) $B_q = 0.5J$

Figure 3.15: Time evolution of $\vec{J}^2_{stag}$ (solid lines) and its thermal average (dashed lines) starting with a staggered initial state and with the dipolar XXZ Hamiltonian, for different values of N and different values of B_q.

Eigenstates and eigenvalues of the dipolar Hamiltonian. In order to understand better the origin of the non-thermal behaviour, we plot in figure 3.16 the eigenenergies as a function of $\langle \vec{J}^2_{stag} \rangle$, in order to identify the presence of eigenstates which are atypical from this point of view. We show the spectrum of $-\mathcal{H}$, for $B_q = -0.2J$ and $B_q = 0.5J$ in figure 3.16. We also highlight with red crosses the eigenstates $|\lambda\rangle$ for which the staggered initial state $|\psi_{stag}\rangle$ has the highest overlap, such that $|\langle\lambda|\psi_{stag}\rangle| > \delta$ with a threshold $\delta = 1/NS$.

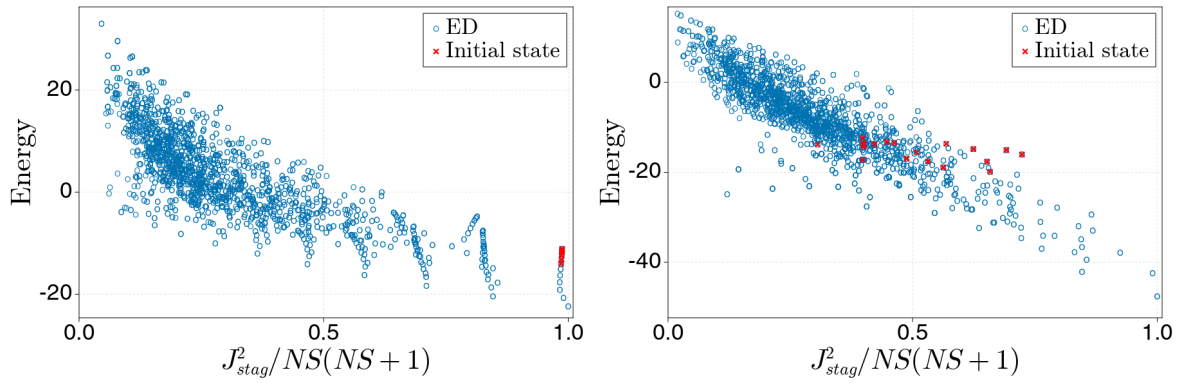

(a) $B_q = -0.2J$ (b) $B_q = 0.5J$

Figure 3.16: Eigenenergy versus mean value of $\vec{J}^2_{stag}$ for the different eigenstates of the dipolar XXZ Hamiltonian for $N = 4$ spins of length $S = 3$. Red crosses indicates states with which the staggered initial state has the highest overlap (see text).

As we can see in figure 3.16b, for $B_q = 0.5J$, the mean value of $\vec{J}^2_{stag}$ varies smoothly with the energy. This is what we would expect from a system obeying the ETH. Moreover we can notice that the initial state overlaps mostly with typical eigenstates, in the "bulk" of the spectrum. On the other hand, for $B_q = -0.2J$, we can see in figure 3.16a that there exist eigenstates with a very well defined value of $\vec{J}^2_{stag}$ close to its maximum value; they have a mean value of $\vec{J}^2_{stag}$ that is completely different from the one of all the other eigenstates with similar energy. These are also the states with which the initial state has the highest overlap. Therefore we are in the case of a violation of the ETH due to the phenomenon of quantum many-body scars [11], namely the existence of Hamiltonian eigenstates for which the mean value of a given observable is drastically different from that of most eigenstates with similar energy and from the thermal one. This is a weak violation of the ETH (as discussed in chapter 1) and it explains the persistence of cat-like states in the dynamics, in spite of an increasing chain length N.

3.3 Conclusions for this chapter

In this chapter, we have given examples of few-qudit entangled states we could generate during a quench dynamics with the dipolar XXZ Hamiltonian, starting either with a uniform or a staggered CSS. In particular, it is possible to generate perfect cat states in the case $N = 2$ by setting the value of B_q to $J/4$. While both initial states share a lot of common properties in the case $N = 2$, we observe drastic differences when increasing N, especially the fact that we can still generate cat-like states with a very good fidelity in the staggered case, up to $N = 6$, while they disappear in the uniform case. We provided some explanation of this behaviour in the

staggered case by looking at the (absence of) thermalization for different values of B_q. However, we could not study chains of length $N > 6$ with exact methods, and we can not conclude yet on the persistence of this dynamics for large systems. We will discuss more in details in the next chapter the case of large N using an approximate separation of variables.

Chapter 4

Scalable squeezing generation with the dipolar XXZ Hamiltonian

In this chapter, we address the question of the production of scalable spin squeezing and entanglement certification for arrays of magnetic atoms, interacting via the large-S dipolar XXZ Hamiltonian presented in section 2.3. In section 4.1, we first look at the thermodynamics of the Hamiltonian at the mean-field level, and study the low-energy spectrum with a linear spin-wave approach. In section 4.2 we then introduce a method based on an approximate rotor/spin-wave separation of variables which allows us to understand the emergence of spin squeezing in the spin models with spatially decaying interactions. We discuss its range of validity and benchmark it via exact results on small systems. Then in section 4.3 we present the results obtained with this new method for the quench dynamics of the dipolar XXZ model, and compare them with those obtained via a truncated cumulant expansion (TCE). Finally, in section 4.4 we try to connect the dynamics of the system with its thermodynamics by reconstructing the equilibrium phase diagram of the large-S dipolar XXZ model.

4.1 Equilibrium behaviour of the dipolar XXZ Hamiltonian

Unlike the previous chapter, where we only considered very small systems ($N \leq 6$), in the present chapter we want to study the case of large systems ($N \sim 10^2 - 10^4$) to match current experimental realisations and understand the scalability of the entangled states produced by the dynamics. In this context, it is interesting to study the thermodynamics of the large-S dipolar XXZ model in order to get some insight on the ground state properties and the low energy spectrum upon varying B_q. In this section, we will first present the mean-field phase diagram for the ground state of the dipolar Hamiltonian in 1D and 2D, and study how the ordered ground-state phases survive a finite temperature in 2D. Then we will study the low-energy spectrum of the Hamiltonian with a linear spin-wave (LSW) approach. In this section, we will focus on the case $S = 3$, which corresponds for instance to Chromium atoms; but we will also discuss the dependence on S of our results. The analysis of the equilibrium behaviour of the systems will allow us to assess whether the initial states for the dynamics (the uniform and staggered CSS, as introduced in the previous chapter) are low-energy or high-energy states for the evolution Hamiltonian. This will be very important in view of the application of the

rotor/spin-wave separation to our problem, and the appearance of scalable spin squeezing.

4.1.1 Mean-field phase diagrams

We start by studying the ground state of the XXZ Hamiltonian in the large N limit, using a mean-field approach. We recall that our Hamiltonian is the following:

$$\mathcal{H} = \sum_{i<j} V_{ij} \left(S_i^z S_j^z - \frac{1}{2} \left(S_i^x S_j^x + S_i^y S_j^y \right) \right) + B_q \sum_i (S_i^z)^2 \tag{4.1}$$

with

$$V_{ij} = \frac{J_0}{|r_i - r_j|^3} \tag{4.2}$$

as we will consider 1D or 2D systems defined on chains or planes orthogonal to the quantisation axis. The indices i, j run over the sites of a L-site chain (in 1D) or of a $L \times L$ square lattice (in 2D) with periodic boundary conditions.

We investigate the ground state of the Hamiltonian with a mean field approach, described in Appendix B.2, for various values of B_q/J and for $S = 3$. For each ground state, we look at the mean value of J^x/N and J^z_{stag}/N which are the order parameters for an xy ferromagnetic phase and a z Néel phase respectively. We show our results in figure 4.1. It appears clearly that in the case of the 2D square lattice, we have a persistent xy ferromagnetic order for a large range of values of B_q, ranging from 0 to $\approx 55J$, with an almost perfect ferromagnet ($\langle J^x \rangle / N \approx 1$) for small positive B_q. On the other hand, for the 1D chain, we only have a ground state with a long-range ferromagnetic order for small $B_q \lesssim 10J$ and we never reach a perfect ferromagnet. We should also point out that the prediction of long-range xy ferromagnetism in 1D may be an artefact of the mean-field approximation, and the true ground state may only possess quasi-long-range order. In the large B_q limit, on the other hand, we expect that the ground state becomes a product of single-spin Dicke states $|S = 3, m = 0\rangle$. Finally, in both cases, we have a long-range Néel order along the z direction for $B_q < 0$. The mean-field approach predicts a first order transition between the Néel and ferromagnet phase, at $B_q = 0.3J$ for the 1D case and $B_q = -0.9J$ for the 2D case.

In the previous chapter, we also saw that it is interesting to consider the dynamics initialized in a staggered CSS along the x axis. In particular, we saw that the staggered CSS can be close to the ground state of $-\mathcal{H}$ and it leads to the formation of highly entangled states via unitary dynamics in small 1D systems. Therefore we can investigate the presence of Néel order along the x axis for various values of B_q/J for the ground state of $-\mathcal{H}$. For the sake of convenience, we transform $\mathcal{H}$ by a rotation of an angle π around the z axis for every other site, leading to the following "staggered" Hamiltonian:

$$\mathcal{H}_{stag} = -\frac{1}{2} \sum_{i<j} V_{ij} \left(S_i^z S_j^z - \frac{(-1)^{i+j}}{2} \left(S_i^x S_j^x + S_i^y S_j^y \right) \right) - B_q \sum_i (S_i^z)^2 . \tag{4.3}$$

This transformation also maps the staggered CSS along x into the uniform CSS along x, and we can perform the same mean-field analysis as before. The only difference is that we should expect ferromagnetic xy order for negative B_q (penalising spins that tilt out of the xy plane), and ferromagnetic order along z (instead of a Néel order) for $B_q > 0$. We show the different phase diagrams for the 1D and 2D cases in figure 4.2. As expected, we can see that we have a

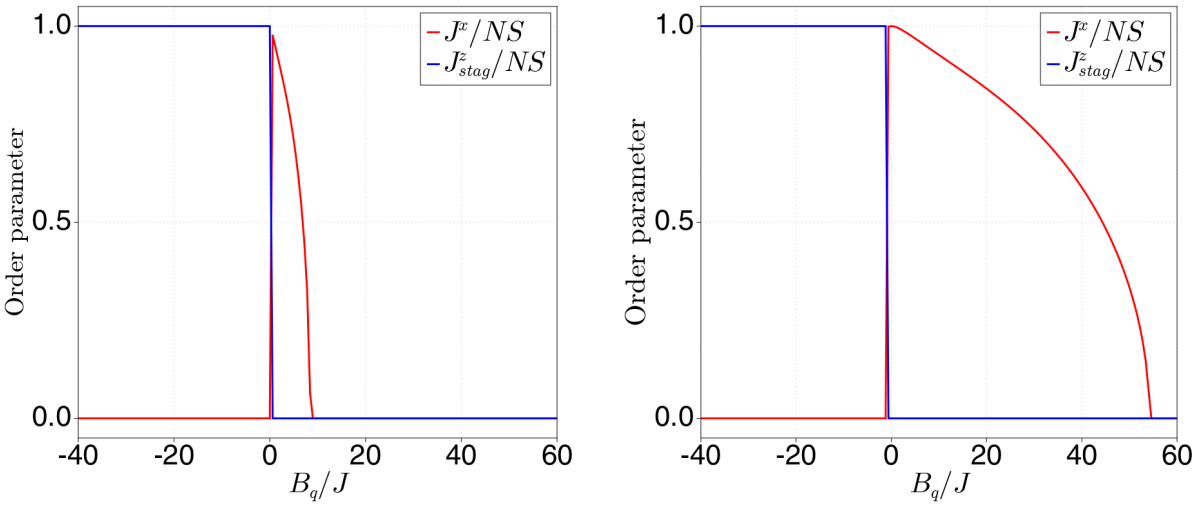

(a) 1D (b) 2D

Figure 4.1: Mean field phase diagram for the ground state of the dipolar XXZ Hamiltonian, with $S = 3$. The simulations have been performed for a 1D chain with length $L = 10^5$ and a 2D square lattice with $10^4 \times 10^4$ sites.

ferromagnetic phase along z for $B_q > 0$ for both the 1D and 2D cases. For the 1D case, only a small range of B_q ($-5.4J \lesssim B_q \lesssim -0.3J$) exhibits ferromagnetic order in the xy plane, which is similar to the 1D uniform case. However, for 2D, we see a major difference with the uniform case, as we have only imperfect ferromagnetic order in the xy plane and for a smaller range of values of B_q ($-16.2J \lesssim B_q \lesssim -3.9J$) compared to the uniform case. This can be easily understood as the long-range nature of the dipolar interactions introduce frustration for the staggered Hamiltonian, which destabilises the long-range order in the xy plane.

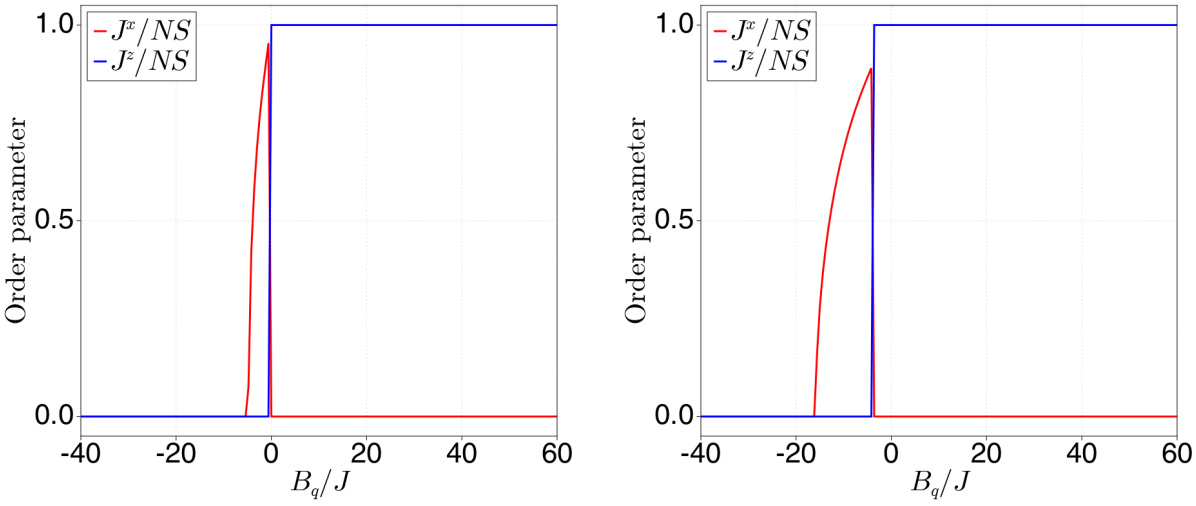

(a) 1D (b) 2D

Figure 4.2: Mean field phase diagram for the ground state of $-\mathcal{H}_{stag}$, with $S = 3$. The simulations have been performed for a 1D chain with length $L = 10^5$ and a 2D square lattice with $10^4 \times 10^4$ sites.

We now have a first idea of the ground state of the large-S dipolar Hamiltonian. The mean-field approach is not always suited for low dimensional systems, especially so for 1D chains, but we expect our results to be more reliable in 2D, especially in the presence of long-range interactions. In the following, we will only focus on 2D square lattices, and we test whether long-range order in the ground state survives at finite temperature or not. For this, we construct the mean field phase diagram at each temperature T, and determine whether we have a long-range order in the thermal state. The detailed procedure is presented in Appendix B.2. This allows us to determine for each value of B_q a critical temperature T_c at which the long-range xy order vanishes. We show our results in figure 4.3. Similarly to the case at $T = 0$, we see that we have a persistent long-range order in the xy plane for the uniform case for a wide range of values of B_q, and for relatively high temperatures up to $T \approx 20J$. On the other hand, for the staggered case, we see that long-range order in the xy plane is much more fragile to temperature, vanishing for $T \gtrsim 8J$. Again, this can be understood from the presence of magnetic frustration in the staggered case due to long-range interactions.

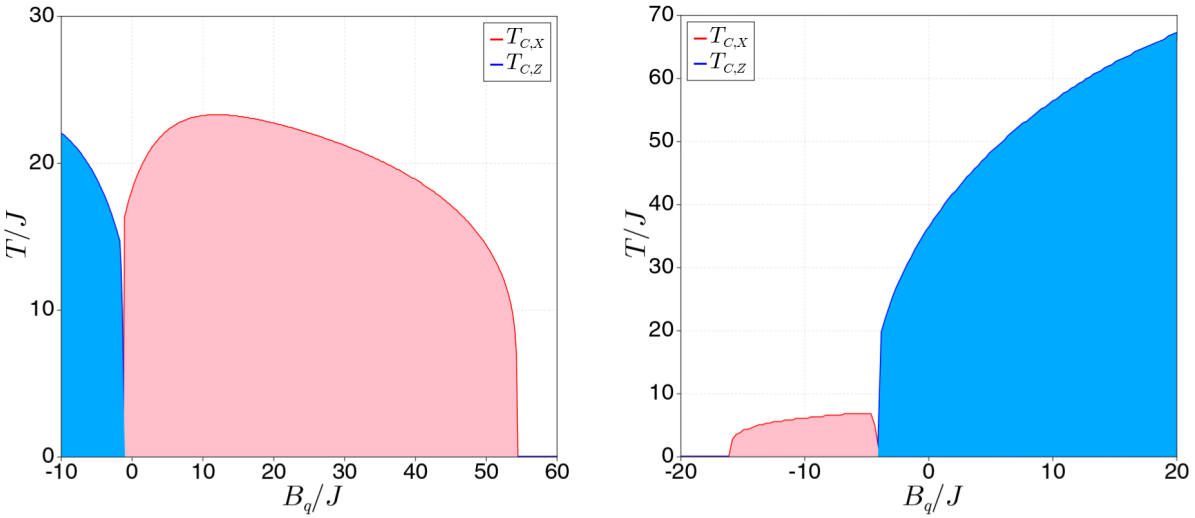

(a) $\mathcal{H}$ (b) $-\mathcal{H}_{stag}$

Figure 4.3: Critical temperature for the different order parameters in the thermal state in function of B_q, for (a)$\mathcal{H}$ and (b)$-\mathcal{H}_{stag}$, with $S = 3$ and for a $10^4 \times 10^4$ square lattice.

As already mentioned, mean-field results are not exact in the limit of low-dimensional systems. We will come back to these results and compare them with the ones of exact unbiased Quantum Monte Carlo simulations in section 4.4. Still, MF simulations give us an intuition on the ground state of the system for different values of B_q and of the proximity of the uniform and staggered CSS to the ground state. We now move beyond the MF approach and study the low-energy excitations of the system via the LSW approach.

4.1.2 LSW spectrum

The low-energy excitations of the dipolar Hamiltonian, both in the uniform and staggered case, can be studied in the form of Linear Spin Waves (LSW). For this purpose, we need to rewrite the Hamiltonian in terms of bosonic operators in momentum space, which then allow us to clearly identify the different excitation modes. The general procedure is the following:

1. We use the Holstein-Primakoff transformation to map our spins onto bosons in real space.

2. We Fourier transform the local bosonic operators into momentum-space bosonic operators.

3. We keep only quadratic terms for the bosons with finite momentum and use a Bogolyubov transformation to diagonalize the quadratic Hamiltonian.

We will detail in this subsection each of these different steps.

Holstein-Primakoff transformation. First we write down the Holstein-Primakoff transformation for our Hamiltonian, as introduced in Eq. 2.19. For this transformation, we need to choose a reference state on each site which corresponds to the bosonic vacuum. In order to study the low-energy spectrum of the system. This state needs to be the best approximation to the Hamiltonian ground state in the form of a CSS. Since we are interested in the ferromagnetic xy phase, we will choose as our bosonic vacuum the CSS along x for all the sites of our 1D chain or 2D square lattice. This corresponds to writing the local spin operators in the following way:

$$\begin{aligned} S_i^x &= -\tilde{S}_i^z = S - b_i^\dagger b_i \\ S_i^y &= \tilde{S}_i^y = \frac{\tilde{S}_i^+ - \tilde{S}_i^-}{2i} = \frac{\sqrt{2S - b_i^\dagger b_i}\; b_i - b_i^\dagger \sqrt{2S - b_i^\dagger b_i}}{2i} \\ S_i^z &= \tilde{S}_i^x = \frac{\tilde{S}_i^+ + \tilde{S}_i^-}{2} = \frac{\sqrt{2S - b_i^\dagger b_i}\; b_i + b_i^\dagger \sqrt{2S - b_i^\dagger b_i}}{2} \end{aligned} \tag{4.4}$$

where the $\tilde{S}^\alpha$ operators are mapped onto bosons via the HP transformation (see Eq. 2.19). Standard spin-wave theory amounts to linearizing this HP transformation under the assumption of a dilute gas of bosonic excitations, $n_i = b_i^\dagger b_i \ll 2S$, which assumes that the quantum ground state is close to the initial CSS. Keeping only the linear and quadratic terms, we obtain:

$$\begin{aligned} S_i^x &= S - b_i^\dagger b_i \\ S_i^y &\approx \sqrt{2S}\, \frac{b_i - b_i^\dagger}{2i} \\ S_i^z &\approx \sqrt{2S}\, \frac{b_i + b_i^\dagger}{2}. \end{aligned} \tag{4.5}$$

In the uniform case, this leads to the quadratic Hamiltonian $\mathcal{H} \approx E_{CSS} + \mathcal{H}_2$ with:

$$\begin{aligned} E_{CSS} &= -\frac{S^2}{2} \sum_{i<j} V_{ij} + \frac{NSB_q}{2} \\ \mathcal{H}_2 &= \frac{S}{4} \sum_{i<j} V_{ij} \left(2b_i^\dagger b_i + 2b_j^\dagger b_j + b_i^\dagger b_j + b_i^\dagger b_j + 3\left(b_i^\dagger b_j^\dagger + b_i b_j \right) \right) \\ &\quad + \frac{SB_q}{2} \sum_i \left(2b_i^\dagger b_i + b_i^\dagger b_i^\dagger + b_i b_i \right). \end{aligned} \tag{4.6}$$

Here E_{CSS} corresponds to the energy of the initial state. In the case of the staggered Hamiltonian, we have instead, with $-\mathcal{H}_{stag} \approx E_{CSS}^{stag} + \mathcal{H}_2^{stag}$:

$$\begin{aligned}
E_{CSS}^{stag} &= \frac{S^2}{2}\sum_{i<j}(-1)^{i+j}V_{ij} - \frac{NSB_q}{2} \\
\mathcal{H}_2^{stag} &= \frac{S}{4}\sum_{i<j}V_{ij}\left[-2(-1)^{i+j}b_i^\dagger b_i - 2(-1)^{i+j}b_j^\dagger b_j + ((-1)^{i+j}-2)(b_i^\dagger b_j + b_i^\dagger b_j)\right] \\
&\quad - \frac{S}{4}\sum_{i<j}V_{ij}((-1)^{i+j}+2)\left(b_i^\dagger b_j^\dagger + b_i b_j\right) - \frac{SB_q}{2}\sum_i\left(2b_i^\dagger b_i + b_i^\dagger b_i^\dagger + b_i b_i\right). \qquad (4.7)
\end{aligned}$$

In the following, we will focus on the case of the uniform Hamiltonian, and we will give the final result for the staggered Hamiltonian toward the end of the subsection.

Fourier transform and Bogolyubov transformation. Standard spin-wave theory amounts to taking the Fourier transform of the bosonic operators:

$$b_i = \frac{1}{\sqrt{N}}\sum_{\vec{q}} e^{i\vec{q}\cdot\vec{r}_i}b_{\vec{q}}, \qquad (4.8)$$

where $\vec{q}$ is defined on the Brillouin zone of the lattice. The resulting quadratic Hamiltonian takes the form:

$$\mathcal{H}_2 = \frac{1}{2}\sum_{\vec{q}}\begin{pmatrix} b_{\vec{q}}^\dagger \\ b_{-\vec{q}}\end{pmatrix}^T\begin{pmatrix}\mathcal{A}_{\vec{q}} & \mathcal{B}_{\vec{q}} \\ \mathcal{B}_{\vec{q}} & \mathcal{A}_{\vec{q}}\end{pmatrix}\begin{pmatrix} b_{\vec{q}} \\ b_{-\vec{q}}^\dagger\end{pmatrix} - \frac{1}{2}\sum_{\vec{q}}\mathcal{A}_{\vec{q}} \qquad (4.9)$$

with

$$\mathcal{A}_{\vec{q}} = S\left(\frac{\tilde{V}_0}{2} + \frac{\tilde{V}_{\vec{q}}}{4} + B_q\right), \quad \mathcal{B}_{\vec{q}} = S\left(\frac{3\tilde{V}_{\vec{q}}}{4} + B_q\right), \qquad (4.10)$$

where $\tilde{V}_{\vec{q}} = \frac{1}{N}\sum_{i\neq j}e^{-i\vec{q}\cdot(\vec{r}_i-\vec{r}_j)}V_{ij}$ is the Fourier transform of the interactions. We then introduce the Bogolyubov operators $a_{\vec{q}}^\dagger$ and $a_{\vec{q}}$, such that:

$$b_{\vec{q}} = u_{\vec{q}}a_{\vec{q}} - v_{\vec{q}}a_{-\vec{q}}^\dagger \qquad (4.11)$$

with

$$\begin{aligned}
E_{\vec{q}} &= \sqrt{\mathcal{A}_{\vec{q}}^2 - \mathcal{B}_{\vec{q}}^2} = \frac{S}{2}\sqrt{\left(\tilde{V}_0 - \tilde{V}_{\vec{q}}\right)\left(\tilde{V}_0 + 2\tilde{V}_{\vec{q}} + 4B_q\right)}, \\
u_{\vec{q}}^2 &= \frac{\mathcal{A}_{\vec{q}}}{2E_{\vec{q}}} + \frac{1}{2}, \quad v_{\vec{q}}^2 = \frac{\mathcal{A}_{\vec{q}}}{2E_{\vec{q}}} - \frac{1}{2}. \qquad (4.12)
\end{aligned}$$

We then finally obtain a Hamiltonian in the diagonal form:

$$\mathcal{H}_2 = \sum_{\vec{q}}E_{\vec{q}}a_{\vec{q}}^\dagger a_{\vec{q}} + \frac{1}{2}\sum_{\vec{q}}\left(E_{\vec{q}} - \mathcal{A}_{\vec{q}}\right) \qquad (4.13)$$

which allows to compute easily the time evolution of the $a_{\vec{q}}$, $a_{\vec{q}}^\dagger$ operators. However, we can notice immediately that we have a vanishing energy $E_0 = 0$ for $\vec{q} = 0$ for all values of B_q, which means that the Bogolyubov transformation is ill-defined for $\vec{q} = 0$. This suggests that it is not possible to treat the zero-momentum b bosons in the same way as the finite-momentum bosons.

They will therefore be treated separately, as we will see in the next section, and for the moment we will focus only on the finite-momentum modes $\vec{q} \neq 0$.

In the case of the staggered Hamiltonian, we get similar results, with:

$$\mathcal{A}_{\vec{q}} = S\left(\frac{\tilde{V}_0}{2} + \frac{\tilde{V}_{\vec{q}}}{2} - \frac{\tilde{V}^{(s)}_{\vec{q}}}{4} + B_q\right), \quad \mathcal{B}_{\vec{q}} = S\left(\frac{\tilde{V}_{\vec{q}}}{2} + \frac{\tilde{V}^{(s)}_{\vec{q}}}{4} + B_q\right). \tag{4.14}$$

where we have defined the following interaction:

$$V^{(s)}_{ij} = \frac{J_0(-1)^{i+j}}{|\vec{r}_i - \vec{r}_j|^3}, \tag{4.15}$$

and we note $\tilde{V}^{(s)}_{\vec{q}}$ its Fourier transform.

Numerical results. We now have all the ingredients needed to study the time evolution of spin-wave excitations in a system of spins initialised in a uniform CSS along x. In particular, we look at the spectrum predicted by LSW theory and the values of B_q at which we expect a breakdown of the theory - which corresponds to having at least a momentum $\vec{q} \neq 0$ for which we have $E^2_{\vec{q}} < 0$. In the uniform case, we have:

$$E^2_{\vec{q}} = \frac{S^2}{4}\left(\tilde{V}_0 - \tilde{V}_{\vec{q}}\right)\left(\tilde{V}_0 + 2\tilde{V}_{\vec{q}} + 4B_q\right) \tag{4.16}$$

where $\tilde{V}_0 - \tilde{V}_{\vec{q}} > 0$ for any $\vec{q} \neq 0$ since the potential V_{ij} is positive. Therefore we expect that for each $\vec{q}$ there is a critical value of B_q, $B^{(c)}_q(\vec{q})$ - satisfying $B^{(c)}_q(\vec{q}) = -\tilde{V}_0/4 - \tilde{V}_{\vec{q}}/2$ - below which the second term becomes negative. The question is then: which is the first mode to develop an instability when decreasing B_q? We show in figure 4.4 the evolution of $E^2_{\vec{q}}$ with B_q for various values of $\vec{q}$ for small system sizes. A square lattice is symmetric under exchange of the two axes of the lattice. Moreover, the interaction is real, so that we have the same energy for positive and negative wavevector $\vec{q}$. Therefore we can restrict ourselves to wavevectors of the form (q_x, q_y) with $q_x \geq q_y \geq 0$. We can see in figure 4.4 that the modes for which we have the largest $B^{(c)}_q$ is the mode $\vec{q} = (\pi, \pi)$. This could have been expected, since it is the momentum mode that minimises the value of $\tilde{V}_{\vec{q}}$, signalling an instability of the system to Néel order along the z axis.

From this we can determine the critical field $B^{(c)}_q$ at which the LSW theory predicts a proliferation of excitations, which corresponds to the fact that our reference state is no longer close to the ground state of the Hamiltonian - indicating the transition from a ground state with ferromagnetic order in the xy plane to Néel order along the z axis. We can determine this critical field by computing $B^{(c)}_q(\pi, \pi)$ for increasing system size. We show our results in figure 4.5, which clearly indicates that in the thermodynamic limit we expect a transition at $B^{(c)}_q \approx -0.93J$ which is comparable with our mean-field result.

In the case of the staggered Hamiltonian, we get a very different behaviour. First, we expect that the energy square $E^2_{\vec{q}}$ of the different modes crosses 0 when increasing B_q (i.e. we expect a negative slope with B_q). This is indeed what we can observe in figure 4.6a. However, when we keep increasing the lattice linear size L, we observe a rapid softening of the modes, especially the ones at small wavevectors $\vec{q} = (2\pi/L, 0)$ (as shown in figure 4.6b). A softening is also observed for the uniform case, but it occurs for much larger values of L and at a slower rate.

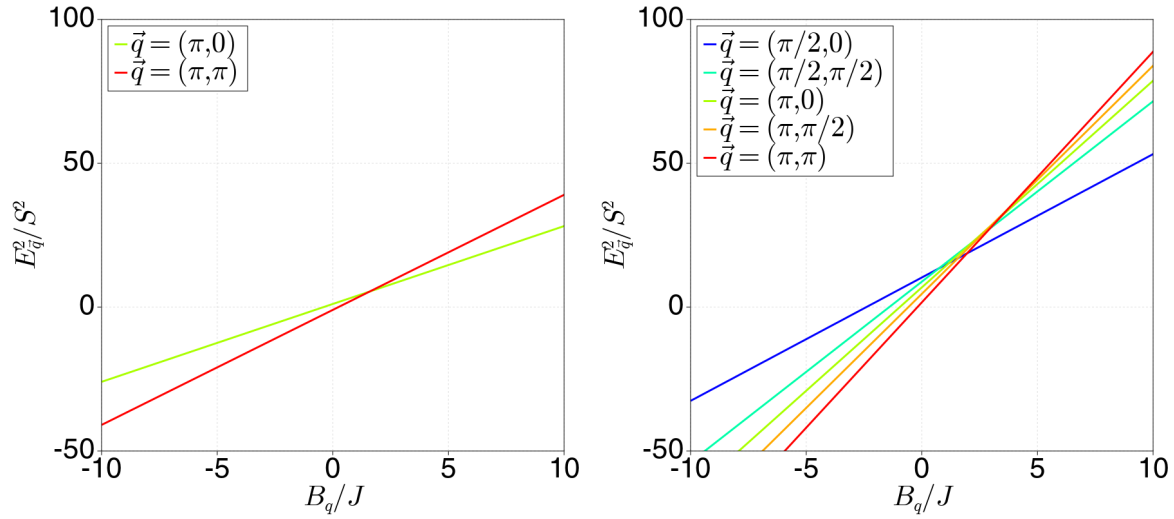

(a) $L = 2$ (b) $L = 4$

Figure 4.4: LSW spectrum for the uniform Hamiltonian $\mathcal{H}_2$ in function of B_q/J for (a) a 2×2 square lattice and (b) a 4×4 square lattice.

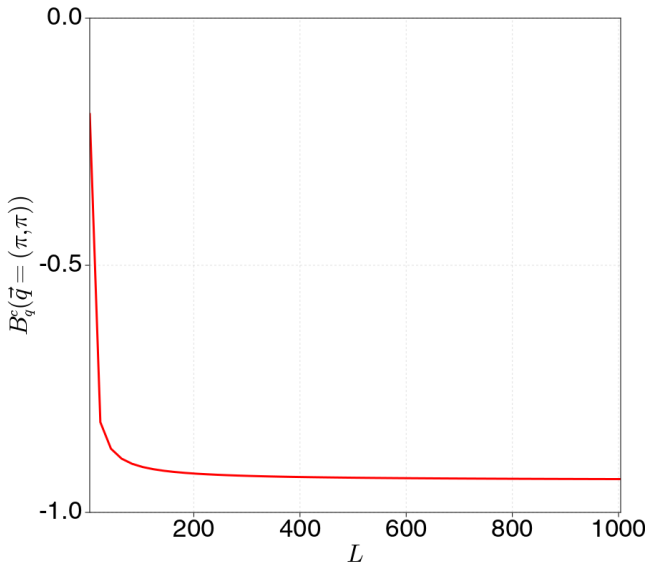

Figure 4.5: Critical value of B_q, $B_q^{(c)}(\pi,\pi)$ for increasing linear system size L, for the uniform quadratic Hamiltonian $\mathcal{H}_2$ on a square lattice.

The conclusion from LSW is therefore that long-range xy ferromagnetic order is not sufficiently stable in the case of the staggered Hamiltonian for LSW to be reliable. As a consequence, the staggered CSS is a low energy state for $-\mathcal{H}$ in 2D only on sufficiently small system sizes.

We also studied the LSW excitations in the 1D case, both for the uniform and staggered CSS. We show our results in figure 4.7. In both the uniform and staggered cases, we observe a rapid softening of the modes, similarly to the staggered case in 2D. From this we expect that the long-range order in the xy plane is stable only for sufficiently small system sizes.

This concludes our study of the equilibrium behaviour of the dipolar XXZ Hamiltonian for large-S spins. In particular, we have seen that we can expect ferromagnetic long-range order

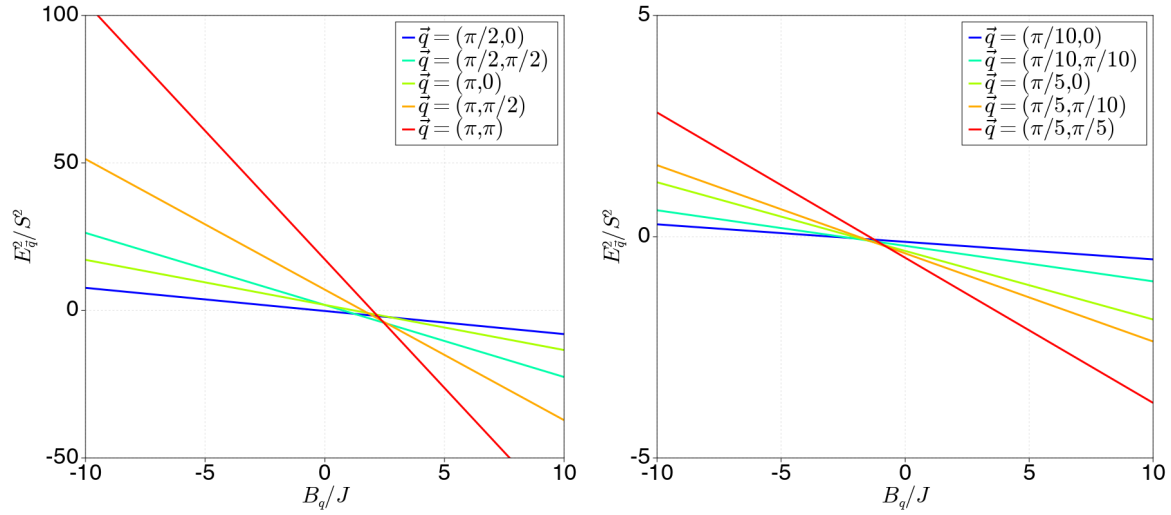

(a) $L = 4$ (b) $L = 20$

Figure 4.6: LSW spectrum for the staggered Hamiltonian $\mathcal{H}_2^{stag}$ in function of B_q/J for (a) a 4×4 square lattice and (b) a 20×20 square lattice.

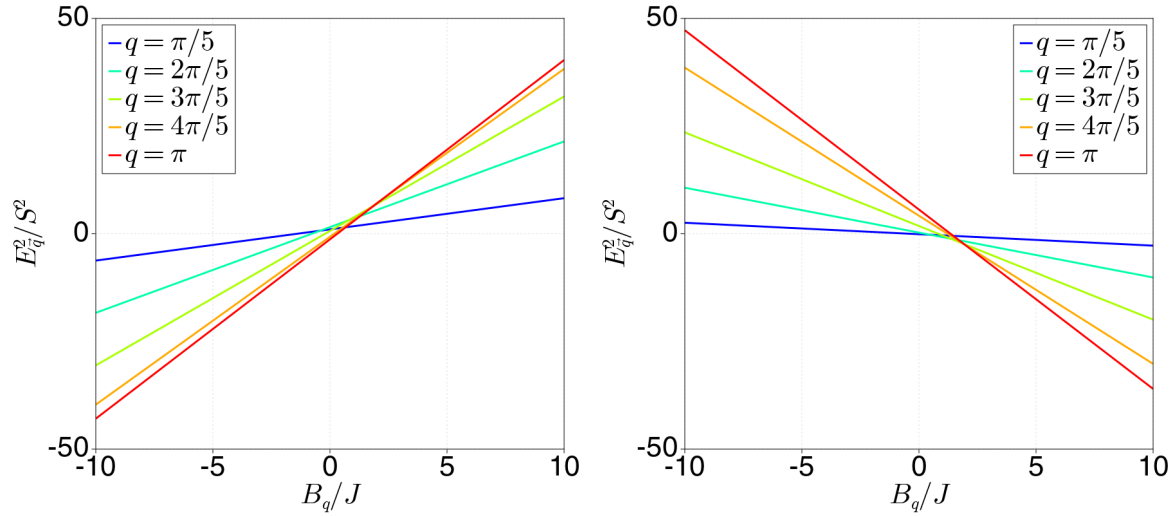

(a) $N = 10$ Uniform (b) $N = 10$ Staggered

Figure 4.7: LSW spectrum in function of B_q/J for a 1D chain of length $N = 10$ for (a) the uniform Hamiltonian $\mathcal{H}_2$ and (b) the staggered Hamiltonian $\mathcal{H}_2^{stag}$.

in the xy plane for a 2D square lattice; and it is therefore interesting to study the unitary dynamics of a CSS along the x axis, as the dynamics will be necessarily a low-energy one, possibly approaching the one of the OAT model, as we will see below. However, standard spin-wave theory may have problems in describing correctly the time evolution of such a quench, due to the presence of a zero-energy mode at $\vec{q} = \vec{0}$ whose bosons can proliferate at no energy cost. In the next section, we will propose a way to treat separately this mode within a rotor/spin-wave separation approximation. This will allow us to treat states which go arbitrarily far from the initial CSS.

4.2 Rotor/spin-wave approximation for the dipolar Hamiltonian

4.2.1 Derivation of the rotor/spin-wave separation

Numerical observations from the previous chapter clearly indicated that the dipolar Hamiltonian mimics to some extent the features of the OAT Hamiltonian. We want to further understand the origin of this correspondence, and probe whether it survives when increasing the system size, or whether it is just a finite-size effect in small systems. In order to do so, we develop an approximate separation of variables in the XXZ Hamiltonian, which allows us to write it as a planar rotor Hamiltonian, analogous to that of the OAT model, plus a correction coming from linear spin waves. Since we want to relate the dipolar XXZ Hamiltonian to the OAT model, we shall estimate the relative weight of these corrections. One can formally reconstruct a OAT Hamiltonian from the dipolar one by isolating the interaction term involving the zero-momentum Fourier component of the spin operators:

$$\begin{aligned}\sum_{ij} V_{ij} S_i^\mu S_j^\mu &= \frac{1}{N}\sum_{\vec{q}} V_{\vec{q}} S_{\vec{q}}^\mu S_{\vec{q}}^\mu \\ &= \frac{1}{N} V_0 \left(J^\mu\right)^2 + \frac{1}{N}\sum_{\vec{q}\neq 0} V_{\vec{q}} S_{\vec{q}}^\mu S_{\vec{q}}^\mu \end{aligned} \tag{4.17}$$

where $S_{\vec{q}}^\mu = \sum_i e^{i\vec{q}\cdot\vec{r}_i} S_i^\mu$, and $S_0^\mu = J^\mu$.

Nonetheless, the residual part, coupling finite-momentum components, does not commute with the zero-momentum one because of the spin $SU(2)$ algebra. An effective separation of variables can instead be achieved by mapping spins onto bosons, and separating zero-momentum and finite-momentum components of the Bose field. Limiting oneself to quadratic terms in the finite-momentum bosonic operators reconstructs LSW theory, which is augmented with a OAT Hamiltonian for a planar rotor, describing the arbitrarily non-linear dynamics of the zero-momentum bosons. This gives us the general guideline for the rotor/spin-wave (RSW) approach [99, 100]:

1. We use the Holstein-Primakoff transformation to map our spins onto bosons in real space.
2. We Fourier transform the local bosonic operators into momentum-space bosonic operators.
3. We regroup all the terms containing only zero-momentum bosons: they reconstruct exactly a OAT Hamiltonian for a macroscopic spin operator.
4. We keep only quadratic terms for the bosons with finite momentum and use a Bogolyubov transformation to diagonalize the quadratic Hamiltonian.

As we can see, the steps 1, 2 and 4 are exactly the same as in the LSW approach described in the previous section (excluding the $\vec{q} = \vec{0}$ mode), therefore we will focus on the third step in this section.

Zero momentum contribution. We want to isolate the contribution to the Hamiltonian of the zero momentum (ZM) bosons, at all orders and not only the lowest order. We define the ZM component of an operator $O^{[\mathrm{ZM}]}(\{b_i, b_i^\dagger\})$ as the part that contains exclusively $b_0, b_0^\dagger$

operators. From the definition of the Fourier transform, it is straightforward to see that for the local Bose operators:

$$b_i^{[\mathrm{ZM}]} = \frac{1}{\sqrt{N}} b_{\vec{q}=0}. \tag{4.18}$$

We can then extend this to the case of spin operators, and with the same HP mapping we introduced in the previous section (Eq. 4.4), we obtain:

$$\begin{aligned}
\left(S_i^x\right)^{[\mathrm{ZM}]} &= \left(-\tilde{S}_i^z\right)^{[\mathrm{ZM}]} = S - \frac{1}{N} b_0^\dagger b_0 = \frac{-\tilde{K}^z}{N} = \frac{K^x}{N} \\
\left(\tilde{S}_i^+\right)^{[\mathrm{ZM}]} &= \frac{b_0^\dagger}{\sqrt{N}} \sqrt{2S - \frac{b_0^\dagger b_0}{N}} = \frac{b_0^\dagger}{N} \sqrt{2SN - b_0^\dagger b_0} = \frac{\tilde{K}^+}{N}
\end{aligned} \tag{4.19}$$

where we note $\tilde{S}$ and $\tilde{K}$ the rotated operators, which gives us finally

$$\begin{aligned}
\left(S_i^x\right)^{[\mathrm{ZM}]} &= \frac{K^x}{N} \\
\left(S_i^y\right)^{[\mathrm{ZM}]} &= \frac{K^y}{N} \\
\left(S_i^z\right)^{[\mathrm{ZM}]} &= \frac{K^z}{N}
\end{aligned} \tag{4.20}$$

with $\vec{K}$ a macroscopic spin operator for a spin of length NS. This means that in the ZM component we can replace any local spin operator S_i^α by the spin operator K^α/N. Hence the ZM component of the Hamiltonian becomes:

$$\begin{aligned}
\mathcal{H}^{[\mathrm{ZM}]} &= \frac{1}{N^2} \sum_{i<j} J_{ij} \left(K^z K^z - \frac{1}{2} \left(K^x K^x + K^y K^y \right) \right) \\
&\quad + \frac{1}{N^2} B_q \sum_i \left(K^z\right)^2 \\
&= \frac{1}{2N} \tilde{V}_0 \left(K^z K^z - \frac{1}{2} \left(\vec{K}^2 - K^z K^z \right) \right) + \frac{B_q}{N} \left(K^z\right)^2
\end{aligned} \tag{4.21}$$

where $\vec{K}^2 = NS\left(NS+1\right)$ is a constant. After simplification, we obtain:

$$\mathcal{H}^{[\mathrm{ZM}]} = \chi_0 \left(K^z\right)^2 - \frac{\tilde{V}_0}{4} S(NS+1) \tag{4.22}$$

with $\chi_0 = \left(\frac{3}{2}\tilde{V}_0 + 2B_q\right) / \left(2N\right)$. We can rewrite χ_0 as $1/2I$, introducing a macroscopic moment of inertia $I \sim O(N)$. The ZM Hamiltonian is proportional to $\left(K^z\right)^2$, and we can identify it with the projection of the Hamiltonian onto the Dicke-state manifold as discussed below [99]. With this we have reconstructed exactly a planar rotor Hamiltonian, i.e. a OAT Hamiltonian.

RSW separation. The rotor/spin-wave separation of variables amounts then to define the finite-momentum (FM) Hamiltonian as $\mathcal{H}^{[\mathrm{FM}]} = \mathcal{H} - \mathcal{H}^{[\mathrm{ZM}]}$, and to approximate this Hamiltonian with its lowest-order term in the $b_{\vec{q}\neq 0}, b_{\vec{q}\neq 0}^\dagger$ operators, namely the spin-wave Hamiltonian at finite momentum:

$$\mathcal{H}^{[\mathrm{FM}]} \approx \mathcal{H}_2^{[\mathrm{FM}]} = \sum_{q\neq 0} E_q a_q^\dagger a_q \tag{4.23}$$

so that one obtains the approximate Hamiltonian

$$\mathcal{H} \approx \frac{(K^z)^2}{2I} + \sum_{\vec{q}\neq 0} E_q a_q^\dagger a_q + C \tag{4.24}$$

with $C = E_R + \frac{1}{2}\sum_{\vec{q}\neq 0}(E_{\vec{q}} - \mathcal{A}_{\vec{q}})$ a constant, and with E_R the ground state energy estimated from the ZM part (see Eq. 4.22). The Hamiltonian is now composed of two commuting terms, the rotor part at zero momentum and the spin-wave part at finite momentum. The state of the system is then described as the quantum state of the macroscopic $\vec{K}$ spin, and the state of the quadratic spin-wave modes. The latter is a gaussian state described in terms of the parameters:

$$F_{\vec{q}} = \langle b_{\vec{q}} b_{-\vec{q}} \rangle, \quad G_{\vec{q}} = \langle b_{\vec{q}}^\dagger b_{\vec{q}} \rangle. \tag{4.25}$$

Neglecting the higher-order terms in the FM bosons is legitimate, as long as those bosons form a dilute gas, namely:

$$N_{\text{bos}} = \sum_{\vec{q}\neq 0} G_{\vec{q}} \ll 2(N-1)S. \tag{4.26}$$

The time evolution of the system is then determined by the independent evolution of the rotor and of the SW degrees of freedom. Applying the separation of variables to all the observables we are interested in (i.e the collective spin, its variance and the squeezing parameter), we have:

$$J^x = K^x - N_{\text{bos}} \tag{4.27}$$

$$\text{Var}\,(J^x) = \text{Var}\,(K^x) - N_{\text{bos}}\,(2NS - 2\langle K^x \rangle + N_{\text{bos}})\,, \tag{4.28}$$

and at the lowest order correction, we have for the squeezing parameter:

$$\xi^2 = 2NS\frac{\min_\theta \text{Var}\left(J^\theta\right)}{\langle J^x \rangle^2} \approx 2NS\frac{\min_\theta \text{Var}\left(K^\theta\right)}{\langle K^x - N_{\text{bos}} \rangle^2}. \tag{4.29}$$

With this expression of the spin-squeezing parameter, it is clear why in the limit of small number of bosons N_{bos} we expect a OAT-like dynamics for the spin-squeezing parameter. In the case of the staggered Hamiltonian, the only modification for the rotor part is that we have to consider the following moment of inertia:

$$\frac{1}{2I^s} = \frac{\tilde{V}^s_{\vec{q}=0} + \frac{1}{2}\tilde{V}^s_{\vec{q}=0} + 2B_q}{2N}. \tag{4.30}$$

With this we have all the ingredients needed to study the time evolution of a system of spins initialised in a uniform or staggered array of CSS along $\pm x$. In the limit of a few bosonic excitations at finite momentum we can expect a OAT-like behaviour emerging even with spatially decaying interactions.

4.2.2 Benchmark of the RSW approach

Before looking at the prediction of RSW approach for large system sizes, we first check that it gives correct results in the limit of small systems by comparing with ED results. In this subsection, we will first look at the spectrum predicted by both methods, and then at the time evolution of observables starting with a uniform or staggered initial states.

Spectrum and tower of states. In order to test our approach, we first try to compare the spectrum predicted by the RSW theory to the exact spectrum computed with ED, for a small 2×2 plaquette. Since we decouple the rotor Hamiltonian from the spin-wave one, the eigenstates of the RSW model are given by a tensor product of eigenstates of both models. For the rotor part, the eigenstates are simply the Dicke states for a giant spin of length NS: $|NS, M\rangle$, $M \in [-NS, NS]$; while for the spin waves the eigenstates are labelled by the boson occupation number in each mode $\vec{q}$ for the Bogolyubov quasiparticles, $|\{n_{\vec{q}}^{(a)}\}\rangle$. This leads to the following energy for a state $|M, \{n_{\vec{q}}^{(a)}\}\rangle$:

$$E\left(M, \{n_{\vec{q}}^{(a)}\}\right) = E_{gs} + \frac{1}{2I} M^2 + \sum_{\vec{q}\neq 0} n_{\vec{q}}^{(a)} E_{\vec{q}} \tag{4.31}$$

where $E_{gs} = E_R + \frac{1}{2}\sum_{\vec{q}\neq 0}\left(E_{\vec{q}} - \mathcal{A}_{\vec{q}}\right)$ is the ground state energy. The rotor ground-state energy E_R can be estimated from Eq. 4.22 but this estimate can actually be improved substantially for small systems by defining the rotor or ZM Hamiltonian as the original spin Hamiltonian projected onto the Dicke manifold [99] spanned by the states $|NS, M\rangle$:

$$\mathcal{H}^{[\mathrm{ZM}]} = P_D \mathcal{H} P_D \tag{4.32}$$

with

$$P_D = \sum_{M=-NS}^{NS} |NS, M\rangle\langle NS, M| \tag{4.33}$$

the projector onto the Dicke-state manifold. Adapting the results of [99] to the case of large spins, and including a quadratic Zeeman field B_q, we obtain:

$$\begin{aligned}\mathcal{H}^{[\mathrm{ZM}]} = {} & E_{CSS}\left(B_q = 0\right) + \frac{\left(K^z\right)^2}{2\tilde{I}} \\ & + \left(B_q - \frac{3\tilde{V}_0}{4(N-1)}\right) \sum_{M=-NS}^{NS} \langle NS, M| \sum_i \left(S_i^z\right)^2 |NS, M\rangle |NS, M\rangle\langle NS, M|\end{aligned} \tag{4.34}$$

with $1/2\tilde{I} = 3\tilde{V}_0/4(N-1)$ and E_{CSS} defined in Eq. 4.6. Note that the difference between $1/2\tilde{I}$ and $1/2I$ (at $B_q = 0$) is of order $1/N$ and vanishes in the large N limit. We estimate numerically from exact diagonalization the contribution of the last term (namely the projection of $\left(S_i^z\right)^2$ on the largest Dicke manifold), and in particular we extract the coefficients of its expansion in powers of K^z:

$$\begin{aligned}\left[\left(S_i^z\right)^2\right]^{[\mathrm{ZM}]} &= \sum_{M=-NS}^{NS} \langle NS, M| \sum_i \left(S_i^z\right)^2 |NS, M\rangle |NS, M\rangle\langle NS, M\rangle \\ &= c + \alpha \left(K^z\right)^2 + \ldots\end{aligned} \tag{4.35}$$

With this, we can define the rotor ground-state energy:

$$\begin{aligned}E_{R,0} &= E_{CSS}(B_q = 0) + c\left(B_q - \frac{3\tilde{V}_0}{4(N-1)}\right) \\ &= -\frac{\tilde{V}_0 N S^2}{4} + c\left(B_q - \frac{3\tilde{V}_0}{4(N-1)}\right)\end{aligned} \tag{4.36}$$

and the corrected moment of inertia:

$$\chi_0' = \frac{1}{2I'} = \frac{1}{2\tilde{I}} + \left(B_q - -\frac{3\tilde{V}_0}{4(N-1)}\right)\alpha \tag{4.37}$$

$$= \frac{3\tilde{V}_0}{4(N-1)}(1-\alpha) + \alpha B_q. \tag{4.38}$$

In this subsection, we will use this corrected energy $E_{R,0}$ and inverse moment of inertia χ_0' for the comparison of the spectrum with ED for small system sizes and for the dynamics of small systems (up to $N = 4$). However, to investigate the dynamics of larger systems, it will not be possible for us to reconstruct numerically the operator $\left[(S_i^z)^2\right]^{[\mathrm{ZM}]}$, and we will instead follow the RSW approach in its simpler formulation (see section 4.2.1).

We show in figure 4.8 the energy of the different eigenstates versus their mean value of $(J^z)^2$, both for the full ED spectrum and the RSW spectrum for the rotor and the first spin waves, in the uniform case and for a 2×2 square lattice with $S = 3$. In the case of a 2×2 plaquette, we expect only two different LSW energies, at wavevectors $\vec{q}_1 = (0, \pi)$ and $\vec{q}_2 = (\pi, \pi)$. We can construct the first excited states as $(n_{\vec{q}_1} = 1, n_{\vec{q}_2} = 0)$ or $(n_{\vec{q}_1} = 0, n_{\vec{q}_2} = 1)$ for one boson (red crosses in figure 4.8), and $(n_{\vec{q}_1} = 2, n_{\vec{q}_2} = 0)$, $(n_{\vec{q}_1} = 0, n_{\vec{q}_2} = 2)$ or $(n_{\vec{q}_1} = 1, n_{\vec{q}_2} = 1)$ for two bosons (orange crosses).

As we can see, for small B_q ($B_q = J$), RSW theory reproduces correctly the low-energy spectrum of the Hamiltonian and this occurs without any free parameter. We can also see that the exact Hamiltonian has a clear tower-of-state structure, reminiscent of the OAT model. On the other hand, for a larger B_q value ($B_q = 15J$), the agreement is much poorer, signalling that the assumption of rotor/spin-wave separation is no longer justified, most likely because the density of $b_{\vec{q}\neq 0}$ bosons becomes larger the larger B_q.

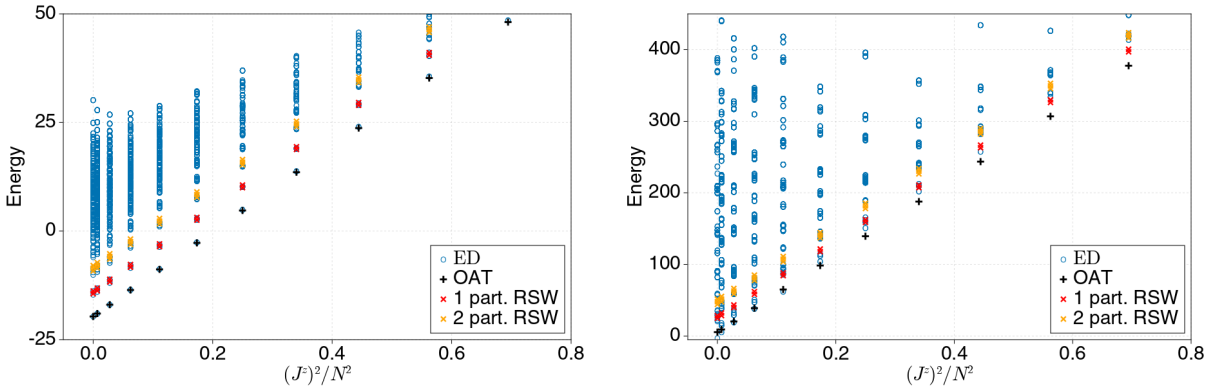

(a) $B_q = J$ (b) $B_q = 15J$

Figure 4.8: Comparison between the spectrum of the exact Hamiltonian (blue circle) and RSW model for the rotor (black crosses), with 1 bosonic excitation (red crosses) and 2 bosonic excitations (orange crosses).

Time evolution of observables. The second step in our benchmarking procedure is to look at the time evolution, starting with a coherent spin state, and compare the results of RSW theory and exact diagonalization for small systems in 1D and 2D.

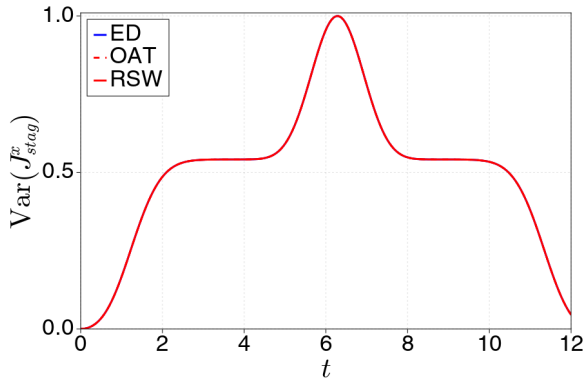

(a) $B_q = 0.25J$

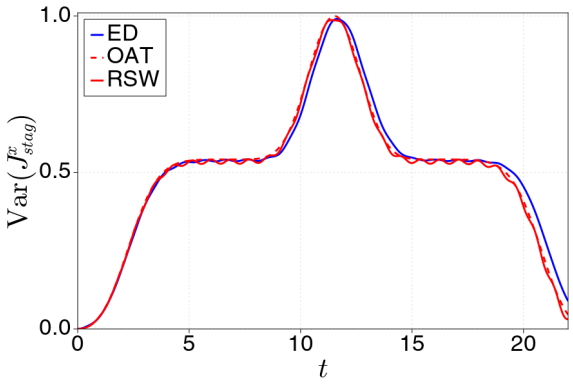

(b) $B_q = 0$

Figure 4.9: Comparison between the time evolution of $\mathrm{Var}\left(J^x_{stag}\right)$ computed with ED (blue) and with the RSW model with only the rotor (red dashed lines) and the rotor and the spin waves (red solid lines) for a 1D system of $N = 2$ spins $S = 3$ and a staggered initial state.

We start by looking at the case of 1D systems with just $N = 2$ sites, with a staggered initial state, as we expect a perfect OAT dynamics for $B_q = 0.25J$. This is indeed what we see when plotting $\mathrm{Var}\left(J^x_{stag}\right)$ in figure 4.9a, as we can see that the RSW results perfectly matches the ED ones, and they correspond exactly to the rotor part - meaning that there are no spin waves. Indeed, we find for this very specific value of B_q that for the only finite momentum $q = \pi$, we have $\mathcal{B}_\pi = 0$. We then vary the value of B_q to see how the RSW prediction evolves when introducing spin waves. We can see in figure 4.9b that the spin waves introduce deviations from a perfect OAT dynamics, in the form of oscillations of small amplitudes that can also be observed with ED. Even though the amplitude of the oscillation is not perfectly reproduced, we can already see that they have the correct frequency. Finally, it is worth mentioning that we get with a decent agreement the time at which the variance of J^x_{stag} reaches its maximum, without any free parameter. In particular, our approach predicts successfully the fact that the time needed to reach the maximum of $\mathrm{Var}\left(J^x_{stag}\right)$ nearly doubles when changing the value of B_q from $B_q = 0.25J$ to $B_q = 0$.

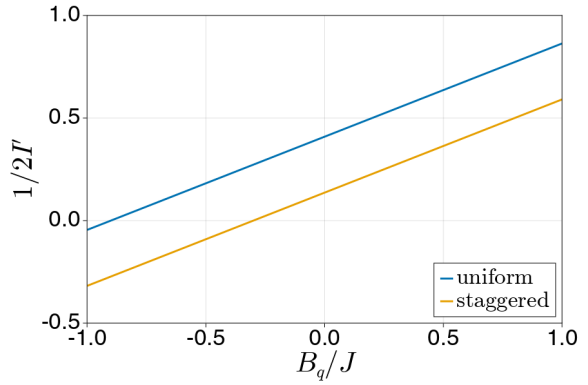

(a) $N = 2$

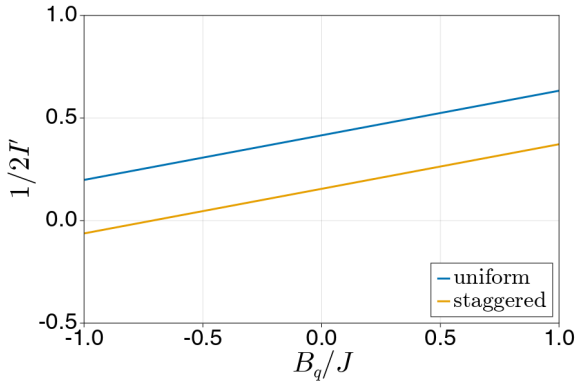

(b) $N = 4$

Figure 4.10: Corrected inverse moment of inertia $1/2I'$ for various values of B_q, for the uniform and staggered Hamiltonian for 1D system with (a) $N = 2$ and (b) $N = 4$ spins of length $S = 3$.

Using the corrected inverse moment of inertia $1/2I'$, we try to determine the value of B_q at which it vanishes - corresponding to a divergence of t_{max} as seen in the previous chapter. We plot in figure 4.10 the value of $1/2I'$ for the uniform and staggered Hamiltonian for various values of B_q. As we can see, the linear dependence of $1/2I'$ with B_q explains the divergence of t_{max} as $1/|B_q - B_q^c|$ in the staggered case. Also, we can see that the predicted value of $B_q^c \approx -0.3$ for $N = 2$ and $B_q^c \approx -0.7$ is in decent agreement with the value predicted by exact diagonalization (see figure 3.3 and 3.12b in the previous chapter). Moreover, in the uniform case, the value of B_q at which we expect $1/2I'$ to vanish is negative - corresponding to a value of B_q for which we expect a z Néel phase in the ground state - and we do not expect the separation of variables to hold. This explains why we do not see any divergence of t_{max} in the uniform case.

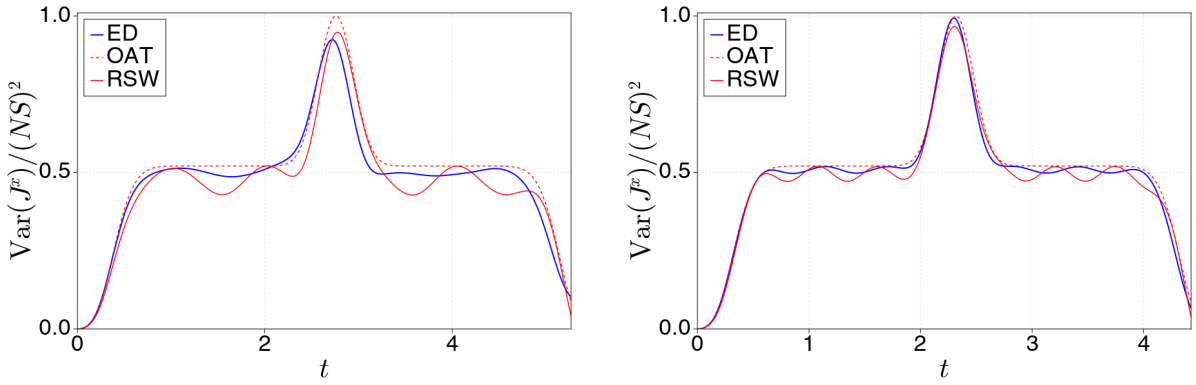

(a) $B_q = 0.5J$ (b) $B_q = J$

Figure 4.11: Comparison between the time evolution of Var (J^x) computed with ED (blue) and with the RSW model with only the rotor (red dashed lines) and the rotor and the spin waves (red solid lines) for a 2D system of $N = 2 \times 2$ spins $S = 3$ and a uniform initial state.

We also looked at the case of 2D systems, with a uniform initial state to further test our ansatz. Results are shown in figure 4.11, and we draw the same conclusions as before. In particular, we seem to have a very good agreement at short times between ED and RSW results. We further investigate the short-time dynamics by computing the time evolution of $\langle J^x \rangle$ and the squeezing parameter in the 2D case, starting with a uniform CSS along x. We show in figures 4.12 and 4.13 the short-time evolution of these observables. As we can see, the RSW approach reproduces to a good extent the dynamics predicted by ED. Moreover in the time evolution of the squeezing parameter we can clearly see that the contribution of the SW corrects the prediction of the rotor-only model to give a better agreement with the exact data. Adding the two contributions together within the RSW approach, we recover almost exactly the optimal squeezing value predicted by ED, at least at short times.

From this we can conclude that the rotor/spin-wave separation is indeed justified when the density of bosons at finite momentum remains small (as predicted from the theory). Therefore the next step would be to look at the predictions of our RSW approach for the number of bosons N_{bos} for increasing system sizes and various values of B_q, so as to test in which regimes RSW approach can be used reliably to study the dynamics of sizeable spin ensembles.

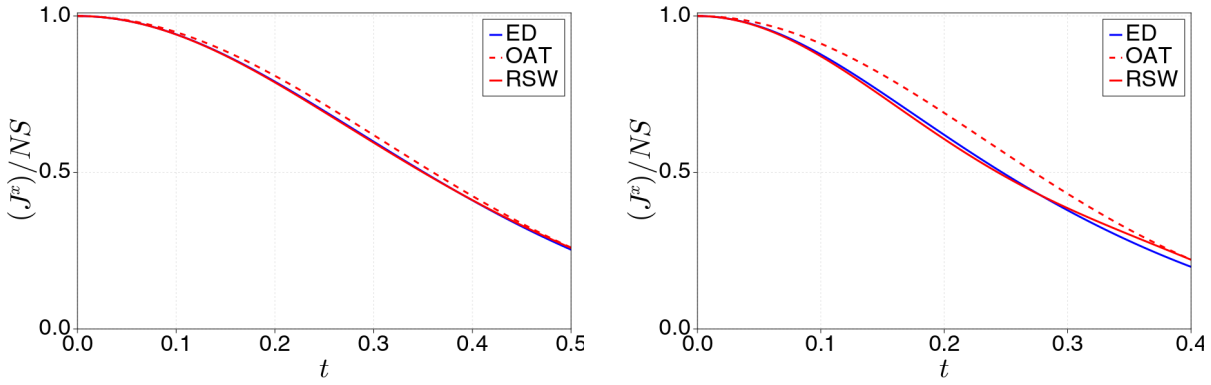

(a) $B_q = J$ (b) $B_q = 2J$

Figure 4.12: Comparison between the time evolution of $\langle (J^x) \rangle / NS$ computed with ED (blue) and with the RSW model with only the rotor (red dashed lines) and the rotor and the spin waves (red solid lines) for a 2D system of $N = 2 \times 2$ spins $S = 3$ and a uniform initial state.

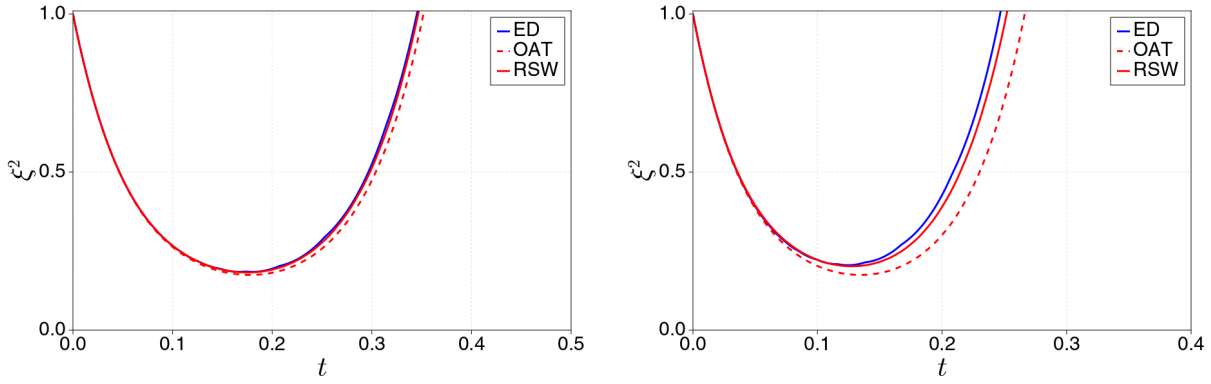

(a) $B_q = J$ (b) $B_q = 2J$

Figure 4.13: Comparison between the time evolution of the squeezing parameter ξ^2 computed with ED (blue) and with the RSW model with only the rotor (red dashed lines) and the rotor and the spin waves (red solid lines) for a 2D system of $N = 2 \times 2$ spins $S = 3$ and a uniform initial state.

4.2.3 Population dynamics of the finite-momentum bosons

We first look at the prediction of our approach for the time evolution of

$$N_{bos} = \sum_{\vec{q} \neq 0} \langle b^\dagger_{\vec{q}} b_{\vec{q}} \rangle = \sum_{\vec{q} \neq 0} G_{\vec{q}}, \tag{4.39}$$

starting with a CSS along x, for both the uniform and staggered Hamiltonians, and for 1D and 2D systems. Thanks to the Bogolyubov transformation, we have an explicit formula for the time evolution of $G_{\vec{q}}$:

$$G_{\vec{q}}(t) = 2u^2_{\vec{q}} v^2_{\vec{q}} (1 - \cos(2E_{\vec{q}} t)) \tag{4.40}$$

with the same definition of $u_{\vec{q}}, v_{\vec{q}}$ and $E_{\vec{q}}$ as in equation 4.12. In the case where we have at least a wavevector $\vec{q}$ such that $E^2_{\vec{q}} < 0$, this will lead to an exponentially growing number of bosons in the system and we will be rapidly out of the domain of validity of our approach. As we saw

in the previous section when using the LSW approach, this occurs when our initial state is not a low-energy state, due e.g. to the fact that we have crossed a phase transition in the ground state of the Hamiltonian. In particular, as we will discuss further below, the proliferation of finite-momentum bosons is at odds with OAT-like dynamics and scalable spin squeezing. On the other hand, if all the $E_{\vec{q}}$ are real, then we are left with a periodic oscillation of all the $G\vec{q}$'s, therefore N_{bos} will be bounded and will oscillate in time. In order to know whether we are in the domain of validity of the RSW approach or not, we can focus on the maximum value of N_{bos} in time, that we call $N_{bos}^{\max}$, and compare it to $2NS$. As long as we have $N_{bos}^{\max}/(2NS)$ small compared to 1, we can expect a dynamics that remains close to the one of a OAT model. We shall discuss more in details in subsection 4.3 the validity and limits of this prediction.

1D systems. We first investigate the case of a 1D dipolar XXZ chain, with both the uniform and staggered Hamiltonian, with an initial state which is a uniform CSS along x. We show in figure 4.14 the results for $N_{bos}^{\max}$ versus the system size N and for various values of B_q. It clearly appears that in the case of a uniform initial state, the OAT-like dynamics observed in chapter 3 for small systems cannot persist indefinitely when going to larger ones. Indeed, the number of bosons generated by the dynamics keeps increasing when N increases, which indicates that for larger systems there will be no features left of the OAT dynamics. For negative values of B_q we find instead an exponentially growing number N_{bos} as soon as $B_q = 0$. On the other hand, for a staggered initial state, there seems to be a small range of values of B_q for which $N_{bos}^{\max}$ does not increase for increasing N. This effect would require some fine tuning of the quadratic Zeeman field B_q: $(\delta B_q < 0.2J)$, but it seems promising for the persistence of OAT-like dynamics.

The data shown in figure 4.14 were calculated for $S = 3$. However since $E_{\vec{q}}$, $\mathcal{A}_{\vec{q}}$ and $\mathcal{B}_{\vec{q}}$ are all proportional to S, changing the value of S will only affect the speed at which the bosons appear in the system, but not their total number. Therefore the ratio $N_{bos}^{\max}/(2SN)$ will go down as $1/S$ and we expect systems with large S to have a more pronounced OAT-like behaviour the size N being the same.

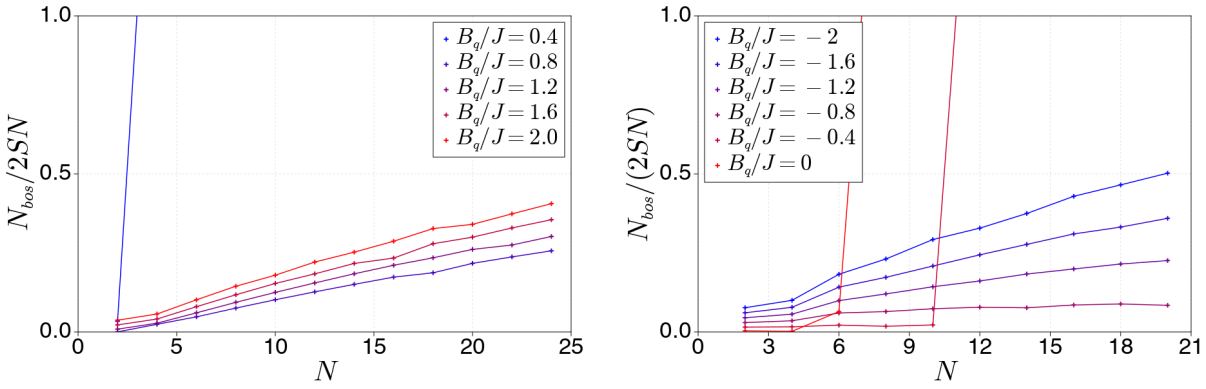

(a) Uniform initial state.

(b) Staggered initial state.

Figure 4.14: Evolution of $N_{bos}^{\max}$ versus the 1D system size N, for various values of B_q and for $S = 3$.

These results are consistent with the results obtained with the LSW approach in 1D in section 4.1.2, as we do have only a small number of bosons for small positive values of B_q in the staggered case and small negative values of B_q in the uniform case.

2D systems. For 2D systems, with the uniform initial state, we get very promising results, as shown in figure 4.15. The ratio $N_{bos}^{\max}/(2NS)$ converges to a finite value for increasing system size. We can then have a look at the evolution of this limit value for different values of B_q (see figure 4.16). This reveals a large range of values of B_q for which we expect a OAT-like behaviour even for large system sizes, namely a dynamics leading to scalable spin squeezing.

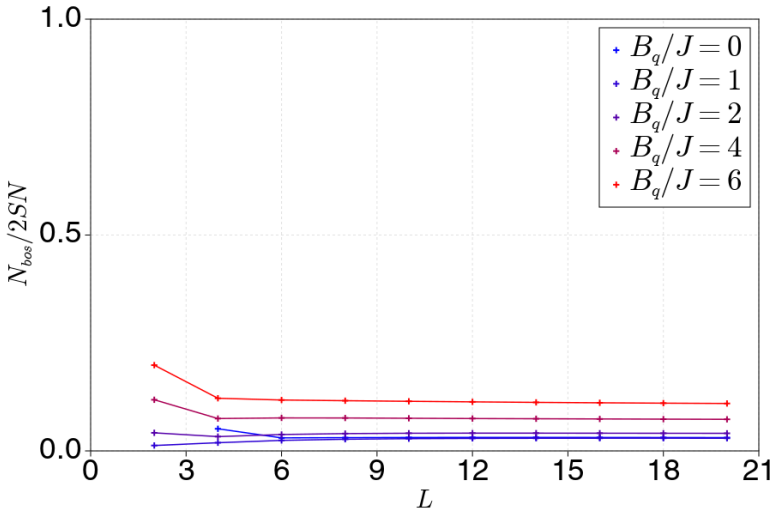

Figure 4.15: Evolution of $N_{bos}^{\max}$ versus the linear system size L ($N = L \times L$), for various values of B_q and for $S = 3$.

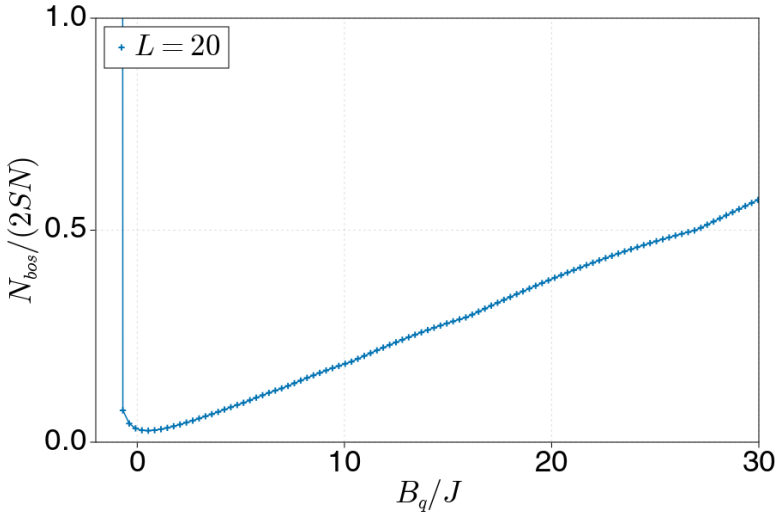

(a) $S = 3$

Figure 4.16: Evolution of $N_{bos}^{\max}$ versus B_q/J for a linear system size $L = 20$ ($N = L \times L$) for $S = 3$.

On the other hand the staggered initial state becomes unstable for $L > 2$ and for positive values of B_q since we get very flat modes, with high values of $u_{\vec{q}}^2 v_{\vec{q}}^2 \gtrsim 2$, which leads to a very high boson number even at short times. For negative values of B_q, it is even worse as the SW is ill-defined, since there exist a wavevector $\vec{q}$ for which we have a negative $E_{\vec{q}}$.

3D systems. So far we have not discussed the case of 3D systems. The fundamental reason is that in 3D we have to take into account the anisotropy of dipolar interactions:

$$V_{ij} = \frac{1 - 3\cos^2(\theta_{ij})}{|\vec{r}_i - \vec{r}_j|^3} \tag{4.41}$$

with θ_{ij} the angle between the dipole-dipole axis $\vec{r}_i - \vec{r}_j$ and the magnetic field $\vec{B}$. Due to this anisotropy, the 3D average of V_{ij} (i.e $\tilde{V}(0)$) in space vanishes, which leads to a vanishing OAT term in the separation-of-variable scheme. This corresponds to having an infinite moment of inertia I for our centre of mass, thus preventing the collective dynamics of the spins. Therefore we do not expect any scalable spin squeezing on a 3D cubic lattice. The best case scenario would be the limit of well separated (and thus weakly coupled) 2D planes along the z direction, for which we may expect the same scaling as for a single 2D plane. This is why we will focus only on the 2D case for the rest of this chapter.

4.3 Scalable spin squeezing in 2D lattices

In the previous section we have identified the case of 2D lattices initialised in the uniform CSS as a very promising candidate for the realization of OAT-like dynamics and hence scalable squeezing. Since the comparison with ED will not be possible anymore for large system sizes, we need to introduce a second numerical method to benchmark the prediction of RSW theory. We choose the approach of the truncated cumulant expansion (TCE) for quantum spin fluctuations. As we will see, this second method is based on assumptions completely independent from the RSW approach. This suggests that, if both methods agree, then their predictions are both quantitatively correct.

4.3.1 Truncated Cumulant Expansion (TCE)

We first introduce a local basis of operators:

$$T_i^{m,m'} = |i,m\rangle\langle i,m'| \tag{4.42}$$

where $|i,m\rangle$ is the eigenstate of S_i^z with eigenvalue m. Any local observable can then be expressed using this basis:

$$O_i = \sum_{m,m'} \langle i,m|O_i|i,m'\rangle T_i^{m,m'}. \tag{4.43}$$

For instance, for the spin operators, we have:

$$S_i^z = \sum_m m T_i^{mm}, \quad S_i^+ = \sum_m \sqrt{S(S+1) - m(m+1)}\, T_i^{m+1,m}. \tag{4.44}$$

One can then reconstruct the time evolution of correlation functions of any observable using the correlation functions of the T operators:

$$\{\langle T_i^{m,m'}\rangle\}, \quad \{\langle T_i^{m,m'} T_j^{n,n'}\rangle\}, \quad \{\langle T_i^{m,m'} T_j^{n,n'} T_k^{p,p'}\rangle\}$$

and so on up to the N-th order (for a system with N spins). In practice, it is not possible to compute the time evolution of the correlations functions of the T operators at all orders. In

order to reduce the number of correlators to be evolved, a common strategy is to focus on the cumulants of the quantum fluctuations of the spin system.

The cumulants of the fluctuations of a set of correlated variables $\{O_i\}$ are defined in the following recursive way:

$$\begin{aligned}
\langle O_i\rangle_C &= \langle O_i\rangle \\
\langle O_iO_j\rangle_C &= \langle O_iO_j\rangle - \langle O_i\rangle\langle O_j\rangle \\
\langle O_iO_jO_k\rangle_C &= \langle O_iO_jO_k\rangle - \langle O_iO_j\rangle_C\langle O_k\rangle - \langle O_iO_k\rangle_C\langle O_j\rangle - \langle O_jO_k\rangle_C\langle O_i\rangle - \langle O_i\rangle\langle O_j\rangle\langle O_k\rangle \\
&= \langle O_iO_jO_k\rangle - \langle O_iO_j\rangle\langle O_k\rangle - \langle O_iO_k\rangle\langle O_j\rangle - \langle O_jO_k\rangle\langle O_i\rangle + 2\langle O_i\rangle\langle O_j\rangle\langle O_k\rangle \\
&(\dots)
\end{aligned}$$

The strategy one can follow is to assume that the cumulants are structured in a hierarchy, such that higher-order cumulants are smaller than lower-order ones, as it is the case in many relevant physical examples (e.g. for bosonic or fermionic gases in states close to Gaussian states). If such a hierarchy exists, it can be conveniently truncated at some finite order, assuming that all n-th order cumulants for $n > n_0$ vanish – this defines then a n_0-th order TCE. In the case $n_0 = 1$, the TCE approach is equivalent to a single-site mean-field approximation. Since our goal is to describe the dynamics of quantum correlations, we adopt instead a second-order TCE, assuming the vanishing of all cumulants starting from 3rd order. Under this assumption, the evolution of the state can be fully described by knowing the evolution of the expectation values $\{\langle T_i^{m,m'}\rangle\}$ and $\{\langle T_i^{m,m'}T_j^{n,n'}\rangle\}$ namely a number of objects $\sim O((2S+1)^4N)$ for a system invariant under spatial translation. From the previous formula it is clear that the computational cost increases with the fourth power of the spin length S, so that the system sizes accessible in practice to this approach decrease with S.

Considering the expectation values $\langle O\rangle \in \{\langle T_i^{m,m'}\rangle, \langle T_i^{m,m'}T_j^{n,n'}\rangle\}$, their evolution is dictated by the Heisenberg equation:

$$i\frac{\mathrm{d}\langle O\rangle}{\mathrm{d}t} = \langle[O,\mathcal{H}]\rangle. \tag{4.45}$$

The truncation of the cumulant hierarchy allows then to write the expectation value of the commutator on the right-hand side as a function of the first-order and second-order cumulants for the T operators, namely $\langle[O,\mathcal{H}]\rangle = F_O\left(\{\langle T_i^{m,m'}\rangle, \langle T_i^{m,m'}T_j^{n,n'}\rangle\}\right)$, so that the equations of motion take the form of a closed set of non-linear differential equations.

Writing the equations of motion of the first- and second-order correlation functions leads to very lengthy expressions, therefore we shall report them in Appendix A. We solve the coupled $\sim O((2S+1)^4N)$ nonlinear equations of motion via a standard 4-th order Runge-Kutta scheme. In particular the expectation value of the Hamiltonian can be written as a linear combination of first- and second-order correlation functions (as it is quadratic in terms of spin operators), so that the energy is conserved within machine precision by this approach. Notice moreover that the TCE approach involves only an approximation at the level of the inter-site correlations, but no approximation is made instead on the statistics of fluctuations of single sites, whose physics is therefore described exactly – in fact even the two-site physics is exactly described with a second-order TCE.

In spite of its ability to correctly describe single-site and two-site physics, the TCE approach has the fundamental shortcoming that no physical quantum state of the spin ensemble may in fact verify the hypothesis of vanishing cumulants beyond a given order $n_0 \geq 2$. Indeed, while Gaussian states (with exactly vanishing third- and higher-order cumulants) exist for

ensembles of bosonic and fermionic modes, no such states are known for spin ensembles. As a consequence the TCE approach can produce unphysical results, especially so when correlations become strongly nonlocal. In the quench dynamics we will study, the initial state has vanishing cumulants beyond first order (since it is a separable state), so that it is exactly described by 2nd-order TCE, as well as its short-time evolution.

Yet when the dynamics of the 2D array of dipolar spins leads to the appearance of very strong squeezing – specifically, when it is akin to that of the OAT model – we observe that the Heisenberg inequality for the collective spin $\mathrm{Var}\,(J^{\min})\,\mathrm{Var}\,(J^{\max}) \geq \langle J^x\rangle^2/4$ can be violated by our TCE results, where $J^{\max}$ is the anti-squeezed collective-spin component, perpendicular to $J^{\min}$ in the yz plane. This violation is the precursor to a drastic decrease of $\mathrm{Var}\,(J^{\min})$, which can become negative – underlying the fact that the second-order TCE approach has the tendency to strongly overestimate the anti-correlations associated with squeezing. In this situation we monitor the evolution of the ratio $R = 4\mathrm{Var}\,(J^{\min})\,\mathrm{Var}\,(J^{\max})\,/\langle J^x\rangle^2$, and we stop the time evolution when $R(t)$ reaches a maximum, which is the prelude to the rapid fall to values below unity and even negative. This is the reason why the TCE results we will show in the different figures are restricted to short times, not reaching the optimal squeezing time t_{OAT}.

4.3.2 Time evolution of the squeezing parameter

We now have all the ingredients we need to compute the time evolution of the spin-squeezing parameter for 2D systems of spins, initialised in a uniform array of CSS along x. We first look at small values of B_q, well within the validity region of our RSW ansatz, for various values of S - namely $S = 3$ (relevant for Chromium), $S = 6$ (relevant for bosonic Erbium) and $S = 8$ (relevant for Dysprosium). In each case, we compare RSW results with those coming from the TCE method. We show our results in figure 4.17. Each colour corresponds to a different system size, the solid lines for the RSW method and the dots for the TCE method. We also show in dotted lines the results only for the rotor part of the RSW ansatz, and in dashed lines the results of the single spin dynamics - namely the quadratic Zeeman term, which acts as a local OAT Hamiltonian. Finally, the dashed-dotted line delimits the area below which we can certify that the system is entangled, according to the criterion of Eq. 2.15.

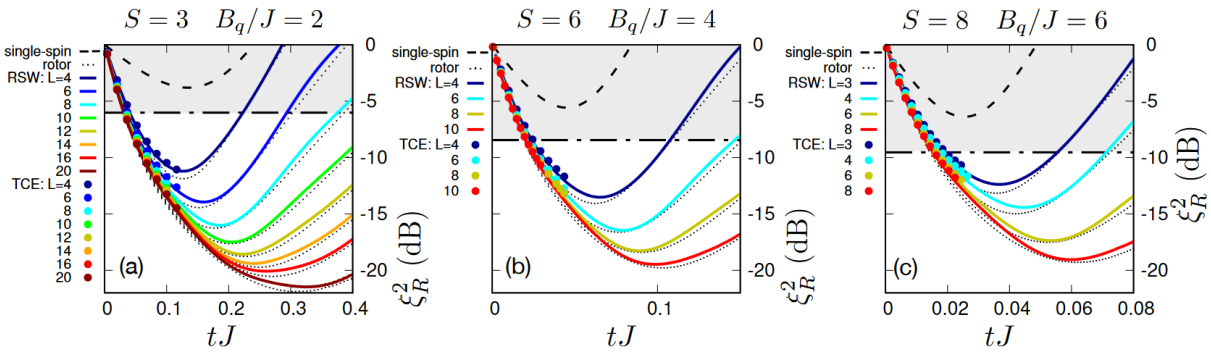

Figure 4.17: Evolution of the squeezing parameter (in dB) versus time for different systems sizes L ($N = L \times L$), for $S = 3, B_q = 2J$ (left), $S = 6, B_q = 4J$ (centre) and $S = 8, B_q = 6J$ (right).

As we can see in figure 4.17, in the three cases we have a very good agreement between the

two numerical methods over the time intervals for which the TCE approach delivers physical results. Moreover, the time evolution of the spin-squeezing parameter follows almost perfectly the one predicted by a perfect OAT model (dotted lines), which indicates that we indeed have a system that is governed by the collective spin dynamics. We therefore have scalable squeezing in the system, as we can see from the fact that we get more and more squeezing the larger the system size is (note that the vertical axis is in log scale). One can also notice that in each case, the squeezing minimum is well below the threshold for entanglement detection, even for small systems sizes $L = 4$. All these observations were expected, since the range of validity of the RSW ansatz coincides with the range of values of B_q for which we expect a OAT-like dynamics. Even more interestingly, we can have a look at what happens when we take B_q out of this region of validity, increasing progressively the value of B_q.

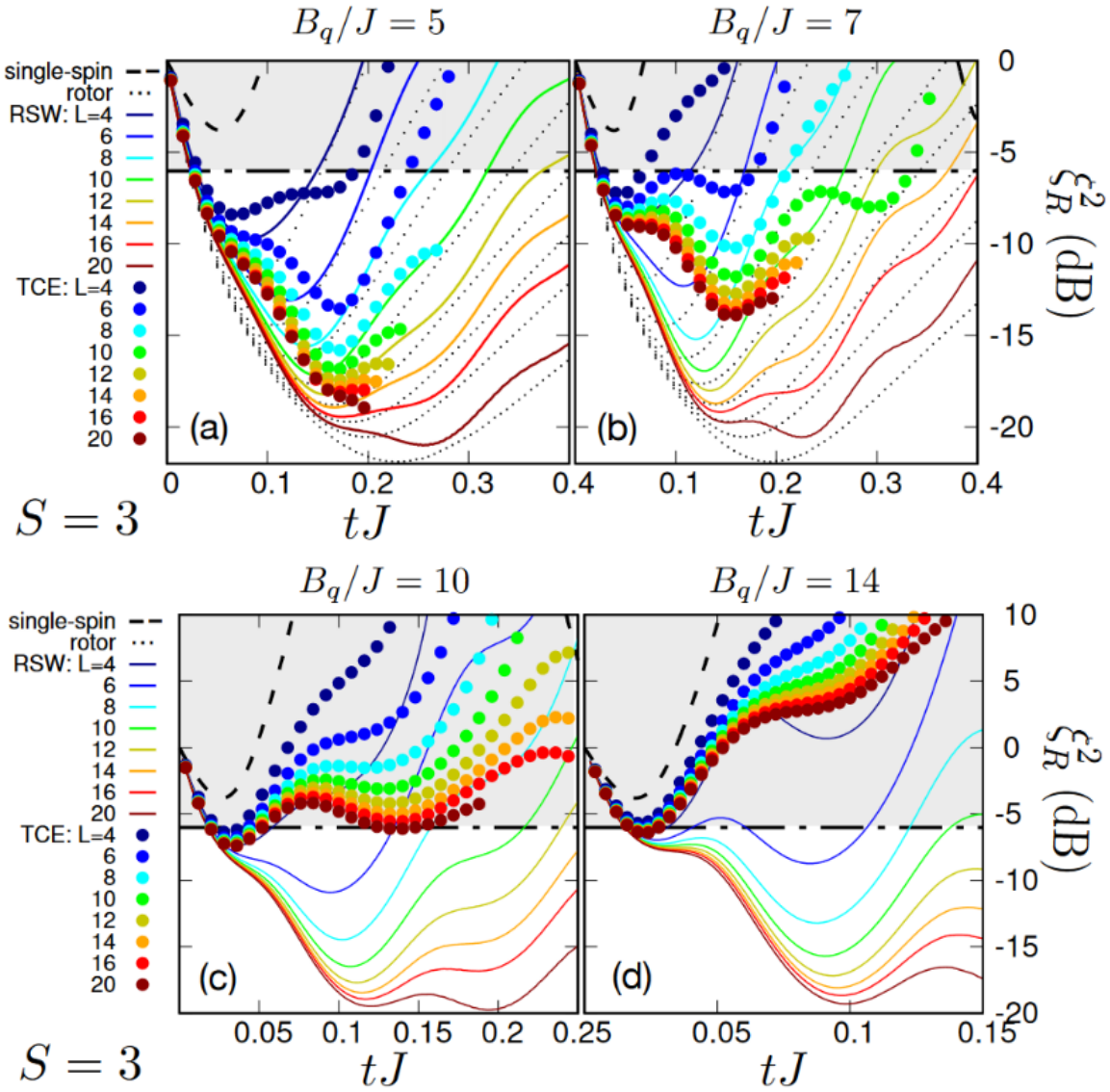

Figure 4.18: Evolution of the squeezing parameter (in dB) versus time for different systems sizes L ($N = L \times L$), for $S = 3$, $B_q = 5J$ (a), $B_q = 7J$ (b), $B_q = 10J$ (c) and $B_q = 14J$ (d). We use the same legend convention as figure 4.17.

As we can see on panel (a) and (b) in figure 4.18, for intermediate values of B_q, we start to see significant discrepancies between the RSW and the TCE results. This signals that the picture of separation of variables underlying RSW theory breaks down. This interpretation is consistent with the fact that the spin-wave correction to the rotor dynamics becomes sizeable, due to a significant density of finite-momentum bosons produced by the dynamics. Nonetheless, as we shall also discuss in the next section, the squeezing parameter predicted by the TCE approach appears to remain scalable for a large range of B_q values, albeit following a behaviour which can no longer be understood when starting from the OAT paradigm, as shown in panels (c) and (d). On these panels, the competition between single-spin and many-body physics becomes manifest, with a short-time behaviour dominated by the B_q term, in which ξ_R^2 reaches a nearly size-independent first minimum, followed by antisqueezing dynamics (ξ_R^2 increases). This first phase of the evolution is followed by a second phase in which, at least for the largest system sizes we considered, anti-squeezing stops, and ξ_R^2 begins to decrease again developing a second minimum, the deeper the larger the size. This later dynamics is clearly the result of many-body interactions – as revealed by its scaling nature with the system size. This can be understood in relationship with a fundamental feature of dipolar spins in 2D, namely their ability to develop and maintain long-range order at low energy [101] (panel (c) of figure 4.18), which is not possible for system with short-range interaction due to the Hohenberg-Mermin-Wagner theorem [102, 103]. Note that for the large values of B_q, since we recover a dynamics that is similar to the one of single spin dynamics, we expect TCE to give more accurate results than the RSW method. Finally, as we can see on panel (d), a significant shift in the squeezing dynamics has occurred when reaching $B_q = 14J$, at least according to TCE, since we do not observe scalable squeezing anymore.

4.3.3 Scaling of the squeezing parameter

From the time evolution data, we can then extract the scaling of the squeezing parameter versus system size for different values of B_q. As mentioned before, we cannot always reach the optimal squeezing time t_{OAT} with the TCE approach. We can nonetheless investigate the scaling of the squeezing parameter at different fractions of the optimal time αt_{OAT}, $\alpha \in [0, 1]$. For each time, when can extract a scaling exponent ν and compare it to the optimal one $\nu_{opt} = 2/3$.

We show our results in the case $S = 3, B_q = 1$ in figure 4.19, based on exact results from a pure OAT Hamiltonian (solid lines) and our RSW approach (diamonds). As we can see, for $B_q = 1$, we obtain the same scaling for the OAT Hamiltonian and the RSW approach. Moreover, in figure 4.19b, we can clearly see that the scaling of the squeezing parameter with system size is almost equal to its optimal value even for a small fraction of the optimal time ($\alpha \sim 0.3 - 0.5$). Therefore we will perform the analysis of TCE results at $t = 0.3t_{OAT}$, for which we already expect an important scaling of the squeezing parameter with system size when the dynamics of the system is akin to the OAT dynamics. We show our results on the scaling of squeezing at $t = 0.3t_{OAT}$ in figure 4.20 for $S = 3, 6$ and 8. As we can see, we have a broad transition from a squeezing parameter that scales with system size for low positive B_q, to an absence of scaling (or inverse scaling) for larger values of B_q. We can see that the two numerical methods (RSW and TCE) disagree on the value of B_q for the transition between the two scaling regimes, as the RSW approach tends to overestimate by construction the proximity to an exact OAT model and hence overestimate the value of the critical B_q. Both methods predict that this transition between the scaling regimes occurs for values of B_q that seems to

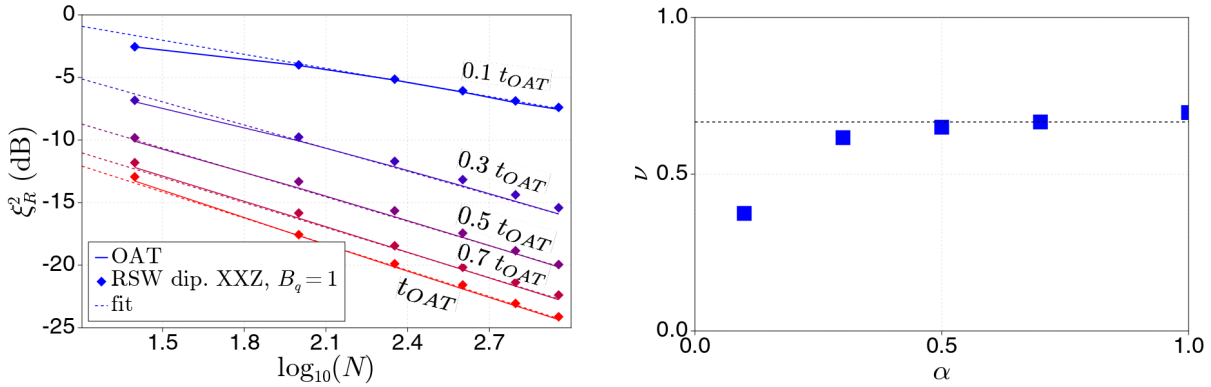

(a) (b)

Figure 4.19: (a) Evolution of the squeezing parameter (in dB) versus log$N$ for different fractions α of the optimal time t_{OAT} for $S = 3, B_q = J$. (b) Evolution of the scaling exponent with the fraction α.

scale linearly with the spin length S, even though there is no sharp transition.

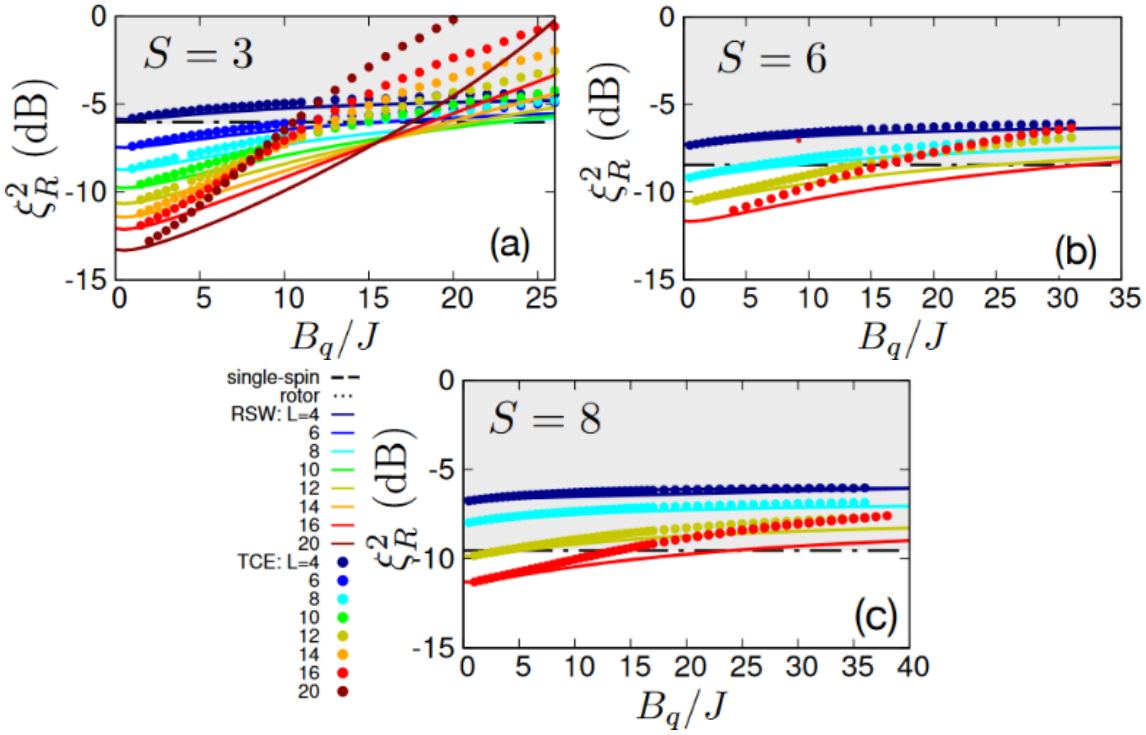

Figure 4.20: Evolution of the squeezing parameter (in dB) versus B_q/J for different systems sizes L ($N = L \times L$), for $S = 3$ (a), $S = 6$ (b) and $S = 8$ (c). Solid lines stand for the RSW method, while the dots correspond to TCE results.

4.4 Study of the thermodynamic transition

In a recent study [104], the authors proposed the conjecture that thermalization of long-range xy ferromagnetic order is a sufficient condition for the occurrence of scalable spin-squeezing. In order to test this conjecture, we will further study the properties of the system around the thermodynamic transitions we already introduced at the beginning of the chapter.

The previous study of the dynamics revealed two transitions which we can try to relate to the thermodynamic behaviour. On the one hand, for B_q becoming slightly negative, we have a fast breakdown of the RSW separation, as the number of bosons explodes in a finite time (see figure 4.16). Such a phenomenon is due to the fact that we find imaginary energies with the Bogolyubov transformation, leading to an exponential growth of N_{bos}. This means that our initial state becomes a highly excited state when $B_q < 0$, due to a drastic change in the ground state properties of the system. On the other hand, for increasing positive B_q, the number of bosons keep increasing linearly, until we reach a regime where we have no scalable squeezing. This indicates a second transition, of seemingly different nature from the first one. In this section, we shall investigate the nature of these two transitions. First, we will study in more details the thermodynamic phase diagram of our spin system, and then we will have a closer look at the time evolution of the system for increasing values of B_q, around the thermodynamics transition predicted in the phase diagram.

4.4.1 Phase diagram

We first reconstruct the phase diagram of the system, by checking the existence of long-range order for different values of B_q and different temperatures T.

Phase diagram for $S = 3$. Using numerically exact Quantum Monte Carlo (QMC) simulations, implemented by T. Roscilde, we compute the critical temperature for the existence of a long-range ferromagnetic order in the xy plane. We also use mean-field theory to compute the same critical temperature and the critical temperature for long-range Néel antiferromagnetism along the z axis, as we did in the first section of this chapter. Details of the numerical computations for both methods are given in the Appendix B.

From the QMC results shown in figure 4.21a, we can see that the thermodynamics exhibits long-range ferromagnetism in the xy plane for a wide range of values of B_q, $0 < B_q < 54J$, and up to a critical temperature T_c^{FM} which reaches a peak value of $\approx 20J$. The FM phase predicted by MF theory is in relatively good agreement with the one obtained via QMC, even though the nature of the transition is not correct (we have a mean-field transition from MF theory, see the appendix for more details). The quantitative agreement between the two methods is not surprising, given the fact that MF theory becomes exact in infinite dimensions; and that the long-range tail of dipolar interactions in 2D dominates the thermodynamics of the system, leading to the existence of a finite-temperature transition. MF theory also allows us to detect a second ordered phase, for $B_q < -1.1J$, as the system exhibits long-range Néel antiferromagnetism along the z axis. Finally, for large B_q, we expect - at the MF level - that the system is in a product state of single-spin Dicke states $|S = 3, m = 0\rangle$.

The connection between the dynamics of the system and its thermodynamics can be established via the mechanism of closed-system thermalization. Indeed, starting from a CSS along x, the unitary evolution driven by the dipolar Hamiltonian at long times is expected to thermalize

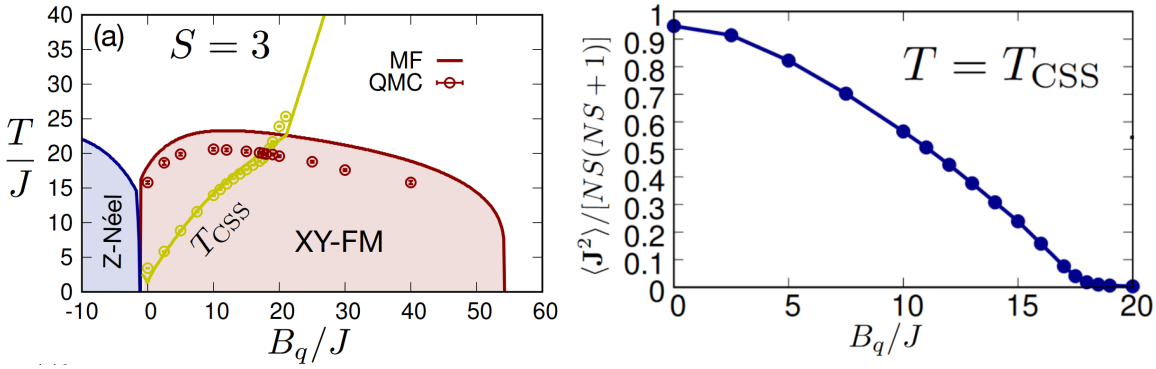

(a) Equilibrium phase diagram for $S = 3$.

(b) Expectation value of $\langle \vec{J}^2 \rangle$ at $T_{\mathrm{CSS}} \langle B_q \rangle$

Figure 4.21: Left : mean-field (MF) and quantum Monte Carlo (QMC) estimates of the transition temperature to xy-ferromagnetism (XY-FM), to Néel antiferromagnetism (Z-Néel), and of the coherent-state temperature T_{CSS}. Right: collective-spin square modulus $\langle \vec{J}^2 \rangle$ along the $(B_q\ ,\ T_{\mathrm{CSS}} \langle B_q \rangle)$ line, evaluated for a system of $N = 48 \times 48$ spins.

the state of the system [105], so that the time average of local observables reproduce their equilibrium expectation values at a temperature T_{CSS} such that

$$\langle \mathrm{CSS}_x | \mathcal{H} | \mathrm{CSS}_x \rangle = \langle \mathcal{H} \rangle_{T_{\mathrm{CSS}}} = \frac{\mathrm{Tr}\left(\mathcal{H} e^{-\mathcal{H}/T_{\mathrm{CSS}}} \right)}{\mathrm{Tr}\left(e^{-\mathcal{H}/T_{\mathrm{CSS}}} \right)}, \tag{4.46}$$

where $\langle ... \rangle_T$ denotes the thermodynamic average at temperature T. T_{CSS} is often referred to as the quench temperature. Figure 4.21a shows a very good agreement between the T_{CSS} computed with the QMC algorithm (open circles) and the one computed with the MF method (solid line).

The key question in order to know whether to expect long-range order or not after a unitary evolution of the system at long time is: does the quench temperature T_{CSS} lie below or above the critical temperature at a given B_q? Here, we can see that we have a clear transition at $B_{q,c} \approx 18J$, for which $T_{CSS}(B_{q,c}) = T_c^{\mathrm{FM}}(B_{q,c})$. This corresponds for our system to a transition from xy-ferromagnetic (XY-FM) to paramagnetic phase. Regarding the unitary evolution at long time, this translates in particular into a drop of the collective spin length $\langle \vec{J}^2 \rangle$ from macroscopic values ($\sim O(N^2)$) to microscopic values ($\sim O(N)$). We can clearly see this phenomenon in figure 4.21b, as $\langle \vec{J}^2 \rangle_{T_{\mathrm{CSS}}}$ drops drastically when B_q approaches $B_{q,c}$. Note that the scaling of the square modulus of the collective-spin with system size N is crucial for the scaling of the squeezing parameter (as having a scalable squeezing parameter requires keeping the spin polarized, i.e. having a spin length close to NS).

Dependence on S. Given the relatively good accuracy of MF theory in reconstructing the phase diagram for $S = 3$, it can be used also for the cases $S = 6$ and $S = 8$, which are much more demanding for unbiased QMC calculations. in figure 4.22 we compare the $S = 3$ phase diagram with those for $S = 6$ and $S = 8$. MF theory predicts a thermodynamic transition at the T_{CSS} temperature for $B_{q,c} \approx 21J$ for $S = 3$ (to be compared with $B_{q,c} \approx 18J$ from QMC); $B_{q,c} \approx 41J$ for $S = 6$, and $B_{q,c} \approx 54J$ for $S = 8$. As we can see, $B_{q,c}$ appears to grow linearly with S. MF theory also allows one to predict the critical B_q values delimiting the phase which exhibits xy ferromagnetism.

The transition to Néel antiferromagnetism is predicted by MF theory to occur for $B_{q,m} \approx -1.1J$ for $S = 3$, $B_{q,m} \approx -J$ for $S = 6$ and $B_{q,m} \approx -0.95J$ for $S = 8$. These predictions are to be compared with $B_{q,m} \approx -0.845J$ (for all spin values) from spin-wave theory. MF and spin-wave theory, albeit not predicting the same critical field, agree on its weak (or absent) spin-length dependence.

On the other hand, MF theory predicts a transition from xy ferromagnetism to quantum paramagnetism in the ground state for $B_q > B_{q,p}$ with $B_{q,p} \approx 54J$ for $S = 3$, $B_{q,p} \approx 190J$ for $S = 6$ and $B_{q,p} \approx 326J$ for $S = 8$. The $B_{q,p}$ values appear to grow with S approximately as S^2. As a consequence the range of B_q values for which one observes xy ferromagnetism at the quench temperature T_{CSS} appears to shrink with respect to the whole B_q extent of the xy ferromagnetic phase, due to the different scaling of $B_{q,c}$ and $B_{q,p}$ with S.

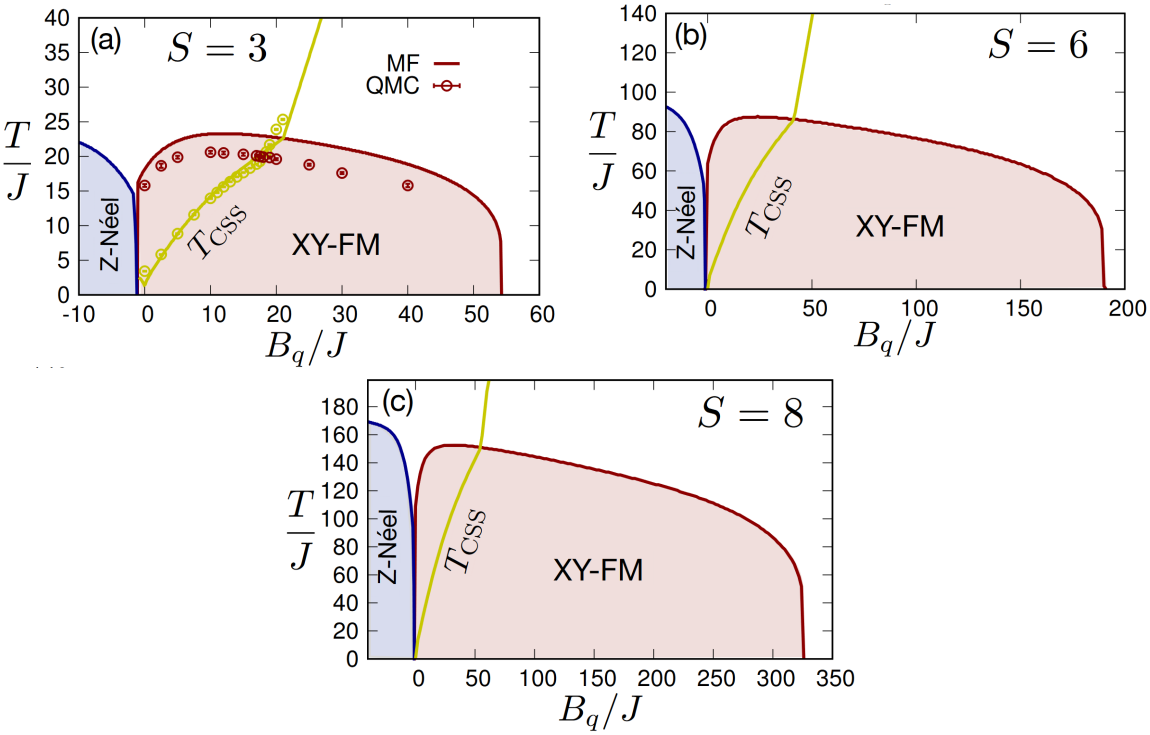

Figure 4.22: Phase diagrams for the $2D$ dipolar XXZ model with $S = 3(a), 6(b)$ and $8(c)$ from QMC and MF theory.

4.4.2 Time evolution around the thermodynamic transition

In the same fashion as in figure 4.18, we study the time evolution of the squeezing parameter for $S = 3$ for increasing values of B_q ranging from $10J$ to $24J$. We also investigate the time evolution of the average magnetization per spin ($\langle J^x \rangle / N$) and the minimal variance for the transverse-field components ($\mathrm{Var}\,(J^{\mathrm{min}})$) that contribute to the squeezing parameter. Our results (obtained with the TCE approach) are shown in figure 4.23. We remark that, for the values of B_q for which the long-time dynamics is expected to exhibit long-range ferromagnetism – namely for $B_q \leq B_{q,c} \approx 18J$ – the TCE data exhibit the characteristic finite-size dynamical precursor of spontaneous symmetry breaking which occurs in the thermodynamic limit. This can be seen in the first column of figure 4.24 from the persistence of a net magnetization

$\langle J^x \rangle / N > 0$ for longer times the larger the system size. This scaling persistence of magnetization can be seen at intermediate times, the early time dynamics being governed by nearly size-independent single spin physics. Indeed, we can see first a size-independent drop, which is very well described by the dynamics of single spins subject to the quadratic Zeeman field B_q (black line on the figures), followed by a tail that scales with system size.

In particular we estimate the extent of this tail from the time t_0 at which $\langle J^x \rangle$ crosses zero. The scaling of this time with system size for various values of B_q is shown in figure 4.24 (a). We observe that the scaling slows down quite markedly for $B_q \approx B_{q,c}$, reflecting the thermodynamic transition. This is a signature that, in spite of their approximate nature, the TCE results appear to be sensitive to the transition itself, whose position was obtained from unbiased QMC results.

We also observe in figure 4.23 that the dynamics of the minimal variance $\mathrm{Var}\,(J^{\min})$ maintains some significant scaling, not in its first minimum in time – which is clearly dictated by the single-spin dynamics – but rather in its second minimum, which comes from many-body interactions. The depth of the second minimum $\min_2 [\mathrm{Var}\,(J^{\min})]$ is shown in figure 4.24 (b). As we can see, it exhibits a persistent scaling even past the thermodynamic transition, nevertheless this scaling does not seem to follow a power law, and it is very different from the scaling which is exhibited by the OAT model (as $N^{-2/3}$ when considering the variance per spin). Hence one might wonder whether this scaling is actually persistent asymptotically; and whether it can lead to scalable squeezing when $\langle J^x \rangle / N$ remains finite – namely for $B_q < B_{q,c}$.

4.4.3 Discussion

All these results allow us to try and draw a link between the scalability of the squeezing at intermediate times and the presence (or absence) of long-range order at long times in the thermodynamic limit.

In all the cases where we have $T_{\mathrm{CSS}} < T_c^{\mathrm{FM}}$, we expect the establishment of long-range order in the long time dynamics of the system, which corresponds to a spontaneous symmetry breaking of the system. This spontaneous breaking of the $U(1)$ symmetry of the Hamiltonian in the thermodynamic limit can have important consequences for the squeezing dynamics [104]. In fact, it implies that, for finite system sizes, the initial polarization $\langle J^x \rangle$ associated with the CSS persists for increasingly long times the larger the system size (and never dies out in the thermodynamic limit). This is shown in figure 4.23, and was also observed experimentally in systems of dipolar qubits [106]. As a consequence, in spite of the depolarizing effect coming from the B_q term, ferromagnetism can protect the spin-squeezing parameter from blowing up, because it prevents a fast vanishing of the denominator in the squeezing parameter ξ_R^2 (see Eq. 2.11) which would lead to anti-squeezing otherwise. Moreover, long-range ferromagnetism can delay or even reverse the anti-squeezing dynamics. Finally, the collective spin remains of macroscopic length, as guaranteed by the fact that $\langle \vec{J}^2 \rangle \sim O(N^2)$ throughout the evolution – although it may differ significantly from its (initial) maximum value $NS(NS+1)$, as shown in figure 4.21b.

These observations led the authors of ref [104] to conjecture that thermalization of long-range xy ferromagnetic order is a sufficient condition for the occurrence of scalable spin-squeezing. Nonetheless, as we clearly observe in figure 4.18 (c) and (d) and 4.23, for the system sizes we explored (up to $N = 400$ for $S = 3$) the fast depolarization imposed by the B_q term can push the squeezing parameter to values ξ_R^2 which are systematically higher than the entanglement

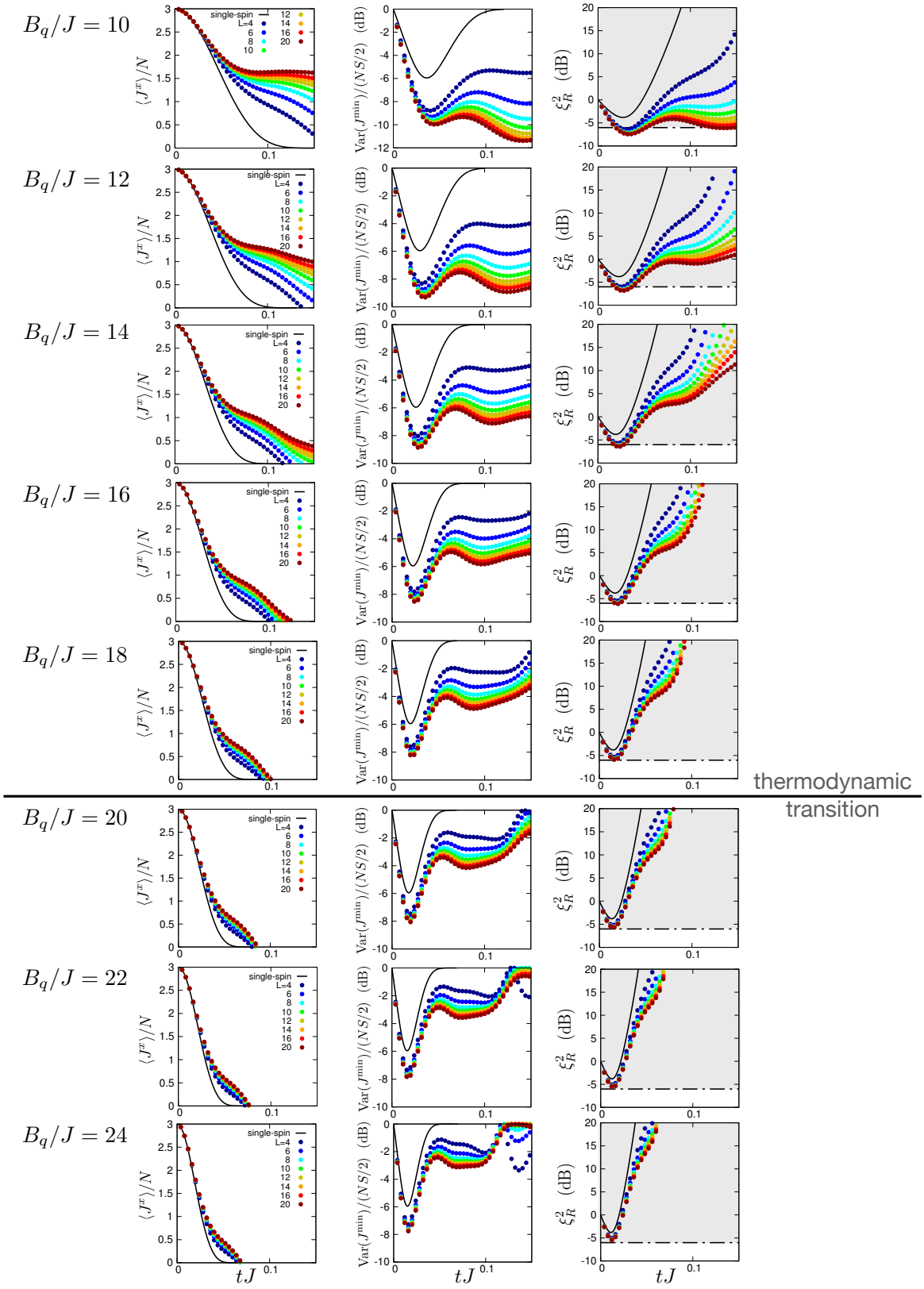

Figure 4.23: Extended data for the dynamics of the 2D dipolar XXZ model with $S = 3$ close to the thermodynamic transition driven by the quadratic Zeeman shift B_q. First column: average magnetization; second column: reduction of the minimum transverse variance with respect to the coherent-spin state value $NS/2$; third column: squeezing parameter.

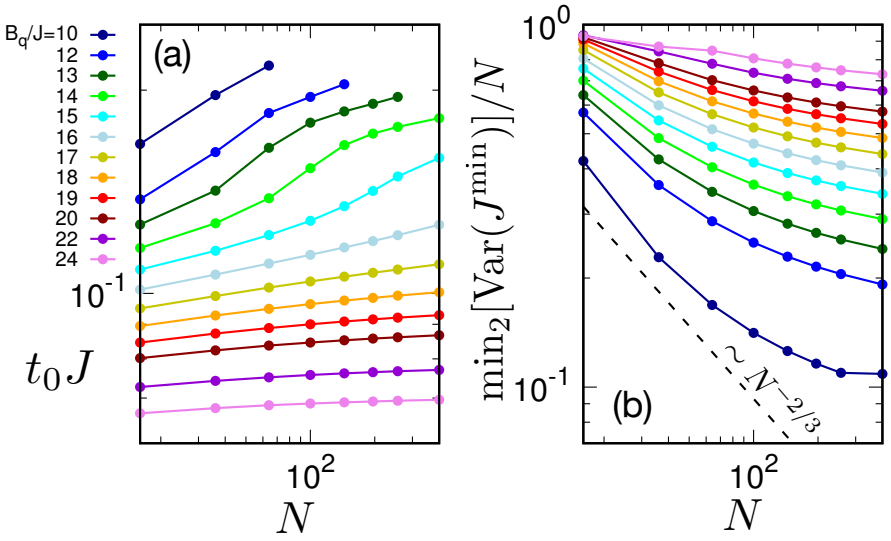

Figure 4.24: Scaling of dynamical features from the TCE results for the $S = 3$ dipolar XXZ model. (a) Time t_0 at which $\langle J^x/N\rangle$ crosses zero; (b) Scaling of the second minimum of $\mathrm{Var}\left(J^{\min}\right)/N$ in time.

threshold $\xi_R^2 = 1/(1+S)$ (for $B_q > 10J$), or even higher than the proper squeezing threshold $\xi_R^2 = 1$ (for $S = 3$ and $B_q > 13J$). This means that we lose collective spin squeezing (i.e. squeezing beyond what can be obtained with a single spin) for values of B_q well below the critical point $B_{q,c}$ at which we lose long-range order in the thermodynamic limit. This situation is not incompatible with scaling of the squeezing parameter (as we can see of figure 4.23), however scaling occurs for values of the squeezing parameter well above the entanglement and squeezing threshold. To see scalable squeezing that is compatible with entanglement - and which would therefore offer many-body metrological advantage compared to single spins [74] - one may need to go to extremely large system sizes, beyond the reach of current experimental setups. Long-range ferromagnetism in the thermalized state is thus only a necessary condition for scalable squeezing during time evolution and in fact this condition can even be relaxed, see [107]. For scalable squeezing to appear at intermediate times not only should $\langle J^x\rangle/N$ not scale to zero, but also $\mathrm{Var}\left(J^{\min}\right)/N$ must scale to ever lower values with increasing size. Such a behaviour is apparent in figure 4.23, and even persisting for $B_q > B_{q,c}$, although a power-law decay of $\mathrm{Var}\left(J^{\min}\right)/N$ with N is not revealed by our data (see figure 4.24 (b)). Therefore our results are not inconsistent the conjecture of Ref. [104] that scalable squeezing persists up to the transition in the thermalized state; yet, for the system sizes we explored, the scaling behaviour close to the transition appears to be very different from (and much slower than) that of the OAT model.

4.5 Conclusions of this chapter

In this chapter, we have shown that the non-equilibrium dynamics of 2D arrays of dipolar large-S spins, initialized in a coherent spin state, features multipartite entanglement in the form of scalable spin squeezing, obeying the scaling of the OAT model for a sufficiently small quadratic Zeeman shift B_q. This validates the hypothesis of separation of variables between collective-spin and spin-wave degrees of freedom. Our results point at the crucial role played by

the quadratic Zeeman shift on the squeezing dynamics of large-S spins – and, more generally, at the competition between single- qudit vs. many-qudit Hamiltonians in the entangling dynamics of qudit ensembles. This picture of separation of variables also allows us to understand better the results we already obtained and discussed in the previous chapter in the case of 1D systems.

The two-dimensional geometries we explored in this chapter are essential for spin-squeezing dynamics to occur: indeed, due to its angular dependence the dipolar interaction averages to zero in three dimensions, so that the collective-spin dynamics is suppressed in 3D. Nonetheless purely 2D arrays of atoms can be realized either by loading a single layer in a three-dimensional optical lattice, or by trapping atoms in quantum-gas-microscope setups [80], as discussed in section 2.3. Hence our work paves the way for the realization of scalable multipartite entanglement in arrays of magnetic atoms (Cr, Er or Dy), representing a most promising platform to realize quantum simulation and quantum information processing with ensembles of qudits.

Chapter 5

Dicke-squeezing dynamics in atomic condensates

In the previous chapter, we studied entanglement dynamics through the evolution of the Wineland spin-squeezing parameter. However, as we mentioned in chapter 2, there exist other forms of spin squeezing, in particular Dicke squeezing which are fully symmetric under rotation around a given axis. In the first section of this chapter, we introduce a generic model for the generation of Dicke squeezing in spinor condensates, via coherent depletion of a condensate mode. We compare the results obtained with exact diagonalization to the ones predicted by a Gaussian Ansatz, and we will focus in particular on the metrological interest of the states generated during the unitary time evolution of the system. We also review different theoretical proposals and experimental realizations of Dicke-squeezing dynamics in spin-1 condensates. In section 5.2, we propose to extend this scheme to the case of squeezing and entanglement for momentum modes, via coherent transfer of particles to opposite-momentum states by periodic modulation of the scattering length of a condensate.

5.1 Dicke squeezing in spinor BEC

In this first section, we will study the generation of entangled states - namely collective Dicke-like states - via the coherent depletion of a condensate of $S = 1$ spins [66, 108].

5.1.1 Derivation of the Hamiltonian

We consider a Bose-Einstein condensate of particles with $S = 1$ spins, in a single spatial mode. The Hilbert space of the system is spanned by the Fock basis of occupation states $|N_{-1}, N_0, N_1\rangle$ for each of the 3 single-spin components along e.g. the z axis, with spin projections $m = 0, \pm 1$. We then introduce the following Hamiltonian, that couple the $m = 0$ mode to the two other modes via a coherent spin-changing collision:

$$\mathcal{H} = \frac{U}{N}\left(a_0 a_0 a_1^\dagger a_{-1}^\dagger + \text{h.c.}\right) + \frac{U_0^{intra}}{2N}\left(a_0^\dagger a_0^\dagger a_0 a_0 + a_1^\dagger a_1^\dagger a_1 a_1 + a_{-1}^\dagger a_{-1}^\dagger a_{-1} a_{-1}\right) + \frac{U_0^{inter}}{2N}\left(a_0^\dagger a_0 a_1^\dagger a_1 + a_1^\dagger a_1 a_{-1}^\dagger a_{-1} + a_0^\dagger a_0 a_{-1}^\dagger a_{-1}\right). \tag{5.1}$$

Here, U/N is the spin-changing collision rate, while U_0^{intra}/N is the interaction energy for two particles in the same mode and U_0^{inter}/N is the interaction energy for two particles in two

different modes. N is the fixed total number of bosons and its presence in the denominator gives to the Hamiltonian the right scaling with particle number, and it descends from the fact that particles are trapped in a mode of volume $V \sim N$. From a pure condensate in the $m = 0$ mode $|0, N, 0\rangle$, the spin-changing collisions can create pairs of atoms in the 1 and -1 modes. The intraspecies and interspecies interaction terms, depending on the sign of U_0^{intra} and U_0^{inter}, can favour or disfavour a mixture of the three modes.

In the case where all the intraspecies interactions strength are the same, we can rewrite the intraspecies interaction terms in terms of the interspecies interaction terms and a constant term, $\left(N_0^2 + N_1^2 + N_{-1}^2\right) = N^2 - 2\left(N_0N_1 + N_0N_{-1} + N_1N_{-1}\right)$, such that:

$$\begin{aligned}&\frac{U_0^{intra}}{N}\left(N_0^2 + N_1^2 + N_{-1}^2\right) + \frac{U_0^{inter}}{N}\left(N_0N_1 + N_0N_{-1} + N_1N_{-1}\right)\\ =&\frac{U_0}{N}\left(N_0N_1 + N_0N_{-1} + N_1N_{-1}\right) + \text{cste.}\end{aligned}$$

with $U_0 = U_0^{inter} - 2U_0^{intra}$. In the following we will omit the normalization factor N, which can be simply re-instated when considering the scaling of time scales for the dynamics. With this convention our Hamiltonian becomes:

$$\mathcal{H} = U\left(a_0a_0a_1^\dagger a_{-1}^\dagger + \text{h.c.}\right) - U_0\left(a_0^\dagger a_0 a_1^\dagger a_1 + a_0^\dagger a_0 a_{-1}^\dagger a_{-1} + a_1^\dagger a_1 a_{-1}^\dagger a_{-1}\right). \tag{5.2}$$

This Hamiltonian is symmetric under the exchange $1 \leftrightarrow -1$. In the following, we will always consider a quench dynamics, starting from a pure condensate of $m = 0$ single-spin states $|0, N, 0\rangle$. Since this initial state is also symmetric under the exchange $1 \leftrightarrow -1$ the dynamics will only explore the states with the same particle numbers $N_1 = N_{-1}$. The only states to consider in the Fock basis are thus of the form $|k, N - 2k, k\rangle$. This reduces the Hilbert space dimension to $\text{Int}(N/2) + 1$, which is linear in N, and which allows for light calculations with ED even for large $N \gtrsim 1000$.

Starting from a condensate in $m = 0$, which corresponds to the product state $\otimes^N|m = 0\rangle$, the dynamics in induced by spin-changing collisions. The first questions one can ask are: what is the maximal population transfer, namely $(N_1 + N_{-1})_{\max}$, over time for different values of the ratio U_0/U? And how does the ratio $(N_1 + N_{-1})_{\max}/N$ evolve for increasing N at a fixed ratio U_0/U?

Figure 5.1 shows indeed that the number of atoms in the $m = \pm 1$ states increases in time, until it reaches a maximum. The maximum population transfer depends on the ratio U_0/U: the smaller this ratio, the larger $(N_1 + N_{-1})_{\max}/N$. Moreover the population dynamics is the same under the transformation $U_0 \to -U_0$. Therefore we can study the scaling of $(N_1 + N_{-1})_{\max}/N$ with N only for positive U_0 (figure 5.2b).

This scaling is shown in figure 5.2a. As we can see, for $U_0 \lesssim 0.9U$, we have a macroscopic proportion of the initial condensate that is transferred to the $m = \pm 1$ modes, whereas for $U = U_0$ most of the atoms remain in the initial mode $m = 0$. This indicates the presence of a dynamical phase transition that occurs for $0.9U < U_0 < U$. Moreover, for $N \approx 1000$, the ratio $(N_1 + N_{-1})_{\max}/N$ seems to have converged to a size-independent value. This value is shown in figure 5.2b as function of U_0/U.

The evolution of spin populations gives only very partial information on the nature of the states generated along the dynamics. Indeed, we expect this coherent depletion dynamics to generate a collective Dicke-like state, close to $|F, M = 0\rangle$, with $F < NS = N$ (here $S = 1$). These states are characterized by a zero variance of the collective spin along z; as well as

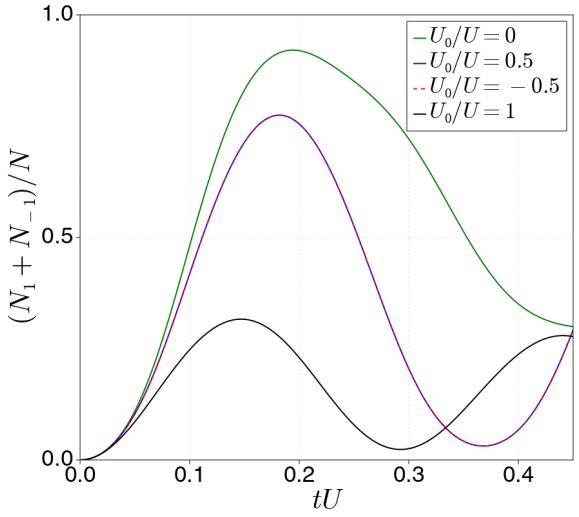

Figure 5.1: Time evolution of the mean populations in the modes $m \pm 1$, $(N_1 + N_{-1})/N$, for $N = 20$ and various values of U_0.

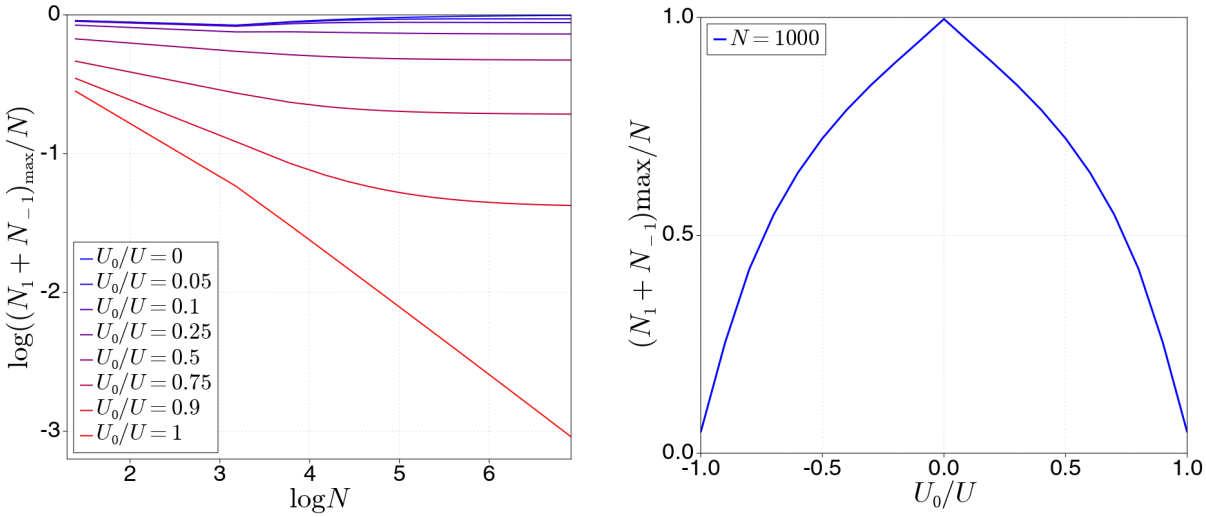

(a) $\log((N_1 + N_{-1})_{\max}/N)$ versus $\log N$ (b) $(N_1 + N_{-1})_{\max}/N$ versus U_0/U

Figure 5.2: (a) Scaling of $(N_1 + N_{-1})_{\max}/N$ versus N for different values of U_0/U in log scale and (b) $(N_1 + N_{-1})_{\max}/N$ versus U/U at $N = 1000$.

macroscopic collective-spin length, and therefore they allow for very precise measurements of rotations around the x or y axis.

5.1.2 Study of the metrological properties

In the following, we want to estimate the best sensitivity we can achieve with respect to rotations around the x axis by using the states produced by the dynamics. First, we need to introduce the collective-spin operators for the spinor gas:

$$J^z = \sum_{m=-1}^{1} m a_m^\dagger a_m = a_1^\dagger a_1 - a_{-1}^\dagger a_{-1}, \quad J^+ = \sum_{m=-1}^{0} \sqrt{2} a_{m+1}^\dagger a_m = \sqrt{2}\left(a_1^\dagger a_0 + a_0^\dagger a_{-1}\right). \tag{5.3}$$

Note that this corresponds to the generalized Schwinger-boson transformation introduced in Eq. 2.18, applied to the case $S = 1$. For a rotation of an angle θ around the x axis, starting from a state $|\Psi\rangle$, the uncertainty on the estimate of θ by measuring a variation of $(J^z)^2$ is given by:

$$(\delta\theta)^2(\theta) = \frac{\mathrm{Var}\left((J_\theta^z)^2\right)}{\left(\frac{\partial\langle(J_\theta^z)^2\rangle}{\partial\theta}\right)^2} \tag{5.4}$$

with $J_\theta^z = \cos\theta J^z - \sin\theta J^y$. Variance and mean value $\langle\dots\rangle$ refer to the state $|\Psi\rangle$. The choice of $(J^z)^2$ as the operator to measure is motivated by the fact that we expect a very small variance of this operator in the case of a Dicke-like state.

We can rewrite the denominator of Eq. 5.4 as:

$$\frac{\partial\langle(J_\theta^z)^2\rangle}{\partial\theta} = -i\langle\left[(J_\theta^z)^2, J_\theta^x\right]\rangle = \langle J_\theta^z J_\theta^y\rangle + \langle J_\theta^y J_\theta^z\rangle \tag{5.5}$$

with $J_\theta^y = \cos\theta J^y + \sin\theta J^z$ and $J_\theta^x = J^x$. This leads to the following expression for $\delta\theta$:

$$(\delta\theta)^2(\theta) = \frac{\mathrm{Var}\left((J_\theta^z)^2\right)}{\left(\langle J_\theta^z J_\theta^y\rangle + \langle J_\theta^y J_\theta^z\rangle\right)^2}. \tag{5.6}$$

We label $(\delta\theta)_{\min}$ the minimal uncertainty over all possible values of θ, and we recall (from chapter 1) that it is bounded from below as specified by the Quantum Cramér-Rao bound [6]:

$$(\delta\theta)^2_{\min} \geq \frac{1}{\mathcal{F}(J^x)} \tag{5.7}$$

with $\mathcal{F}(J^x)$ the Quantum Fisher information of the state with respect to rotations around x. For pure states, we have $\mathcal{F}(J^x) = 4\langle(J^x)^2\rangle$, which gives us the following bound for $(\delta\theta)^2_{\min}$:

$$(\delta\theta)^2 \geq \frac{1}{4\langle(J^x)^2\rangle}. \tag{5.8}$$

This tells us that the larger the value of $\langle(J^x)^2\rangle$, the better estimate of θ we can reach. Therefore we can first have a look at the evolution of the mean value of $(J^x)^2$ in time, and especially of the maximum reached $(J^x)^2_{\max}$ for a given system size N and ratio U_0/U. We will focus in particular on the scaling of $(J^x)^2_{\max}$ with system size N, as it will allow us to determine the metrological gain we can achieve with respect to single spins. In particular, $\langle(J^x)^2\rangle$ growing as N^2 indicates that we can reach Heisenberg scaling for metrology.

5.1.3 Exact results for the dynamics

We thus studied the time evolution of $\langle(J^x)^2\rangle$ starting from the initial state $|0, N, 0\rangle$ for different values of $\frac{U_0}{U}$ from -1 to 1, and for different values of N.

We show the results of time evolution of $\langle(J^x)^2\rangle/N^2$ for a few values of U_0/U in figure 5.3. We also put the results for the population transfer for comparison. First, one can notice that there is an asymmetry between the case $U_0 > 0$ and the case $U_0 < 0$, thus we will have to

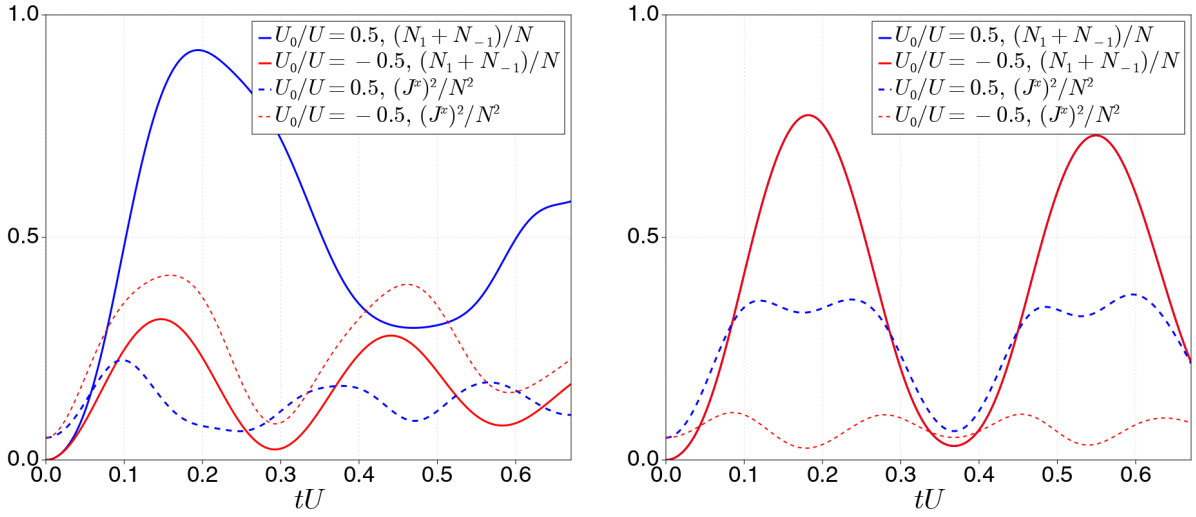

Figure 5.3: Time evolution of $\langle (J^x)^2 \rangle$ (solid lines) and of the mean populations in the modes $m \pm 1$, $(N_1 + N_{-1})/N$ (dashed lines), for $N = 20$ and various values of U_0, (a) $U_0 = 0$ and 1 and (b) $U_0 = 0.5$ and -0.5.

study both cases $U_0 < 0$ and $U_0 > 0$. Indeed, it is possible to introduce the following phase transformation for the bosonic operators:

$$\tilde{a}_0 = a_0 e^{i\pi/4}, \quad \tilde{a}_{\pm 1} = a_{\pm 1} e^{-i\pi/4}. \tag{5.9}$$

The effect of this transformation is to change the relative sign of U and U_0, as it maps $a_0^\dagger a_0^\dagger a_1 a_{-1}$ onto $-a_0^\dagger a_0^\dagger a_1 a_{-1}$, while the spin populations $N_0, N_{\pm 1}$ remains unchanged. This explains the origin of the symmetry between $\pm U_0$ in the time evolution of the spin populations. On the other hand, we have, for $(J^x)^2$:

$$\begin{aligned}
\langle \left(\tilde{J}^x\right)^2 \rangle &= \frac{1}{4} \left\langle \left(\tilde{a}_1^\dagger \tilde{a}_0 + \tilde{a}_0^\dagger \tilde{a}_{-1}\right) \left(\tilde{a}_{-1}^\dagger \tilde{a}_0 + \tilde{a}_0^\dagger \tilde{a}_1\right) + \left(\tilde{a}_{-1}^\dagger \tilde{a}_0 + \tilde{a}_0^\dagger \tilde{a}_1\right) \left(\tilde{a}_1^\dagger \tilde{a}_0 + \tilde{a}_0^\dagger \tilde{a}_{-1}\right) \right\rangle \\
&= \frac{1}{4} \left\langle -a_1^\dagger a_{-1}^\dagger a_0 a_0 - a_0^\dagger a_0^\dagger a_1 a_{-1} + a_1^\dagger a_1 a_0 a_0^\dagger + a_0^\dagger a_0 a_{-1} a_{-1}^\dagger \right\rangle \\
&+ \frac{1}{4} \left\langle -a_1^\dagger a_{-1}^\dagger a_0 a_0 - a_0^\dagger a_0^\dagger a_1 a_{-1} + a_{-1}^\dagger a_{-1} a_0 a_0^\dagger + a_0^\dagger a_0 a_1 a_1^\dagger \right\rangle
\end{aligned} \tag{5.10}$$

which is clearly not invariant under the phase transformation that maps U_0 unto $-U_0$. We also observe that the time at which we obtain the maximum population transfer does not always coincide with the time at which $\langle (J^x)^2 \rangle / N^2$ is maximal.

We then study the scaling of $\langle (J^x)^2_{\max} \rangle / N^2$ - the maximum value of $\langle (J^x)^2 \rangle / N^2$ during the time evolution - with the system size N. We show our results in figure 5.4. For both $U_0 > 0$ and $U_0 < 0$, we observe Heisenberg scaling of $\langle (J^x)^2 \rangle$ as long as $|U_0| \lesssim 0.85U$. However, one can notice from the different scales on the vertical axis that for $U_0 > 0$ we observe a higher prefactor λ for Heisenberg scaling (such that $\langle (J^x)^2_{\max} \rangle \sim \lambda N^2$) for $U_0 > 0$. The λ prefactor is plotted in figure 5.5 as a function of U_0/U. In both cases we observe a dynamical transition at $|U_0| \approx U$ for which we observe that $\langle (J^x)^2_{\max} \rangle / N^2$ goes to zero for increasing system sizes.

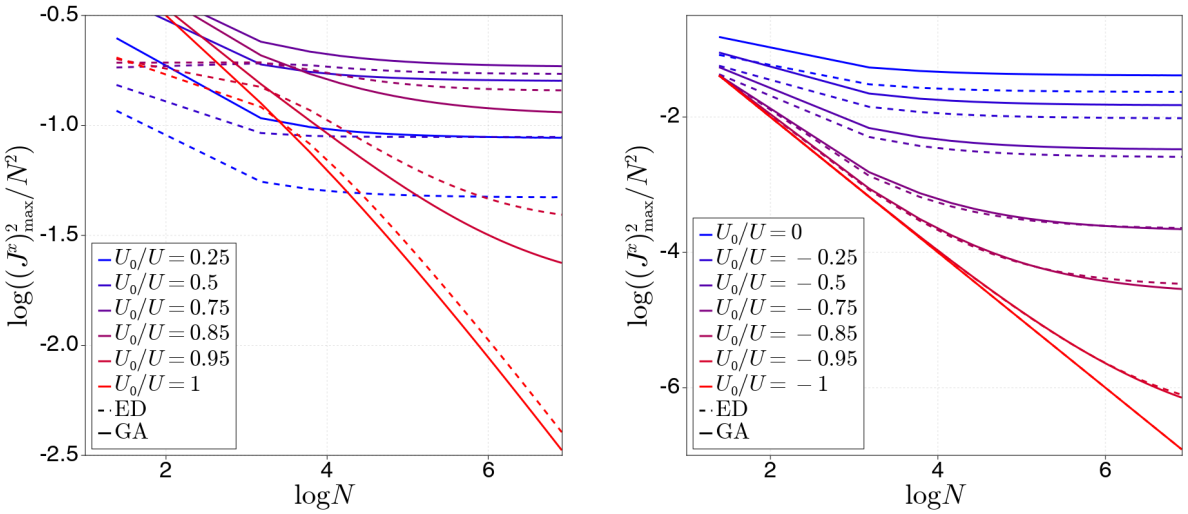

Figure 5.4: Maximum value of $\langle (J^x)^2 \rangle$ reached during the dynamics vs $\log(N)$ for different positive (a) and negative (b) values of U_0. Dashed lines correspond to ED results, while the solid lines correspond to GA results.

5.1.4 Dynamics from a Gaussian Ansatz

Finally, we compared the results obtained with ED with results obtained with an approximate method, based on the Gaussian Ansatz for the evolved state. In the case of $S = 1$ spinor condensates, we could rely only on exact numerical results, as we have light exact numerical calculations with only three modes. However, we aim to generalize the 3-mode problem to the case of many momentum modes. In that case, we cannot rely on ED anymore for large system sizes. Therefore we want to benchmark our Gaussian Ansatz in the case where we also have ED results to compare with, in order to determine how reliable the results predicted by the GA are. We detail the equations of motion of the Gaussian ansatz (GA) in Appendix C.1. As we can see in figure 5.4, it appears that we have good agreement (even though not perfect) between the exact and approximate numerical methods. In particular, the Gaussian ansatz is able to predict the dynamical transition observed with ED. From the previous figure, we can see that the value $\langle (J^x)^2_{\max} \rangle / N^2$ reaches a plateau for $N \gtrsim 1000$, therefore we can study more in details the scaling of $\langle (J^x)^2_{\max} \rangle / N^2$ at fixed $N = 1000$ for various values of U_0, and we show our results in figure 5.5. There, we observe that both the ED and GA results predict a maximum for $U_0 \approx 0.75U$, with $\lambda \approx 0.5$.

Finally, we investigate the time needed to reach the state that corresponds to $\langle (J^x)^2_{\max} \rangle$, and its scaling with system size. This is important because if the time needed to reach Heisenberg scaling is too long, it will be out of reach for any realistic experiment. We show our results from both ED and GA in figure 5.6. As we can see, we have a time t_{max} that scales approximately as $N^{-0.85}$ in the optimal case $U_0 = 0.75U$ (and the power seems to remain the same for values of U_0 such that $0.25U < U_0 < 0.85U$). However, we have to keep in mind that we must consider an extensive Hamiltonian, i.e. we must rescale $U, U_0 \to U/N, U_0/N$, which leads to $t_{\max} \sim N^{0.15}$. This is still a rather favourable scaling and potentially compatible with current experimental platforms, reaching a few thousands atoms [66, 108, 109]. As we can see in figure 5.6b, for $N = 1000$, we only need to reach a time of order $tU \sim 6$, namely only ≈ 6 interaction times.

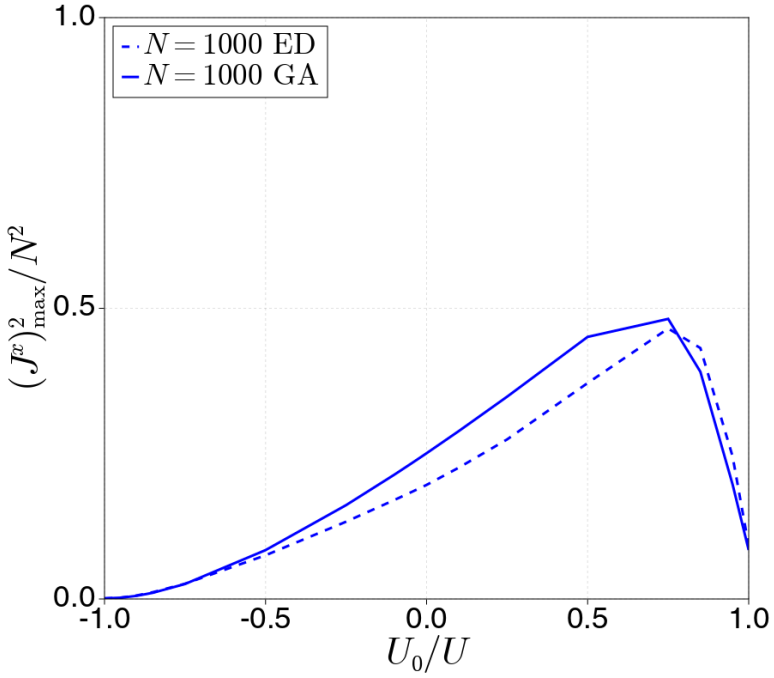

Figure 5.5: Maximum value of $\langle (J^x)^2 \rangle$ reached during the dynamics vs $\log(N)$ versus U_0/U for $N = 1000$.

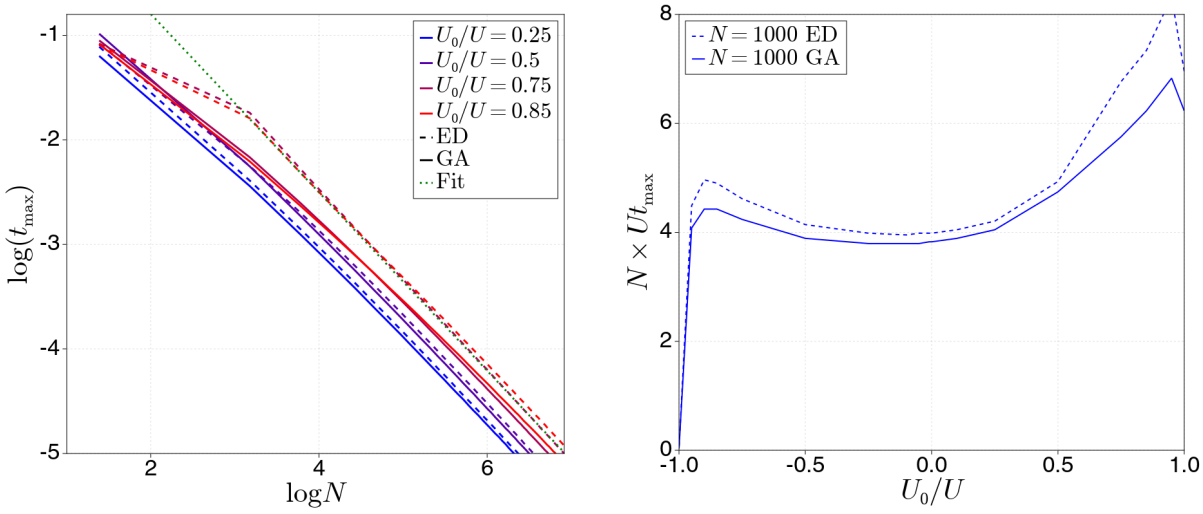

(a) (b)

Figure 5.6: (a) Scaling of $t_{\max}$ with system size, for different values of U_0. The black dotted fit is here to guide the eye, and corresponds to N^α with $\alpha = -0.85$. (b) $N \times U t_{\max}$ versus U_0/U, for a fixed $N = 1000$. Dashed lines correspond to ED results, while the solid lines correspond to GA results.

5.1.5 Sensitivity to rotations

We can now go back to the sensitivity to rotations, and compute $(\delta\theta)^2$ (as defined in Eq. 5.6) versus θ for the state that maximises $\langle (J^x)^2 \rangle$ for a given N and U_0/U. Both for ED and GA, we work with the rotated operators. The expression of the powers of collective spins within the

GA framework are detailed in Appendix C.2.

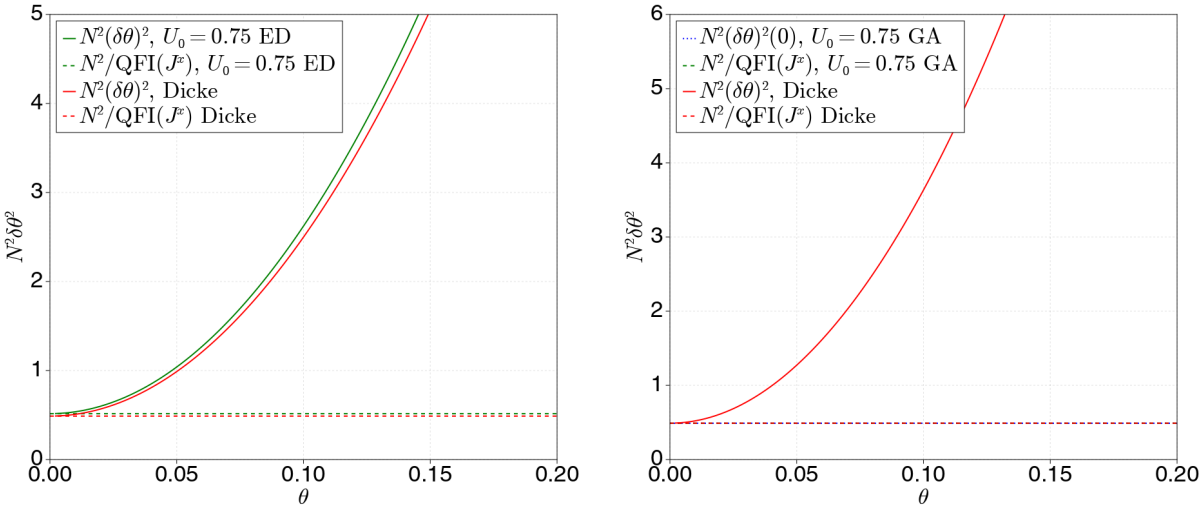

(a) ED (b)

Figure 5.7: (a) Uncertainty on the phase estimation $N^2\delta\theta\,(\theta)$ versus θ for the optimal state obtained during the dynamics with ED (green) compared to the uncertainty with a perfect Dicke state $|N, m = 0\rangle$ for $N = 40$, $U_0/U = 0.75$. The dashed lines show the QFI for both states. (b) Same plot, but the ED results are replaced with the GA ones. For $\delta\theta$, we only show the limit for $\theta \to 0$ (blue dotted line). We also have taken $N = 50$, since GA allows to study larger system sizes.

in figure 5.7a, we first show the uncertainty on the phase $\delta\theta$ one can obtain with a perfect Dicke state $|N, m = 0\rangle$, and compare it with that of the state obtained during time evolution (with ED) that maximises $\langle (J^x)^2 \rangle$ for $N = 40$, $U_0 = 0.75U$. We also plot for both states the Quantum Fisher Information associated with a rotation around J^x. For Dicke states, there is an analytical expression, given by [38]:

$$\mathcal{F}\left(|N, m = 0\rangle, J^x\right) = 2N\left(N + 1\right). \tag{5.11}$$

As we can see, measuring $(J^z)^2$ under rotation gives the best possible estimate of the rotation angle when $\theta \to 0$, as $\delta\theta$ reaches the lower bound imposed by the QFI. We also notice that the state obtained during the dynamics allows for an estimate almost as good as that of a perfect Dicke state (as expected from the scalability of $\langle (J^x)^2_{\max} \rangle$ with N in the case $U_0 = 0.75U$). In the large N limit, we thus expect an uncertainty that scales as $\delta\theta^2 \sim \lambda/(N^2)$ with $\lambda \approx 0.5$ according to our numerical results. We then show the results obtained with the GA method in figure 5.7b. In the case of GA, in order to study the evolution of $\delta\theta$ with θ, we need to express $\langle (J^y)^4 \rangle$ in terms of first-order and second-order correlation functions, which requires heavy analytical calculation. However, as shown before we are only interested in the optimal sensitivity, which is obtain in the limit $\theta \to 0$. Therefore, we will restrain ourselves only to the value $\delta\theta\,(0)$ (blue dotted line) and compare it with the QFI of the state. Again, we can see that both curves coincide, and they also match the results of the perfect Dicke State $|N, m = 0\rangle$.

5.1.6 Details about the Gaussian Ansatz

The Gaussian Ansatz, even though approximate, gives correct predictions on the scaling of the different parameters of interest ($\delta\theta$, $\langle (J^x)^2_{\max}\rangle$ and $t_{\max}$) and it allows us to study system sizes we could not reach with ED, especially if we want to consider more than just 3 condensate modes.

One of the main differences between the GA and ED simulations is that we start the ED simulations with a single Fock state, with a fixed total atom number N, whereas for the GA simulations we assume that our initial state is a coherent state (with average number of atoms N), corresponding to the best gaussian approximation to a Fock state. In particular, this state is a superposition of several Fock states with various atom numbers, and an uncertainty of $\delta N = \sqrt{N}$ around the mean value N.

We first checked that by starting the ED simulations with a coherent state instead of a Fock state, we obtained similar results in the limit of large N (which is expected, as the relative uncertainty $\delta N/N$ goes to 0 for $N \to \infty$. We show the time evolution of $\langle (J^x)^2\rangle/N^2$ for both initial states in figure 5.8. As we can see, for increasing N, we see less and less difference between the two initial state, and in particular they give the same prediction for the first maximum of $\langle (J^x)^2\rangle$.

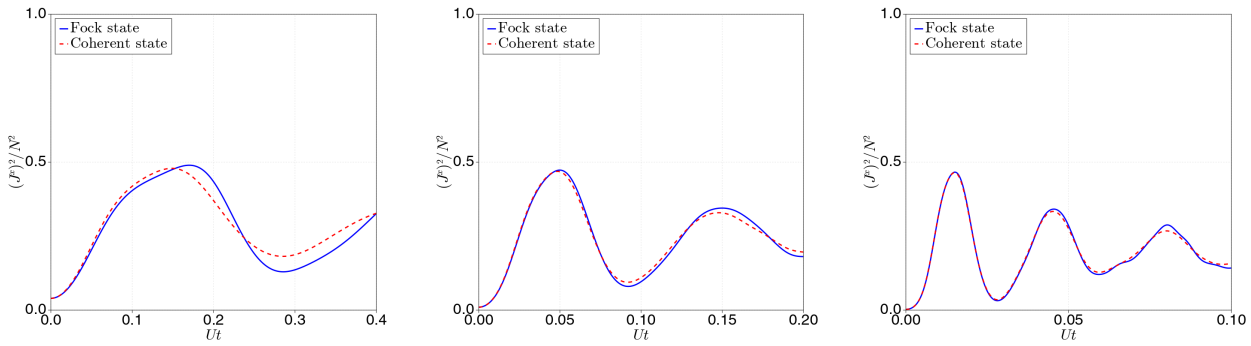

(a) $N = 25$ (b) $N = 100$ (c) $N = 400$

Figure 5.8: Time evolution of $\langle (J^x)^2\rangle$ starting from a Fock state (solid blue) and a coherent initial state (dashed red) with the same mean atom number $N = 25$ (a), $N = 100$ (b) and $N = 400$ (c). All the simulations have been performed with $U = 1$ and $U_0 = 0.75$.

Using ED simulations starting with a coherent state, we could also compute the evolution in time of second-order and third-order cumulant functions, and compare them with the prediction of the Gaussian ansatz. In particular, we introduce the following third order cumulants:

$$Q_1 = \langle a_0 a_1 a_{-1}\rangle - \langle a_0\rangle\langle a_1 a_{-1}\rangle, \quad Q_2 = \langle a_0^\dagger a_1 a_{-1}\rangle - \langle a_0^\dagger\rangle\langle a_1 a_{-1}\rangle \tag{5.12}$$

which by definition remain zero at all times for the GA. We also compare ED and GA results for the second-order cumulant $F_{1-1} = \langle a_1 a_{-1}\rangle$. As we can see in figure 5.9, after some time, third-order cumulants start building up, and this corresponds to the time at which deviations appears between the ED and GA predictions for the two-point cumulant F_{1-1}. Nonetheless, they remain rather small at all times.

This indicates that if we want to improve our Gaussian Ansatz we have to consider higher-order cumulants. We tried to study the time evolution of the system with a 3rd order TCE, but this led to problems with energy conservation. We assume that this is due to the fact that

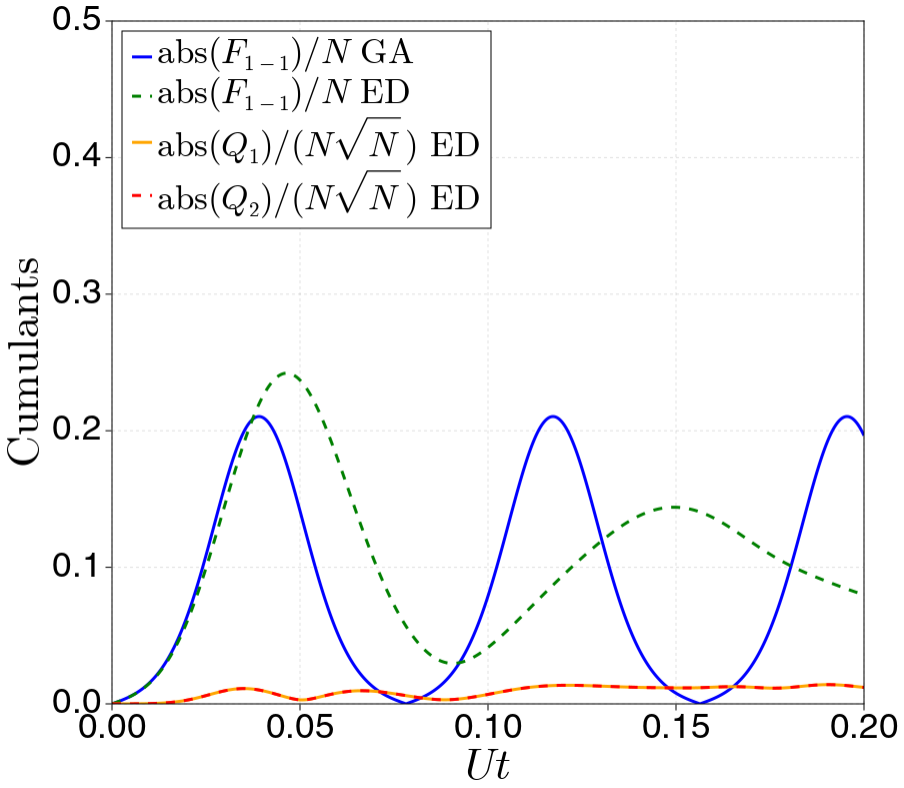

Figure 5.9: Time evolution of 2nd and 3rd order cumulant functions, starting from a coherent state for GA and ED simulations. All the simulations have been performed with $N = 100$, $U = 1$ and $U_0 = 0.75$.

there exist non physical states for which only the 3 first cumulant orders are non zero, and these states would push the dynamics outside of the space of relevant physical states. We did not try to include 4th order cumulants as it leads to rather lengthy expression, but this represents a direction for future works.

5.1.7 Experimental realizations

Many experiments have been able to realize Hamiltonians similar to the one we studied in this first section, using for instance condensates of ^{87}Rb atoms in the manifold $F = 1$ [66, 108, 109] or $F = 2$ [110, 111]. Two main schemes emerge have been explored for the production of highly entangled states, both starting from an initial state where all the atoms are in the state $|F, m_F = 0\rangle$. The first possibility is to let the system evolve under a unitary dynamics with a Hamiltonian similar to the one presented before, leading to a coherent pair creation of spins in the $m_F = \pm 1$ states that is analogous to parametric down-conversion in optical systems [110, 111]. With this method, a squeezing of $-11.4(5)$ dB was measured using the squeezing parameter presented in Eq. 2.24, corresponding to an entanglement depth of at least 28 atoms in a system of $N = 8000$ atoms of ^{87}Rb [66]. The second method consists in varying adiabatically an external magnetic field in order to cross a quantum phase transition, resulting from the competition between the spin-changing collisions and a quadratic Zeeman field that creates an energy difference between the $m = 0$ state and the $m = \pm 1$ states [108, 109, 112].

The Hamiltonian is the following:

$$\mathcal{H}_{\mathrm{QPT}} = \frac{c_2}{N}\left(a_1^\dagger a_{-1}^\dagger a_0 a_0 + \mathrm{h.c.}\right) + \frac{c_2}{N}\left(N_0 N_1 + N_0 N_{-1}\right) - qN_0 \tag{5.13}$$

with q the quadratic Zeeman shift. Note that this Hamiltonian is similar to the one discussed previously, with two main differences. First, there is one term missing in the interspecies interactions (proportional to $N_1 N_{-1}$). Secondly, there is now a quadratic Zeeman shift that leads to off-resonant spin-exchange collisions if too large. Starting with a large positive $q \gg |c_2|$, the ground state is simply a factorized state, where all the atoms are in the $m = 0$ state. By adiabatically ramping down q to zero, the system crosses a quantum phase transition, and the state of the system becomes close to the Dicke state $|N, 0\rangle$ [108]. We tried to compare the results on the uncertainty $\delta\theta$ obtained with the adiabatically prepared state with those of a perfect Dicke state. For the state obtained adiabatically, we simply took the ground state of the above Hamiltonian, and in the case $q = 0$, and $c_2 = -1$ (as c_2 is negative for ^{87}Rb [113]). We show the comparison for the different states in figure 5.10. Interestingly, in the experiment, the minimal uncertainty is not reached in the limit $\theta \to 0$ but for a (small) finite θ. We assume that this is due to experimental imperfection, and we tried to simulate that by adding a small noise, of order $1/N^4$ on the the coefficient of the wavefunction in the Fock basis $|N_{-1}, N_0, N_1\rangle$. By doing so, we indeed have a minimum uncertainty for a finite θ, and an uncertainty that diverges for $\theta \to 0$. In a more recent experiment using the same techniques, a squeezing of 16.6 ± 1.3 dB was recorded for the phase sensing with a Ramsey interferometer in a system of $N = 26400$ atoms [114].

5.2 Dicke squeezing in momentum space

We now study the realization of Dicke-like states in spinless condensates, by taking into account the momentum degrees of freedom instead of the spin degrees of freedom. In momentum space, the condensate corresponds to a momentum $k = 0$. If there exists a depletion mechanism that specifically couples the $k = 0$ mode to two modes at $k = \pm k_0$, the 3-mode system can be mapped onto a system of bosons with effective $S = 1$ spin. One can therefore use the results obtained previously to monitor the entanglement and Dicke squeezing produced in time, but now in momentum space.

In the first subsection, we derive the interaction Hamiltonian for different momentum components. In the second subsection, we show how we can reproduce the results of the previous section by modulating in time the scattering length of the spin collisions. Finally in the last subsection we try to generalize these results to the case of more than three momentum modes.

5.2.1 Dicke squeezing from Faraday instability

We first consider the case of a 1D system for simplicity. For a contact interaction in real space $g\delta(r)$, the interaction in momentum space takes the following form:

$$\mathcal{H}_{int} = \frac{U}{N_S}\sum_{k,k'q} a_{k-q}^\dagger a_{k'+q}^\dagger a_k a_{k'} \tag{5.14}$$

with $U = ga^d$ and $N_S = V/a^d$ the dimensionless volume (in units of a^d, which can be thought of as e.g. the unit-cell volume in an optical lattice). The kinetic energy is analogous to a

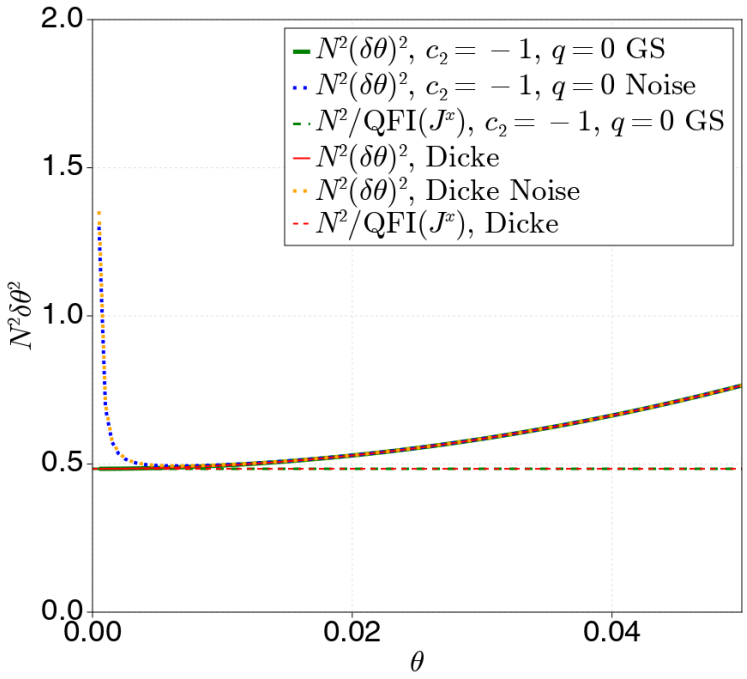

Figure 5.10: Uncertainty on the phase estimation $N^2\delta\theta\,(\theta)$ versus θ for the $\mathcal{H}_{\mathrm{QPT}}$ ground state ($c_2 = -1$, $q = 0$) compared to the uncertainty with a perfect Dicke state $|N, m = 0\rangle$ for $N = 30$. The dotted lines show the uncertainty when adding a random noise of order $1/N^4$ to each of the components of the two states. The dashed lines show the QFI for the ideal Dicke state and $\mathcal{H}_{\mathrm{QPT}}$ ground state.

quadratic Zeeman field B_q, adding an energy offset to the different modes:

$$\mathcal{H}_{tot} = \frac{U}{N_S} \sum_{k,k'q} a^\dagger_{k-q} a^\dagger_{k'+q} a_k a_{k'} + B_q \sum_k k^2 N_k. \tag{5.15}$$

Note that the quadratic Zeeman term suppresses the collision terms if $B_q \gg U/N_S$, as collisions become off-resonant. In particular, if we start with a pure condensate with all the atoms at zero momentum $k = 0$, the system will remain frozen in that state. In order to have population transfer from the $k = 0$ mode and Dicke squeezing, we can think of modulating in time the coupling constant U, at a frequency ω: $U(t) = U_0/2 + U_1 \sin(\omega t + \phi)$. This can create Faraday waves in the system, leading to a spatial modulation of the ground state, namely a non zero population in two modes $\pm k_0$. This has been observed in BEC in various experiments, through the periodic modulation of the scattering length by using a Feshbach resonance [115–117].

In a first approximation, we will limit ourselves to only three modes, $k = 0$ and $k = \pm k_0$, we will note $N_{\pm 1}$ the populations in the $\pm k_0$ modes, and we will absorb a factor k_0^2 in the definition of $B_q = \hbar^2 k_0^2/(2m)$ from now on. By doing so, we can rewrite our Hamiltonian in the following way:

$$\begin{aligned}\mathcal{H}_{tot} &= \frac{U}{N_S} \sum_{k,k'q} a^\dagger_{k-q} a^\dagger_{k'+q} a_k a_{k'} + B_q \sum_{k=-1,0,1} \frac{k^2}{k_0^2} N_k \\ &= \frac{2U}{N_S} \left(a^\dagger_0 a^\dagger_0 a_1 a_{-1} + \text{h.c.} \right) + \frac{2U}{N_S} \left(N_0 N_1 + N_0 N_{-1} + N_1 N_{-1} \right) + B_q \left(N_1 + N_{-1} \right)\end{aligned} \tag{5.16}$$

up to a constant. We thus have the same Hamiltonian as in the previous section, but now with the addition of the quadratic Zeeman term. By tuning the frequency and phase of the modulation of $U(t)$, it will be possible to eliminate this off resonant term and create Dicke-like states and squeezing in the system during the dynamics. Since we have a periodic modulation of our Hamiltonian in time, it corresponds to a Floquet Hamiltonian. To study it exactly we will use Lanczos algorithm instead of full ED in the following subsection.

5.2.2 Modulation of the scattering length and rotating-wave approximation

The first step is to determine the modulation frequency ω at which we have resonant population transfer in our system, as it is the mechanism leading to the formation of Dicke-like states. This frequency can be determined either by doing different numerical simulations at fixed B_q and for various ω, or by computing analytically the Hamiltonian in a rotating frame. The rotating frame which eliminates the quadratic Zeeman term is given by the transformation $\mathcal{U} = \exp\left(-iB_q t \sum_k k^2 N_k\right)$. In our 3-mode system, it simply reads as $\mathcal{U} = \exp\left[-iB_q t \left(N_1 + N_{-1}\right)\right]$. In this rotating frame, both positive and negative momentum operators rotate with the same phase. If we rewrite the Hamiltonian in this new frame:

$$\mathcal{H}_{\text{RF}} = \mathcal{U}\mathcal{H}\mathcal{U}^\dagger + i\frac{\partial \mathcal{U}}{\partial t}\mathcal{U}^\dagger, \tag{5.17}$$

we get:

$$\begin{aligned}\mathcal{H}_{\mathrm{RF}}(\omega,\phi) &= \frac{2U(t)}{N_S}\left(a_0^\dagger a_0^\dagger a_1 a_{-1} e^{-2iB_q t} + \text{h.c.}\right) + \frac{2U(t)}{N_S}\left(N_0N_1 + N_0N_{-1} + N_1N_{-1}\right) \\ &= \frac{U_1}{iN_S}\left(a_0^\dagger a_0^\dagger a_1 a_{-1} e^{i(\omega-2B_q)t+i\phi} - a_1^\dagger a_{-1}^\dagger a_0 a_0 e^{-i(\omega-2B_q)t-i\phi}\right) \\ &+ \frac{U_0}{N_S}\left(N_0N_1 + N_0N_{-1} + N_1N_{-1}\right) + \frac{U_0}{N_S}\left(a_0^\dagger a_0^\dagger a_1 a_{-1} e^{-2iB_q t} + \text{h.c.}\right) \\ &+ \frac{U_1\left(e^{i\omega t+i\phi} - e^{-i\omega t-i\phi}\right)}{iN_S}\left(N_0N_1 + N_0N_{-1} + N_1N_{-1}\right) \\ &+ \frac{U_1}{iN_S}\left(a_1^\dagger a_{-1}^\dagger a_0 a_0 e^{i(\omega+2B_q)t+i\phi} - a_0^\dagger a_0^\dagger a_1 a_{-1} e^{-i(\omega+2B_q)t-i\phi}\right). \end{aligned} \tag{5.18}$$

From this expression, it is clear that in order to have non-rotating collision terms in the limit of large B_q, we must take $\omega = \pm 2B_q$. Similarly, when looking numerically at the maximum population transfer for various values of ω during the time evolution of the system we find a resonance condition for $\omega = 2B_q$ (see figure 5.11). Note that a large value of $|U_0| > |U_1|$ can shift this condition (see figure 5.11c), but since we are interested in the case where we have the largest variance of J^x - which corresponds to $|U_0| < |U_1|$ from the previous section results - from now on we will only consider the case $\omega = 2B_q$.

By imposing $\omega = 2B_q$, and assuming that we have a very large $B_q \gg U_1, U_0$, we can perform a rotating-wave approximation (RWA) and eliminate all the rotating terms. In doing so, we obtain the following Hamiltonian:

$$\mathcal{H}_{\mathrm{RWA}}(\phi) = \frac{U_1}{iN_S}\left(a_0^\dagger a_0^\dagger a_1 a_{-1} e^{i\phi} - a_1^\dagger a_{-1}^\dagger a_0 a_0 e^{-i\phi}\right) + \frac{U_0}{N_S}\left(N_0N_1 + N_0N_{-1} + N_1N_{-1}\right). \tag{5.19}$$

We can see that we recover a Hamiltonian very similar to the one of Eq. 5.2, with U_1 playing the role of U. Note also that the phase ϕ is important: by taking $\phi = \pi/2$ or $\phi = 3\pi/2$, one gets:

$$\mathcal{H}_{\mathrm{RWA}}\left(\phi = \frac{\pi}{2}\right) = \frac{U_1}{N_S}\left(a_0^\dagger a_0^\dagger a_1 a_{-1} + a_1^\dagger a_{-1}^\dagger a_0 a_0\right) + \frac{U_0}{N_S}\left(N_0N_1 + N_0N_{-1} + N_1N_{-1}\right), \tag{5.20}$$

$$\begin{aligned}\mathcal{H}_{\mathrm{RWA}}\left(\phi = \frac{3\pi}{2}\right) &= -\frac{U_1}{N_S}\left(a_0^\dagger a_0^\dagger a_1 a_{-1} + a_1^\dagger a_{-1}^\dagger a_0 a_0\right) \\ &+ \frac{U_0}{N_S}\left(N_0N_1 + N_0N_{-1} + N_1N_{-1}\right). \end{aligned} \tag{5.21}$$

As we can see, two different phases ϕ can lead to opposite relative signs between U_0 and U_1. Here, we recover exactly the Hamiltonian of Eq. 5.2 in the case $\phi = 3\pi/2$. We saw in the previous section (figures 5.2b and 5.5) that the relative sign did not matter for the population transfer, but it plays an important role for the variance of J^x. Therefore we expect that changing ϕ will not affect the population transfer from the mode 0 to the modes ± 1, but it will drastically affect the value of $\langle (J^x)^2_{\max} \rangle$. This is confirmed in figure 5.12, both with the time dependent Hamiltonian (dashed lines) and the time-independent Hamiltonian -after making the RWA (solid lines).

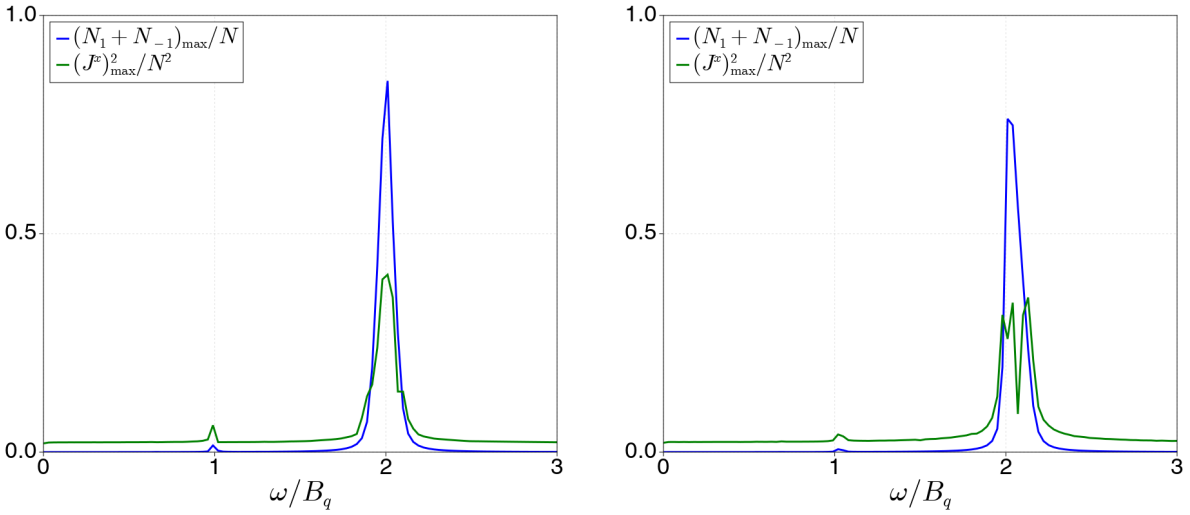

(a) $U_0 = 0.01U_1$ (b) $U_0 = 0.75U_1$

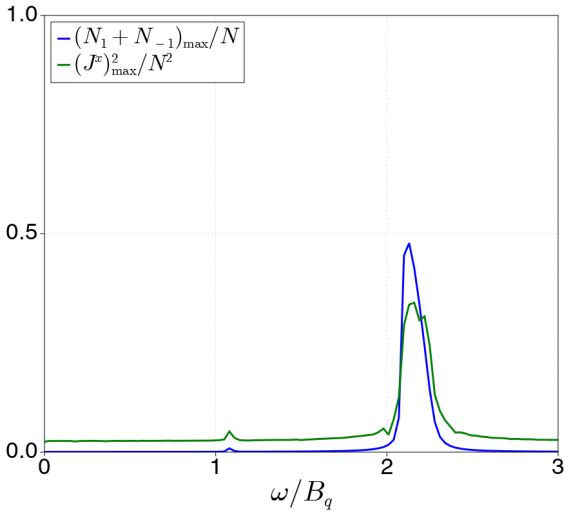

(c) $U_0 = 2U_1$

Figure 5.11: Maximum population transfer and variance of J^x for different drive frequencies ω. For all the figures, we have taken $N = 50$, $B_q = 20U_1$ and $\phi = 0$.

Figure 5.13 shows a comparison between results with and without the RWA, validating the latter approximation when $B_q \gg U$. As we can see, in the limit of large B_q, we do have the same expectation value for the population transfer $(N_1 + N_{-1})/N$ and for the variance of J^x, whereas for intermediate B_q, we still can see some oscillations due to the not so fast oscillation present in the RF Hamiltonian.

Finally, we implemented the RF and RWA Hamiltonians for the Gaussian ansatz, and compared the result obtained with our previous results from ED. We show the results of such comparison in figure 5.14. As we can see, similarly to the ED case, we have a perfect agreement between the RWA and RF Hamiltonian for the Gaussian ansatz for a very large $B_q = 100U_1$. Moreover, as in the spinor case, we see that the Gaussian Ansatz perfectly reproduces ED results at early times, and it gives a good estimation of the maximum value of $\langle (J^x) \rangle / N^2$ reached during the time evolution. This Ansatz will be really interesting in order to study the case with more modes in the system, for which we will not be able to rely on ED results anymore. Indeed, when

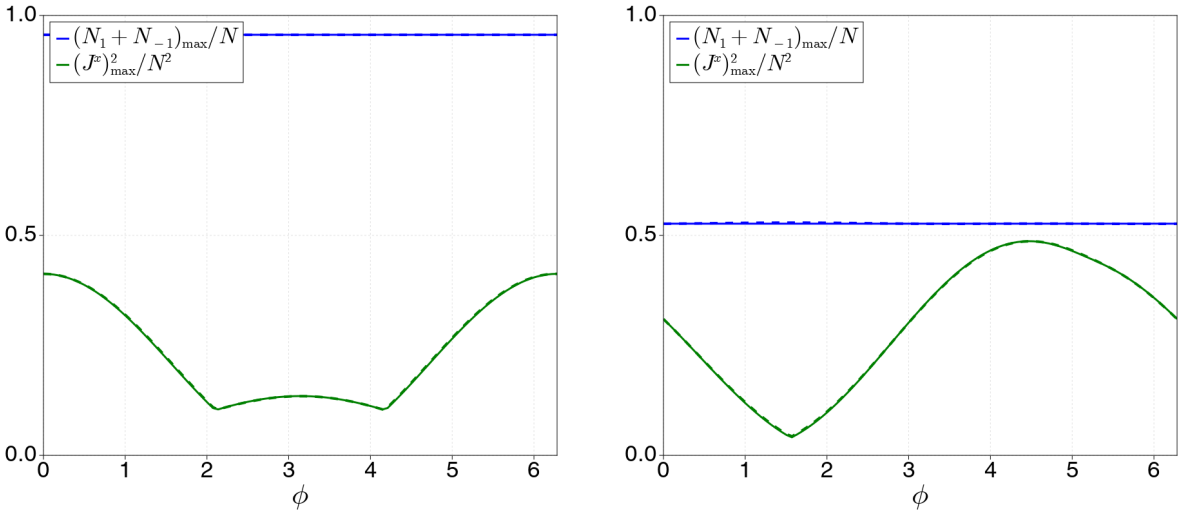

(a) $U_0 = 0$ (b) $U_0 = 0.75U_1$

Figure 5.12: Maximum population transfer and variance of J^x for different initial phase ϕ. The dashed lines corresponds to the evolution with time-dependent Hamiltonian in the rotating frame $\mathcal{H}_{\text{RF}}$, while the solid lines correspond to the time independent Hamiltonian after the RWA, $\mathcal{H}_{\text{RWA}}$. For both figures, we have taken $N = 50$ and $B_q = 50U_1$.

studying correlations in momentum space, collisions can lead to leakage into other momentum modes - even if we couple preferentially to two modes via the Faraday instability. We will discuss more in details the generalisation to M momentum modes in subsection 5.2.4.

5.2.3 Potential metrological application to force sensing

Squeezing in momentum space can be used to measure inertial forces with an enhanced precision, with respect to independent atoms, as it was possible to measure a magnetic field with higher precision using spin-squeezed states. Indeed, we consider in 1D an inertial force that couples to the atoms via the following Hamiltonian:

$$\mathcal{H}_F = -F \sum_r V_r n_r \tag{5.22}$$

with V_r the local potential associated to the force at position r and n_r the number of atoms at position r. Expressing this Hamiltonian in momentum space, we obtain:

$$\mathcal{H}_F = -\frac{F}{\sqrt{N_S}} \sum_{k,q} V_{k-q} a_k^\dagger a_q \tag{5.23}$$

where V_q is the Fourier transform of V_r at momentum q. In the case of only three momentum modes $k = 0, \pm k_0$, it can be rewritten, up to constant terms, as:

$$\begin{aligned}\mathcal{H}_F &= -\frac{F}{\sqrt{2N_S}} \left[|V_{k_0}| \left(e^{i\phi} J^+ + e^{-i\phi} J^- \right) + V_{2k_0}^* a_{-1}^\dagger a_1 + V_{2k_0} a_1^\dagger a_{-1} \right] \\ &= -\frac{F}{\sqrt{2N_S}} \left[2|V_{k_0}| \left(\cos(\phi) J^x - \sin(\phi) J^y \right) + V_{2k_0}^* a_{-1}^\dagger a_1 + V_{2k_0} a_1^\dagger a_{-1} \right]\end{aligned} \tag{5.24}$$

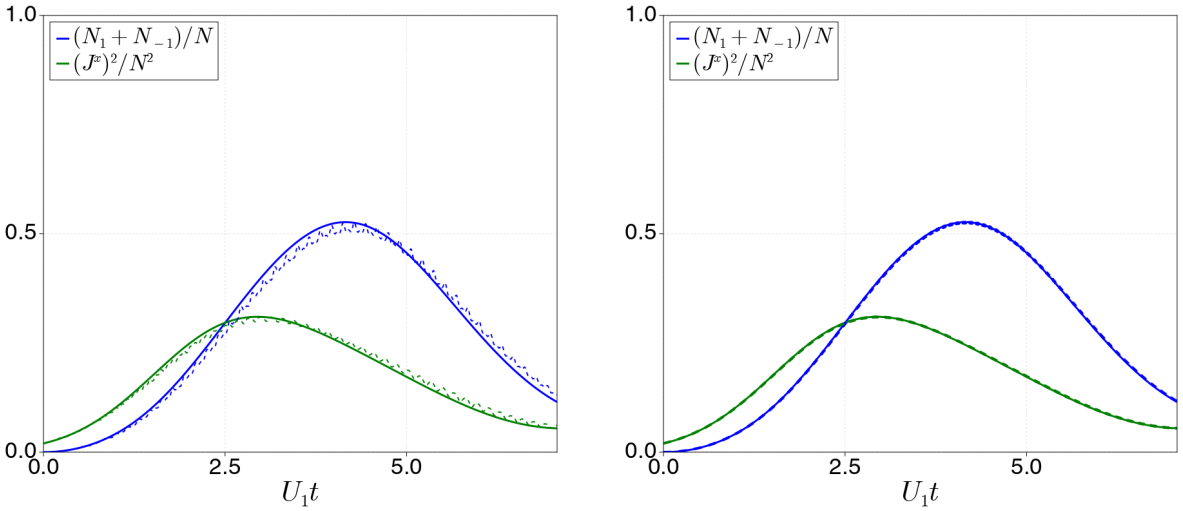

(a) $B = 20U_1$ (b) $B = 200U_1$

Figure 5.13: Time evolution of the population in the $k = \pm 1$ modes and of the variance of J^x for the time-dependent (dashed lines) and time-independent (solid lines) Hamiltonians. Here, we have taken $N = 50$, $U_1 = 1$, $U_0 = 0.75$, and $\phi = 0$.

with $V_{k_0} = |V_{k_0}|e^{i\phi}$. Assuming the terms $a_1^\dagger a_{-1}$ and $a_{-1}^\dagger a_1$ vanishes (as with the RWA approximation), we are left with a Hamiltonian that is proportional to $J^\phi = \cos(\phi) J^x - \sin(\phi) J^y$. From this, it is clear why we can apply the same metrological schemes as in the case of measuring a B field along an axis in the equatorial plane in the case of spinor condensates.

5.2.4 Generalisation to M modes

The first step towards the generalisation to M modes is to consider five modes, i.e. two additional modes which are not resonantly coupled to the condensate. We take into account the following modes : $-2k_0, -k_0, 0, k_0, 2k_0$. Similarly to the case with three modes, we assume that we have a large B_q that gives rise to off-resonant momentum-collision terms. Keeping the same notation as in subsection 5.2.1, we have the following Hamiltonian:

$$\mathcal{H} = \frac{U(t)}{N_S} \sum_{k,k',q} a_{k-q}^\dagger a_{k'+q}^\dagger a_k a_{k'} + B_q \sum_k k^2 N_k \tag{5.25}$$

with $k, k' \in \{0, \pm 1, \pm 2\}$. We consider again the case of time modulation of the interaction scattering length in order to have the same resonant collision process as before, namely $a_1^\dagger a_{-1}^\dagger a_0 a_0$ and $a_0^\dagger a_0^\dagger a_1 a_{-1}$. This again fixes the value of the modulation frequency to $\omega = 2B_q$. Moving to the same frame as in subsection 5.2.2, and performing the RWA, we obtain, up to constant terms:

$$\begin{aligned}\mathcal{H}_{RWA}(\phi) = &\frac{U_1}{iN_S}\left(a_0^\dagger a_0^\dagger a_1 a_{-1} e^{i\phi} + a_{-1}^\dagger a_{-1}^\dagger a_0 a_{-2} e^{i\phi} + a_1^\dagger a_1^\dagger a_0 a_2 e^{i\phi} + \text{h.c.}\right) \\ &+ \frac{U_0}{N_S} \sum_{k<k'} N_k N_{k'}.\end{aligned} \tag{5.26}$$

The first interesting result is that we now have other resonant collision processes, that send two atoms in the ± 1 mode to one in the ± 2 mode and the other in the 0 mode. In

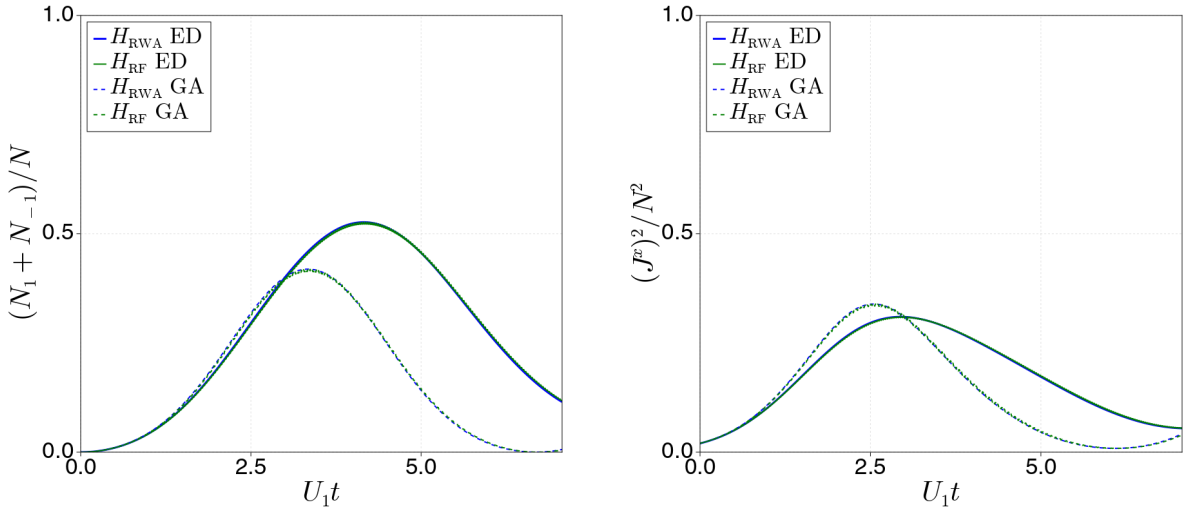

(a) $(N_1 + N_{-1})/N$ (b) $\langle (J^x) \rangle / N^2$

Figure 5.14: (a) time evolution of the population in the $k = \pm 1$ modes and (b) time evolution of the variance of J^x for the time-dependent RF (green lines) and time-independent RWA (blue lines) Hamiltonians. Here, we have taken $N = 50$, $U_1 = 1$, $U_0 = 0.75$, $B = 100$ and $\phi = 0$. Solid lines correspond to ED simulations, while dashed lines correspond to the GA results.

the case of many modes, it is easy to see that indeed we expect always a resonant coupling of the form $a^\dagger_{(n+1)k_0} a^\dagger_{(n-1)k_0} a_{nk_0} a_{nk_0}$ if we choose $\omega = 2B_q k_0^2$ - in order to have a resonant $a^\dagger_{k_0} a^\dagger_{-k_0} a_0 a_0$ momentum-exchange collision - and if we have a quadratic dispersion relation. This process could parasite the three-mode dynamics - i.e. Dicke squeezing for an effective $S = 1$ spin - described in the previous subsection; however because at early times there are only a few atoms in the $k \neq 0$ modes this process may be slow enough to observe three-mode dynamics at early times. Note that now we have 5 modes, which reduces drastically the atom numbers reachable with exact methods, and we will have to rely on Gaussian Ansatz to perform the numerical simulations for larger system sizes. We did not have the time to perform the numerical simulations in the case of 5 modes or more during this thesis, but this will be the subject of future work.

5.3 Conclusions

To conclude, we saw in this chapter that it was possible to generate highly entangled states - in the form of Dicke-squeezed states - when considering the dynamics of a spinor condensate in a single spatial mode with spin-exchange collisions. We compared the time evolution predicted by exact methods with that predicted by a Gaussian Ansatz and we found a good agreement between the two methods. We also investigated the metrological potential of Dicke-squeezed states, in particular their sensitivity to rotations and we found that it was possible to achieve the Heisenberg scaling with number of atoms for the sensitivity to rotations around any axis in the equatorial plane. Finally, we saw in the second section that it was possible to recover results similar to the Dicke-squeezing dynamics with a spinless time-dependent Hamiltonian even in the presence of a strong energy offset between the modes. This requires a periodic modulation of the scattering length - which leads to a modulation of the effective coupling

potential $U(t) = U_0/2 + U_1 \sin(\omega t + \phi)$. We determined that in order to reach the optimal squeezed state, we need to reach a ratio $U_0/U_1 = 0.75$. This corresponds to having a very strong modulation of the scattering length with respect to its mean value. This could be done by operating at the vicinity of a Feshbach resonance [118], around which it is possible to vary the scattering length by several order of magnitudes, and even changing its sign.

Conclusions

One of the main motivations of this thesis was to achieve a better understanding of the dynamics of quantum spin systems, in particular the build-up of correlations and entanglement in large-S spin systems, starting with a separable initial state. For this purpose, we developed new approximate schemes, namely an approximate separation of variables adapted to the large-S systems, as well as a Gaussian Ansatz (GA) and a Truncated Cumulant Expansion (TCE) for spin fluctuations.

In the case of the dipolar XXZ Hamiltonian for magnetic atoms, we were able to predict the existence of highly entangled states in the dynamics - in the form of highly squeezed states and cat-like states - in the case of only $N = 2$ spins, starting with a uniform or staggered coherent spin state in the xy plane. Thanks to the approximate separation of variables, we were able to extend this result to the case of very large systems sizes in 2D square lattices, in the case of a uniform initial state. In particular, we have proposed a realistic protocol to realize scalable spin squeezing, obeying the scaling of the OAT model for a sufficiently small quadratic Zeeman shift B_q. Hence our work paves the way for the realization of scalable multipartite entanglement in arrays of magnetic atoms (Cr, Er or Dy), representing a most promising platform to realize quantum simulation and quantum information processing with ensembles of qudits.

Finally, we studied the generation of other forms of entanglement - namely Dicke squeezing - in the case of atomic condensates. In particular, we showed that by modulating periodically in time the condensate scattering length - e.g. via a Feshbach resonance - it was possible to generate states in the dynamics that reach the Heisenberg scaling of sensitivity with respect to rotation angles. These results were partly known in the case of spin-1 condensates, for instance with ^{87}Rb atoms, and we generalized them to the case of spinless condensates by studying correlations in momentum space. The latter present a potential metrological interest, as squeezing in momentum space can be used to achieve a better sensitivity - w.r.t. independent atoms - when measuring inertial forces.

As a further direction, we shall investigate the general case with more than three different momentum modes. We have shown that in the case of more than three modes, there are other resonant momentum-collision processes, and it will be important to investigate how much they change the squeezing dynamics we observe in the three-mode case.

Another interesting future direction will be to implement alternative numerical methods to compare with our numerical results, and in particular the GDTWA, which can be very successful in the study of large-S spins. In a recent collaboration with the group of A. M. Rey and the group of B. Laburthe, we could test the predictions of the TCE approach versus GDTWA predictions and experimental results for bipartite correlation along quantization axis

for chromium atoms [81]. This pointed out the good agreement between the different numerical approaches for short times, as well as the fact that GDTWA is able to predict the correct structure of spin correlations at longer times.

Finally, we can consider further perspectives, and in particular:

- study itinerant spinful bosons / fermions with e.g. Gaussian Ansatz / Hartree-Fock approach, in order to investigate spin entanglement resulting from spin-changing collisions and dipolar interactions;
- study how to create giant dipolar spins with two condensates, and determine what entangled states can emerge and resist dipolar relaxation;

all this in the perspective of a quantum gas microscope which can measure spatially resolved spin populations.

Bibliography

[1] I. M. Georgescu, S. Ashhab, and F. Nori, "Quantum simulation," *Rev. Mod. Phys.*, vol. 86, pp. 153–185, Mar 2014.

[2] R. Horodecki, P. Horodecki, M. Horodecki, and K. Horodecki, "Quantum entanglement," *Rev. Mod. Phys.*, vol. 81, pp. 865–942, Jun 2009.

[3] O. Gühne and G. Tóth, "Entanglement detection," *Physics Reports*, vol. 474, pp. 1–75, Apr. 2009.

[4] V. Giovannetti, S. Lloyd, and L. Maccone, "Advances in quantum metrology," *Nature Photonics*, vol. 5, pp. 222–229, Apr. 2011.

[5] G. Tóth and I. Apellaniz, "Quantum metrology from a quantum information science perspective," *Journal of Physics A: Mathematical and Theoretical*, vol. 47, p. 424006, Oct. 2014.

[6] C. W. Helstrom, "Quantum detection and estimation theory," *J Stat Phys*, vol. 1, no. 2, pp. 231–252, 1969.

[7] L. D'Alessio, Y. Kafri, A. Polkovnikov, and M. Rigol, "From quantum chaos and eigenstate thermalization to statistical mechanics and thermodynamics," *Advances in Physics*, vol. 65, pp. 239–362, May 2016.

[8] M. Srednicki, "The approach to thermal equilibrium in quantized chaotic systems," *Journal of Physics A: Mathematical and General*, vol. 32, pp. 1163–1175, Feb. 1999.

[9] J. Eisert, M. Cramer, and M. B. Plenio, "Colloquium: Area laws for the entanglement entropy," *Rev. Mod. Phys.*, vol. 82, pp. 277–306, Feb 2010.

[10] J. M. Deutsch, H. Li, and A. Sharma, "Microscopic origin of thermodynamic entropy in isolated systems," *Phys. Rev. E*, vol. 87, p. 042135, Apr 2013.

[11] S. Moudgalya, B. A. Bernevig, and N. Regnault, "Quantum many-body scars and Hilbert space fragmentation: a review of exact results," *Reports on Progress in Physics*, vol. 85, p. 086501, Aug. 2022.

[12] P. Sala, T. Rakovszky, R. Verresen, M. Knap, and F. Pollmann, "Ergodicity Breaking Arising from Hilbert Space Fragmentation in Dipole-Conserving Hamiltonians," *Physical Review X*, vol. 10, p. 011047, Feb. 2020.

[13] D. A. Huse, R. Nandkishore, and V. Oganesyan, "Phenomenology of fully many-body-localized systems," *Physical Review B*, vol. 90, p. 174202, Nov. 2014.

[14] V. Alba, "Eigenstate thermalization hypothesis and integrability in quantum spin chains," *Phys. Rev. B*, vol. 91, p. 155123, Apr 2015.

[15] A. Weiße and H. Fehske, "Exact Diagonalization Techniques," in *Computational Many-Particle Physics* (H. Fehske, R. Schneider, and A. Weiße, eds.), vol. 739, pp. 529–544, Berlin, Heidelberg: Springer Berlin Heidelberg, 2008. Series Title: Lecture Notes in Physics.

[16] C. Lanczos, "An iteration method for the solution of the eigenvalue problem of linear differential and integral operators," *J. Res. Natl. Bur. Stand. B*, vol. 45, pp. 255–282, 1950.

[17] J. Cullum and R. A. Willoughby, "A survey of Lanczos procedures for very large real 'symmetric' eigenvalue problems," *Journal of Computational and Applied Mathematics*, vol. 12-13, pp. 37–60, May 1985.

[18] H. A. M. Leymann, A. Foerster, and J. Wiersig, "Expectation value based equation-of-motion approach for open quantum systems: A general formalism," *Phys. Rev. B*, vol. 89, p. 085308, Feb 2014.

[19] R. Schack and A. Schenzle, "Moment hierarchies and cumulants in quantum optics," *Phys. Rev. A*, vol. 41, pp. 3847–3852, Apr 1990.

[20] D. Plankensteiner, C. Hotter, and H. Ritsch, "QuantumCumulants.jl: A Julia framework for generalized mean-field equations in open quantum systems," *Quantum*, vol. 6, p. 617, Jan. 2022.

[21] W. Verstraelen, D. Huybrechts, T. Roscilde, and M. Wouters, "Quantum and classical correlations in open quantum spin lattices via truncated-cumulant trajectories," *PRX Quantum*, vol. 4, p. 030304, Jul 2023.

[22] V. E. Colussi, H. Kurkjian, M. Van Regemortel, S. Musolino, J. van de Kraats, M. Wouters, and S. J. J. M. F. Kokkelmans, "Cumulant theory of the unitary bose gas: Prethermal and efimovian dynamics," *Phys. Rev. A*, vol. 102, p. 063314, Dec 2020.

[23] F. Becca and S. Sorella, *Quantum Monte Carlo Approaches for Correlated Systems*. Cambridge University Press, 1 ed., Nov. 2017.

[24] J. Gubernatis, N. Kawashima, and P. Werner, *Quantum Monte Carlo Methods: Algorithms for Lattice Models*. Cambridge University Press, 1 ed., Jan. 2016.

[25] A. W. Sandvik, A. Avella, and F. Mancini, "Computational Studies of Quantum Spin Systems," (Vietri sul Mare, (Italy)), pp. 135–338, 2010.

[26] F. Bloch, "Zur Theorie des Ferromagnetismus," *Zeitschrift für Physik*, vol. 61, pp. 206–219, Mar. 1930.

[27] J. C. Slater, "Cohesion in monovalent metals," *Phys. Rev.*, vol. 35, pp. 509–529, Mar 1930.

[28] R. Kubo, "The spin-wave theory as a variational method and its application to antiferromagnetism," *Rev. Mod. Phys.*, vol. 25, pp. 344–351, Jan 1953.

[29] T. Shi, E. Demler, and J. I. Cirac, "Variational approach for many-body systems at finite temperature," *Phys. Rev. Lett.*, vol. 125, p. 180602, Oct 2020.

[30] J. I. Cirac, D. Pérez-García, N. Schuch, and F. Verstraete, "Matrix product states and projected entangled pair states: Concepts, symmetries, theorems," *Rev. Mod. Phys.*, vol. 93, p. 045003, Dec 2021.

[31] S. R. Muleady, M. Yang, S. R. White, and A. M. Rey, "Validating phase-space methods with tensor networks in two-dimensional spin models with power-law interactions," *Phys. Rev. Lett.*, vol. 131, p. 150401, Oct 2023.

[32] B. Zhu, A. M. Rey, and J. Schachenmayer, "A generalized phase space approach for solving quantum spin dynamics," *New Journal of Physics*, vol. 21, p. 082001, Aug. 2019.

[33] M. A. Nielsen and I. L. Chuang, *Quantum Computation and Quantum Information: 10th Anniversary Edition*. Cambridge University Press, 1 ed., June 2012.

[34] Y. Wang, Z. Hu, B. C. Sanders, and S. Kais, "Qudits and High-Dimensional Quantum Computing," *Frontiers in Physics*, vol. 8, p. 589504, Nov. 2020.

[35] M. Erhard, M. Krenn, and A. Zeilinger, "Advances in high-dimensional quantum entanglement," *Nature Reviews Physics*, vol. 2, pp. 365–381, June 2020.

[36] E. Moreno-Pineda, C. Godfrin, F. Balestro, W. Wernsdorfer, and M. Ruben, "Molecular spin qudits for quantum algorithms," *Chemical Society Reviews*, vol. 47, no. 2, pp. 501–513, 2018.

[37] L. Chomaz, I. Ferrier-Barbut, F. Ferlaino, B. Laburthe-Tolra, B. L. Lev, and T. Pfau, "Dipolar physics: a review of experiments with magnetic quantum gases," *Reports on Progress in Physics*, vol. 86, p. 026401, Feb. 2023.

[38] L. Pezzè, A. Smerzi, M. K. Oberthaler, R. Schmied, and P. Treutlein, "Quantum metrology with nonclassical states of atomic ensembles," *Reviews of Modern Physics*, vol. 90, p. 035005, Sept. 2018.

[39] R. H. Dicke, "Coherence in spontaneous radiation processes," *Phys. Rev.*, vol. 93, pp. 99–110, Jan 1954.

[40] J. M. Radcliffe, "Some properties of coherent spin states," *J. Phys. A: Gen. Phys.*, vol. 4, no. 3, pp. 313–323, 1971.

[41] T. Chalopin, "Quantum-enhanced sensing and synthetic landau levels with ultracold dysprosium atoms," 2019.

[42] J. P. Dowling, G. S. Agarwal, and W. P. Schleich, "Wigner distribution of a general angular-momentum state: Applications to a collection of two-level atoms," *Phys. Rev. A*, vol. 49, pp. 4101–4109, May 1994.

[43] K. Husimi, "Some formal properties of the density matrix," *Proceedings of the Physico-Mathematical Society of Japan. 3rd Series*, vol. 22, no. 4, pp. 264–314, 1940.

[44] D. J. Wineland, J. J. Bollinger, W. M. Itano, and D. J. Heinzen, "Squeezed atomic states and projection noise in spectroscopy," *Phys. Rev. A*, vol. 50, no. 1, pp. 67–88, 1994.

[45] D. J. Wineland, J. J. Bollinger, W. M. Itano, F. L. Moore, and D. J. Heinzen, "Spin squeezing and reduced quantum noise in spectroscopy," *Phys. Rev. A*, vol. 46, no. 11, pp. R6797–R6800, 1992. Publisher: American Physical Society.

[46] G. S. Agarwal and R. R. Puri, "Atomic states with spectroscopic squeezing," *Phys. Rev. A*, vol. 49, pp. 4968–4971, Jun 1994.

[47] M. Hillery and L. Mlodinow, "Interferometers and minimum-uncertainty states," *Phys. Rev. A*, vol. 48, pp. 1548–1558, Aug 1993.

[48] A. S. Sørensen and K. Mølmer, "Entanglement and extreme spin squeezing," *Phys. Rev. Lett.*, vol. 86, pp. 4431–4434, May 2001.

[49] D. F. Walls, "Squeezed states of light," *Nature*, vol. 306, pp. 141–146, Nov. 1983.

[50] J. Schwinger, "On angular momentum," 1 1952.

[51] T. Holstein and H. Primakoff, "Field dependence of the intrinsic domain magnetization of a ferromagnet," *Phys. Rev.*, vol. 58, no. 12, pp. 1098–1113, 1940.

[52] M. Kitagawa and M. Ueda, "Squeezed spin states," *Phys. Rev. A*, vol. 47, pp. 5138–5143, Jun 1993.

[53] C. K. Law, H. T. Ng, and P. T. Leung, "Coherent control of spin squeezing," *Phys. Rev. A*, vol. 63, p. 055601, Apr 2001.

[54] G.-R. Jin and S. W. Kim, "Storage of spin squeezing in a two-component bose-einstein condensate," *Phys. Rev. Lett.*, vol. 99, p. 170405, Oct 2007.

[55] C. Gross, T. Zibold, E. Nicklas, J. Estève, and M. K. Oberthaler, "Nonlinear atom interferometer surpasses classical precision limit," *Nature*, vol. 464, pp. 1165–1169, Apr. 2010.

[56] M. F. Riedel, P. Böhi, Y. Li, T. W. Hänsch, A. Sinatra, and P. Treutlein, "Atom-chip-based generation of entanglement for quantum metrology," *Nature*, vol. 464, pp. 1170–1173, Apr. 2010.

[57] R. Schmied, J.-D. Bancal, B. Allard, M. Fadel, V. Scarani, P. Treutlein, and N. Sangouard, "Bell correlations in a Bose-Einstein condensate," *Science*, vol. 352, pp. 441–444, Apr. 2016.

[58] M. Fadel, T. Zibold, B. Décamps, and P. Treutlein, "Spatial entanglement patterns and Einstein-Podolsky-Rosen steering in Bose-Einstein condensates," *Science*, vol. 360, pp. 409–413, Apr. 2018.

[59] A. S. Sørensen and K. Mølmer, "Entangling atoms in bad cavities," *Phys. Rev. A*, vol. 66, p. 022314, Aug 2002.

[60] I. D. Leroux, M. H. Schleier-Smith, and V. Vuletić, "Implementation of cavity squeezing of a collective atomic spin," *Phys. Rev. Lett.*, vol. 104, p. 073602, Feb 2010.

[61] Z. Li, B. Braverman, S. Colombo, C. Shu, A. Kawasaki, A. F. Adiyatullin, E. Pedrozo-Peñafiel, E. Mendez, and V. Vuletić, "Collective spin-light and light-mediated spin-spin interactions in an optical cavity," *PRX Quantum*, vol. 3, p. 020308, Apr 2022.

[62] O. Hosten, N. J. Engelsen, R. Krishnakumar, and M. A. Kasevich, "Measurement noise 100 times lower than the quantum-projection limit using entangled atoms," *Nature*, vol. 529, pp. 505–508, Jan. 2016.

[63] C. Song, K. Xu, H. Li, Y.-R. Zhang, X. Zhang, W. Liu, Q. Guo, Z. Wang, W. Ren, J. Hao, H. Feng, H. Fan, D. Zheng, D.-W. Wang, H. Wang, and S.-Y. Zhu, "Generation of multicomponent atomic schrödinger cat states of up to 20 qubits," *Science*, vol. 365, no. 6453, pp. 574–577, 2019.

[64] D. Kajtoch and E. Witkowska, "Quantum dynamics generated by the two-axis counter-twisting hamiltonian," *Phys. Rev. A*, vol. 92, p. 013623, Jul 2015.

[65] G. Vitagliano, I. Apellaniz, I. n. L. Egusquiza, and G. Tóth, "Spin squeezing and entanglement for an arbitrary spin," *Phys. Rev. A*, vol. 89, p. 032307, Mar 2014.

[66] B. Lücke, J. Peise, G. Vitagliano, J. Arlt, L. Santos, G. Tóth, and C. Klempt, "Detecting multiparticle entanglement of dicke states," *Phys. Rev. Lett.*, vol. 112, p. 155304, Apr 2014.

[67] A. Abragam, *The Principles of Nuclear Magnetism*. Clarendon Press, 1961.

[68] N. F. Mott, "Metal-insulator transition," *Rev. Mod. Phys.*, vol. 40, pp. 677–683, Oct 1968.

[69] A. Patscheider, B. Zhu, L. Chomaz, D. Petter, S. Baier, A.-M. Rey, F. Ferlaino, and M. J. Mark, "Controlling dipolar exchange interactions in a dense three-dimensional array of large-spin fermions," *Phys. Rev. Res.*, vol. 2, p. 023050, Apr 2020.

[70] A. de Paz, A. Sharma, A. Chotia, E. Maréchal, J. H. Huckans, P. Pedri, L. Santos, O. Gorceix, L. Vernac, and B. Laburthe-Tolra, "Nonequilibrium quantum magnetism in a dipolar lattice gas," *Phys. Rev. Lett.*, vol. 111, no. 18, p. 185305, 2013. Publisher: American Physical Society.

[71] S. Lepoutre, J. Schachenmayer, L. Gabardos, B. Zhu, B. Naylor, E. Maréchal, O. Gorceix, A. M. Rey, L. Vernac, and B. Laburthe-Tolra, "Out-of-equilibrium quantum magnetism and thermalization in a spin-3 many-body dipolar lattice system," *Nat Commun*, vol. 10, no. 1, p. 1714, 2019.

[72] L. Gabardos, B. Zhu, S. Lepoutre, A. M. Rey, B. Laburthe-Tolra, and L. Vernac, "Relaxation of the collective magnetization of a dense 3d array of interacting dipolar $s = 3$ atoms," *Phys. Rev. Lett.*, vol. 125, p. 143401, Sep 2020.

[73] Y. A. Alaoui, B. Zhu, S. R. Muleady, W. Dubosclard, T. Roscilde, A. M. Rey, B. Laburthe-Tolra, and L. Vernac, "Measuring correlations from the collective spin fluctuations of a large ensemble of lattice-trapped dipolar spin-3 atoms," *Phys. Rev. Lett.*, vol. 129, p. 023401, Jul 2022.

[74] T. Chalopin, C. Bouazza, A. Evrard, V. Makhalov, D. Dreon, J. Dalibard, L. A. Sidorenkov, and S. Nascimbene, "Quantum-enhanced sensing using non-classical spin states of a highly magnetic atom," *Nature Communications*, vol. 9, no. 1, p. 4955, 2018.

[75] A. Evrard, V. Makhalov, T. Chalopin, L. A. Sidorenkov, J. Dalibard, R. Lopes, and S. Nascimbene, "Enhanced magnetic sensitivity with non-gaussian quantum fluctuations," *Phys. Rev. Lett.*, vol. 122, p. 173601, May 2019.

[76] T. Satoor, A. Fabre, J.-B. Bouhiron, A. Evrard, R. Lopes, and S. Nascimbene, "Partitioning dysprosium's electronic spin to reveal entanglement in nonclassical states," *Phys. Rev. Res.*, vol. 3, p. 043001, Oct 2021.

[77] C. Bouazza, "Ultracold dysprosium gas in optical dipole traps: control of interactions between highly magnetic atoms," 2018.

[78] W. S. Bakr, J. I. Gillen, A. Peng, S. Fölling, and M. Greiner, "A quantum gas microscope for detecting single atoms in a hubbard-regime optical lattice," *Nature*, vol. 462, no. 7269, pp. 74–77, 2009.

[79] E. Haller, J. Hudson, A. Kelly, D. A. Cotta, B. Peaudecerf, G. D. Bruce, and S. Kuhr, "Single-atom imaging of fermions in a quantum-gas microscope," *Nature Physics*, vol. 11, no. 9, pp. 738–742, 2015.

[80] L. Su, A. Douglas, M. Szurek, R. Groth, S. F. Ozturk, A. Krahn, A. H. Hébert, G. A. Phelps, S. Ebadi, S. Dickerson, F. Ferlaino, O. Marković, and M. Greiner, "Dipolar quantum solids emerging in a Hubbard quantum simulator," *Nature*, vol. 622, pp. 724–729, Oct. 2023.

[81] Y. A. Alaoui, S. R. Muleady, E. Chaparro, Y. Trifa, A. M. Rey, T. Roscilde, B. Laburthe-Tolra, and L. Vernac, "Measuring bipartite spin correlations of lattice-trapped dipolar atoms," 2024.

[82] A. Browaeys, D. Barredo, and T. Lahaye, "Experimental investigations of dipole–dipole interactions between a few Rydberg atoms," *Journal of Physics B: Atomic, Molecular and Optical Physics*, vol. 49, p. 152001, Aug. 2016.

[83] S. Weber, C. Tresp, H. Menke, A. Urvoy, O. Firstenberg, H. P. Büchler, and S. Hofferberth, "Calculation of Rydberg interaction potentials," *Journal of Physics B: Atomic, Molecular and Optical Physics*, vol. 50, p. 133001, July 2017.

[84] A. Browaeys and T. Lahaye, "Many-body physics with individually controlled Rydberg atoms," *Nature Physics*, vol. 16, pp. 132–142, Feb. 2020.

[85] H. Labuhn, D. Barredo, S. Ravets, S. De Léséleuc, T. Macrì, T. Lahaye, and A. Browaeys, "Tunable two-dimensional arrays of single Rydberg atoms for realizing quantum Ising models," *Nature*, vol. 534, pp. 667–670, June 2016.

[86] H. Bernien, S. Schwartz, A. Keesling, H. Levine, A. Omran, H. Pichler, S. Choi, A. S. Zibrov, M. Endres, M. Greiner, V. Vuletić, and M. D. Lukin, "Probing many-body dynamics on a 51-atom quantum simulator," *Nature*, vol. 551, pp. 579–584, Nov. 2017.

[87] J. Zeiher, J.-y. Choi, A. Rubio-Abadal, T. Pohl, R. Van Bijnen, I. Bloch, and C. Gross, "Coherent Many-Body Spin Dynamics in a Long-Range Interacting Ising Chain," *Physical Review X*, vol. 7, p. 041063, Dec. 2017.

[88] D. Barredo, H. Labuhn, S. Ravets, T. Lahaye, A. Browaeys, and C. S. Adams, "Coherent Excitation Transfer in a Spin Chain of Three Rydberg Atoms," *Physical Review Letters*, vol. 114, p. 113002, Mar. 2015.

[89] S. De Léséleuc, V. Lienhard, P. Scholl, D. Barredo, S. Weber, N. Lang, H. P. Büchler, T. Lahaye, and A. Browaeys, "Observation of a symmetry-protected topological phase of interacting bosons with Rydberg atoms," *Science*, vol. 365, pp. 775–780, Aug. 2019.

[90] P. Scholl, H. J. Williams, G. Bornet, F. Wallner, D. Barredo, L. Henriet, A. Signoles, C. Hainaut, T. Franz, S. Geier, A. Tebben, A. Salzinger, G. Zürn, T. Lahaye, M. Weidemüller, and A. Browaeys, "Microwave engineering of programmable xxz hamiltonians in arrays of rydberg atoms," *PRX Quantum*, vol. 3, p. 020303, Apr 2022.

[91] I. Cohen, P. Richerme, Z.-X. Gong, C. Monroe, and A. Retzker, "Simulating the haldane phase in trapped-ion spins using optical fields," *Phys. Rev. A*, vol. 92, p. 012334, Jul 2015.

[92] C. Monroe, W. C. Campbell, L.-M. Duan, Z.-X. Gong, A. V. Gorshkov, P. W. Hess, R. Islam, K. Kim, N. M. Linke, G. Pagano, P. Richerme, C. Senko, and N. Y. Yao, "Programmable quantum simulations of spin systems with trapped ions," *Rev. Mod. Phys.*, vol. 93, p. 025001, Apr 2021.

[93] B. Yan, S. A. Moses, B. Gadway, J. P. Covey, K. R. A. Hazzard, A. M. Rey, D. S. Jin, and J. Ye, "Observation of dipolar spin-exchange interactions with lattice-confined polar molecules," *Nature*, vol. 501, pp. 521–525, Sept. 2013.

[94] H. Zou, E. Zhao, and W. V. Liu, "Frustrated Magnetism of Dipolar Molecules on a Square Optical Lattice: Prediction of a Quantum Paramagnetic Ground State," *Physical Review Letters*, vol. 119, p. 050401, July 2017.

[95] N. Y. Yao, M. P. Zaletel, D. M. Stamper-Kurn, and A. Vishwanath, "A quantum dipolar spin liquid," *Nature Physics*, vol. 14, pp. 405–410, Apr. 2018.

[96] G. Vitagliano, P. Hyllus, I. n. L. Egusquiza, and G. Tóth, "Spin squeezing inequalities for arbitrary spin," *Phys. Rev. Lett.*, vol. 107, p. 240502, Dec 2011.

[97] S. Hensler, J. Werner, A. Griesmaier, P. Schmidt, A. Görlitz, T. Pfau, S. Giovanazzi, and K. Rzażewski, "Dipolar relaxation in an ultra-cold gas of magnetically trapped chromium atoms," *Applied Physics B*, vol. 77, pp. 765–772, Dec. 2003.

[98] A. de Paz, B. Naylor, J. Huckans, A. Carrance, O. Gorceix, E. Maréchal, P. Pedri, B. Laburthe-Tolra, and L. Vernac, "Dipolar atomic spin ensembles in a double-well potential," *Phys. Rev. A*, vol. 90, p. 043607, Oct 2014.

[99] T. Roscilde, T. Comparin, and F. Mezzacapo, "Rotor/spin-wave theory for quantum spin models with u(1) symmetry," *Phys. Rev. B*, vol. 108, p. 155130, Oct 2023.

[100] T. Roscilde, T. Comparin, and F. Mezzacapo, "Entangling dynamics from effective rotor–spin-wave separation in u(1)-symmetric quantum spin models," *Phys. Rev. Lett.*, vol. 131, p. 160403, Oct 2023.

[101] D. Peter, S. Müller, S. Wessel, and H. P. Büchler, "Anomalous behavior of spin systems with dipolar interactions," *Phys. Rev. Lett.*, vol. 109, p. 025303, Jul 2012.

[102] P. C. Hohenberg, "Existence of long-range order in one and two dimensions," *Phys. Rev.*, vol. 158, pp. 383–386, Jun 1967.

[103] N. D. Mermin and H. Wagner, "Absence of ferromagnetism or antiferromagnetism in one- or two-dimensional isotropic heisenberg models," *Phys. Rev. Lett.*, vol. 17, pp. 1133–1136, Nov 1966.

[104] M. Block, B. Ye, B. Roberts, S. Chern, W. Wu, Z. Wang, L. Pollet, E. J. Davis, B. I. Halperin, and N. Y. Yao, "A Universal Theory of Spin Squeezing," 2023. Publisher: [object Object] Version Number: 1.

[105] T. Comparin, F. Mezzacapo, and T. Roscilde, "Multipartite entangled states in dipolar quantum simulators," *Phys. Rev. Lett.*, vol. 129, p. 150503, Oct 2022.

[106] G. Bornet, G. Emperauger, C. Chen, B. Ye, M. Block, M. Bintz, J. A. Boyd, D. Barredo, T. Comparin, F. Mezzacapo, T. Roscilde, T. Lahaye, N. Y. Yao, and A. Browaeys, "Scalable spin squeezing in a dipolar Rydberg atom array," *Nature*, vol. 621, pp. 728–733, Sept. 2023.

[107] T. Roscilde, F. Caleca, A. Angelone, and F. Mezzacapo, "Scalable spin squeezing from critical slowing down in short-range interacting systems," 2024.

[108] Y.-Q. Zou, L.-N. Wu, Q. Liu, X.-Y. Luo, S.-F. Guo, J.-H. Cao, M. K. Tey, and L. You, "Beating the classical precision limit with spin-1 Dicke states of more than 10,000 atoms," *Proceedings of the National Academy of Sciences*, vol. 115, pp. 6381–6385, June 2018.

[109] X.-Y. Luo, Y.-Q. Zou, L.-N. Wu, Q. Liu, M.-F. Han, M. K. Tey, and L. You, "Deterministic entanglement generation from driving through quantum phase transitions," *Science*, vol. 355, pp. 620–623, Feb. 2017.

[110] C. Klempt, O. Topic, G. Gebreyesus, M. Scherer, T. Henninger, P. Hyllus, W. Ertmer, L. Santos, and J. J. Arlt, "Multiresonant Spinor Dynamics in a Bose-Einstein Condensate," *Physical Review Letters*, vol. 103, p. 195302, Nov. 2009.

[111] C. Klempt, O. Topic, G. Gebreyesus, M. Scherer, T. Henninger, P. Hyllus, W. Ertmer, L. Santos, and J. J. Arlt, "Parametric Amplification of Vacuum Fluctuations in a Spinor Condensate," *Physical Review Letters*, vol. 104, p. 195303, May 2010.

[112] Z. Zhang and L.-M. Duan, "Generation of Massive Entanglement through an Adiabatic Quantum Phase Transition in a Spinor Condensate," *Physical Review Letters*, vol. 111, p. 180401, Oct. 2013.

[113] M.-S. Chang, C. D. Hamley, M. D. Barrett, J. A. Sauer, K. M. Fortier, W. Zhang, L. You, and M. S. Chapman, "Observation of spinor dynamics in optically trapped ^{87}Rb bose-einstein condensates," *Phys. Rev. Lett.*, vol. 92, p. 140403, Apr 2004.

[114] T.-W. Mao, Q. Liu, X.-W. Li, J.-H. Cao, F. Chen, W.-X. Xu, M. K. Tey, Y.-X. Huang, and L. You, "Quantum-enhanced sensing by echoing spin-nematic squeezing in atomic Bose–Einstein condensate," *Nature Physics*, vol. 19, pp. 1585–1590, Nov. 2023.

[115] J. H. V. Nguyen, M. C. Tsatsos, D. Luo, A. U. J. Lode, G. D. Telles, V. S. Bagnato, and R. G. Hulet, "Parametric Excitation of a Bose-Einstein Condensate: From Faraday Waves to Granulation," *Physical Review X*, vol. 9, p. 011052, Mar. 2019.

[116] Z. Zhang, K.-X. Yao, L. Feng, J. Hu, and C. Chin, "Pattern formation in a driven Bose–Einstein condensate," *Nature Physics*, vol. 16, pp. 652–656, June 2020.

[117] I. Krešić, G. R. M. Robb, G.-L. Oppo, and T. Ackemann, "Generating multiparticle entangled states by self-organization of driven ultracold atoms," *Phys. Rev. Lett.*, vol. 131, p. 163602, Oct 2023.

[118] C. Chin, R. Grimm, P. Julienne, and E. Tiesinga, "Feshbach resonances in ultracold gases," *Rev. Mod. Phys.*, vol. 82, pp. 1225–1286, Apr 2010.

[119] O. F. Syljuåsen and A. W. Sandvik, "Quantum monte carlo with directed loops," *Phys. Rev. E*, vol. 66, p. 046701, Oct 2002.

[120] F. Alet, S. Wessel, and M. Troyer, "Generalized directed loop method for quantum monte carlo simulations," *Phys. Rev. E*, vol. 71, p. 036706, Mar 2005.

[121] N. Defenu, T. Donner, T. Macrì, G. Pagano, S. Ruffo, and A. Trombettoni, "Long-range interacting quantum systems," *Rev. Mod. Phys.*, vol. 95, p. 035002, Aug 2023.

Appendix A

TCE equations of motion

We give in this appendix the explicit equations of motions for the second order TCE method (assuming all the cumulants of order $n \geq 3$ remain zero at all times). We recall the expression of the spin operators in terms of the T operators:

$$S_i^z = \sum_m m T_i^{mm}, \quad S_i^+ = \sum_m \sqrt{S(S+1) - m(m+1)} T_i^{m+1,m}. \tag{A.1}$$

From now on, we will use the following notation:

$$C^+(m) = \sqrt{S(S+1) - m(m+1)}, \quad C^-(m) = \sqrt{S(S+1) - m(m-1)}. \tag{A.2}$$

The commutation relations of the $\{T_i^{mm'}\}$ are given by:

$$\left[T_i^{mm'}, T_j^{nn'}\right] = \delta_{ij}\left(\delta_{m'n} T_i^{mn'} - \delta_{n'm} T_i^{nm'}\right). \tag{A.3}$$

Therefore we get from the commutation relations with the Hamiltonian:

$$\begin{aligned}
\left[T_k^{mm'}, \mathcal{H}\right] &= \frac{1}{2}\sum_{i\neq j} V_{ij}\left(\left[T_k^{mm'}, S_i^z S_j^z\right] - \frac{1}{4}\left(\left[T_k^{mm'}, S_i^+ S_j^-\right] + \left[T_k^{mm'}, S_i^- S_j^+\right]\right)\right) \\
&+ \sum_i B_q \left[T_k^{mm'}, (S_i^z)^2\right] \\
&= \frac{1}{2}\sum_{i\neq j} V_{ij} \sum_{nl} nl \left[T_k^{mm'}, T_i^{nn} T_j^{ll}\right] + \sum_i B_q \sum_n n^2 \left[T_k^{mm'}, T_i^{nn}\right] \\
&- \frac{1}{8}\sum_{i\neq j} V_{ij} \sum_{n=-S}^{S-1} \sum_{l=-S+1}^{S} C^+(n) C^-(l) \left[T_k^{mm'}, T_i^{n+1,n} T_j^{l-1,l}\right] \\
&- \frac{1}{8}\sum_{i\neq j} V_{ij} \sum_{n=-S+1}^{S} \sum_{l=-S}^{S-1} C^-(n) C^+(l) \left[T_k^{mm'}, T_i^{n-1,n} T_j^{l+1,l}\right] \\
&= (m'-m) \sum_{j\neq k} \sum_l V_{kj} l T_k^{mm'} T_j^{ll} + B_q\left(m'^2 - m^2\right) T_k^{mm'} \\
&- \frac{1}{4}\sum_{j\neq k} V_{kj} \sum_{l=-S+1}^{S} C^-(l)\left[C^-(m') T_k^{m,m'-1} - C^+(m) T_k^{m+1,m'}\right] T_j^{l-1,l} \\
&- \frac{1}{4}\sum_{j\neq k} V_{jk} \sum_{l=-S}^{S-1} C^+(l)\left[C^+(m') T_k^{m,m'+1} - C^-(m) T_k^{m-1,m'}\right] T_j^{l+1,l}.
\end{aligned} \tag{A.4}$$

From this expression, we can immediately derive the equation for the time evolution of the $\{\langle T_k^{mm'}\rangle\}$:

$$\begin{aligned} i\hbar\frac{\mathrm{d}}{\mathrm{d}t}\langle T_k^{mm'}\rangle &= (m'-m)\sum_{j\neq k}\sum_l V_{kj}l\langle T_k^{mm'}T_j^{ll}\rangle + B_q\left(m'^2-m^2\right)\langle T_k^{mm'}\rangle \\ &- \frac{1}{4}\sum_{j\neq k}V_{kj}\sum_{l=-S+1}^{S}C^-(l)\left[C^-(m')\langle T_k^{m,m'-1}T_j^{l-1,l}\rangle - C^+(m)\langle T_k^{m+1,m'}T_j^{l-1,l}\rangle\right] \\ &- \frac{1}{4}\sum_{j\neq k}V_{jk}\sum_{l=-S}^{S-1}C^+(l)\left[C^+(m')\langle T_k^{m,m'+1}T_j^{l+1,l}\rangle - C^-(m)\langle T_k^{m-1,m'}T_j^{l+1,l}\rangle\right]. \end{aligned} \tag{A.5}$$

For the second-order terms, we use Leibniz rule to compute the commutator of $T_k^{mm'}T_g^{pp'}$ with $\mathcal{H}$, assuming $k\neq g$:

$$\left[T_k^{mm'}T_g^{pp'},\mathcal{H}\right] = \left[T_k^{mm'},\mathcal{H}\right]T_g^{pp'} + T_k^{mm'}\left[T_g^{pp'},\mathcal{H}\right]. \tag{A.6}$$

Using Eq. A.4, we get immediately the equation of motion for $\langle T_k^{mm'}T_g^{pp'}\rangle$:

$$\begin{aligned} i\hbar\frac{\mathrm{d}}{\mathrm{d}t}\langle T_k^{mm'}T_g^{pp'}\rangle &= (m'-m)\sum_{j\neq k}\sum_l V_{kj}l\langle T_k^{mm'}T_j^{ll}T_g^{pp'}\rangle + B_q\left(m'^2-m^2\right)\langle T_k^{mm'}T_g^{pp'}\rangle \\ &- \frac{1}{4}\sum_{j\neq k}V_{kj}\sum_{l=-S+1}^{S}C^-(l)\left[C^-(m')\langle T_k^{m,m'-1}T_j^{l-1,l}T_g^{pp'}\rangle - C^+(m)\langle T_k^{m+1,m'}T_j^{l-1,l}T_g^{pp'}\rangle\right] \\ &- \frac{1}{4}\sum_{j\neq k}V_{jk}\sum_{l=-S}^{S-1}C^+(l)\left[C^+(m')\langle T_k^{m,m'+1}T_j^{l+1,l}T_g^{pp'}\rangle - C^-(m)\langle T_k^{m-1,m'}T_j^{l+1,l}T_g^{pp'}\rangle\right] \\ &+ (p'-p)\sum_{j\neq g}\sum_l V_{gj}l\langle T_k^{mm'}T_g^{pp'}T_j^{ll}\rangle + B_q\left(p'^2-p^2\right)\langle T_k^{mm'}T_g^{pp'}\rangle \\ &- \frac{1}{4}\sum_{j\neq g}V_{gj}\sum_{l=-S+1}^{S}C^-(l)\left[C^-(p')\langle T_k^{m,m'}T_g^{p,p'-1}T_j^{l-1,l}\rangle - C^+(p)\langle T_k^{m,m'}T_g^{p+1,p'}T_j^{l-1,l}\rangle\right] \\ &- \frac{1}{4}\sum_{j\neq g}V_{jg}\sum_{l=-S}^{S-1}C^+(l)\left[C^+(p')\langle T_k^{m,m'}T_g^{p,p'+1}T_j^{l+1,l}\rangle - C^-(p)\langle T_k^{m,m'}T_g^{p-1,p'}T_j^{l+1,l}\rangle\right]. \end{aligned} \tag{A.7}$$

Finally, assuming that the third-order cumulants all vanish, we rewrite the third order correlation functions as:

$$\begin{aligned} \langle T_i^{ll'}T_j^{mm'}T_k^{nn'}\rangle &= \langle T_i^{ll'}T_j^{mm'}\rangle\langle T_k^{nn'}\rangle + \langle T_i^{ll'}\rangle\langle T_j^{mm'}T_k^{nn'}\rangle + \langle T_i^{ll'}T_k^{nn'}\rangle\langle T_j^{mm'}\rangle \\ &- 2\langle T_i^{ll'}\rangle\langle T_j^{mm'}\rangle\langle T_k^{nn'}\rangle \end{aligned} \tag{A.8}$$

for $i\neq j\neq k$, which indeed leads to a close set of equations of motion.

Appendix B

QMC and MF calculations for the phase diagram

B.1 Quantum Monte Carlo

The QMC simulations have been performed by T. Roscilde using the Stochastic Series Expansion approach with directed-loop updates [119]; this approach can be adapted to spin systems with arbitrary spin lengths S by using e.g. simple heat-bath transition probabilities dictating the directed-loop dynamics [120]. Simulations have been performed on $N = L \times L$ square lattices with periodic boundary conditions, and L ranging from 24 to 64. The critical temperature T_c^{FM} for the ferromagnetic-paramagnetic transition of the dipolar XXZ model has been estimated via the scaling of the correlation length ξ, which can be extracted from the structure factor:

$$S(\mathbf{q}) = \frac{1}{N} \sum_{ij} e^{i\mathbf{q}\cdot(\mathbf{r}_i - \mathbf{r}_j)} \langle S_i^x S_j^x \rangle \tag{B.1}$$

via the second-moment estimator

$$\xi = \frac{L}{2\pi} \sqrt{\frac{S(0,0)}{S(2\pi/L, 0)} - 1}. \tag{B.2}$$

This quantity is expected to exhibit the following scaling behaviour at the 2D dipolar transition

$$\xi \sim L F_\xi \left(|T - T_c^{\mathrm{FM}}| L^{1/\nu} \right) \tag{B.3}$$

where F_ξ is a universal scaling function, and $\nu = 1$ [121]. A representative scaling plot is shown in figure B.1, showing a very good collapse of the QMC data.

B.2 Mean-field approach

In order to perform the same computation with mean-field theory, we have to postulate that the thermal state of the system can be written as a separable state $\rho(T) = \otimes_{i=1}^{N} \rho_i(T)$, where

$$\rho_i(T) = \frac{\exp(-\beta \mathcal{H}_i)}{\mathrm{Tr}[\exp(-\beta \mathcal{H}_i)]} \ . \tag{B.4}$$

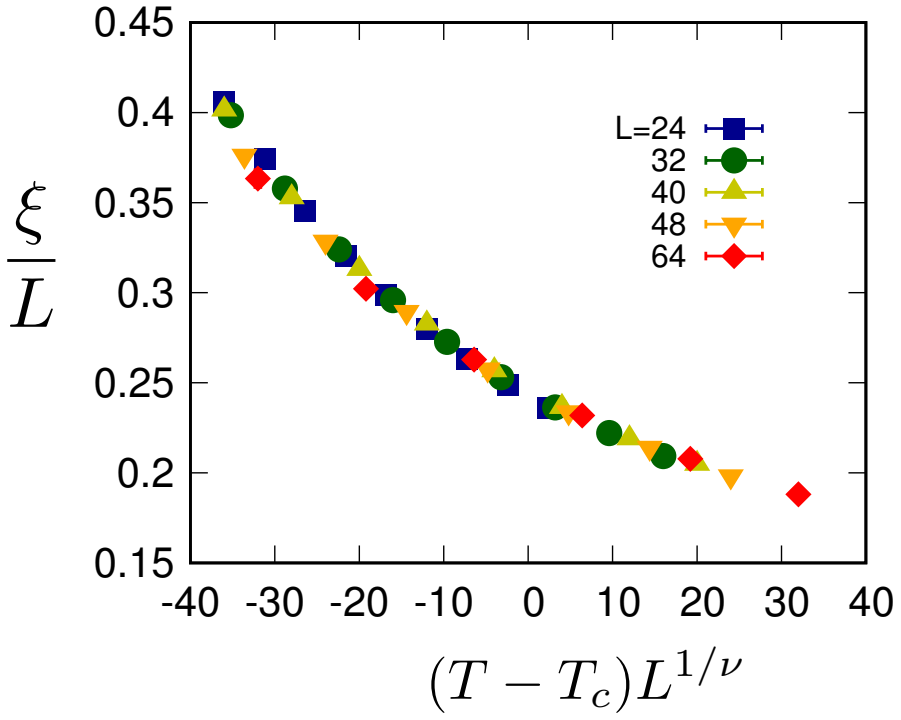

Figure B.1: Scaling plot of the correlation length at the ferromagnetic/paramagnetic transition for the 2D dipolar XXZ model with $S = 3$ and $B_q/J = 17$, using the critical exponent $\nu = 1$ and the critical temperature $T_c^{\mathrm{FM}} = 20.1J$. The data stem from unbiased QMC simulations.

$\mathcal{H}$ is the effective single-site Hamiltonian

$$\mathcal{H}_i = -\vec{H}_i \cdot (\vec{S}_i - \langle \vec{S}_i \rangle/2) + B_q (S_i^z)^2 \tag{B.5}$$

containing the effective self-consistent field

$$\begin{aligned} H_i^{x(y)} &= \frac{1}{2} \sum_j V_{ij} \langle S_j^{x(y)} \rangle \\ H_i^z &= -\sum_j V_{ij}^s \langle S_j^z \rangle \end{aligned} \tag{B.6}$$

where $\langle S_i^\mu \rangle = \mathrm{Tr}(S_i^\mu \rho_i)$. The equilibrium state of the system is then evaluated by self-consistently calculating the average spin $\langle \vec{S}_i \rangle$ until convergence, starting with a random initial state. In the particular case of $T = 0$, we take ρ_i as the ground state of the current MF Hamiltonian instead of a thermal distribution. In particular in the xy-ferromagnetic phase the average spin points in the xy plane; it vanishes in the paramagnetic phase (including the one at $T = 0$ for large B_q); while it is staggered along the z axis in the z-Néel phase obtained for $B_q < 0$. Note that we have introduced a staggered potential in the z component of the self-consistent field in order to be able to detect the AFM order along z at the single spin level.

Appendix C

Dicke squeezing with the Gaussian Ansatz

C.1 Equations of motion

We want to study the time evolution of a condensate of $S = 1$ spins, under the following Hamiltonian:

$$\mathcal{H} = U\left(a_0 a_0 a_1^\dagger a_{-1}^\dagger + \text{h.c.}\right) - U_0\left(a_0^\dagger a_0 a_1^\dagger a_1 + a_0^\dagger a_0 a_{-1}^\dagger a_{-1} + a_1^\dagger a_1 a_{-1}^\dagger a_{-1}\right). \tag{C.1}$$

For the Gaussian Ansatz, we assume that we can rewrite the bosonic operators as $a_0 = \phi_0 + \delta a_0$, $a_{\pm 1} = \delta a_{\pm 1}$ with $\phi_0 = \langle a_0 \rangle$ a scalar and $\langle \delta a_m \rangle = 0$. We then introduce the following two-point correlation functions for the bosonic operators:

$$G_{00} = \langle \delta a_0^\dagger \delta a_0 \rangle, \quad F_{00} = \langle \delta a_0 \delta a_0 \rangle, \quad G_{\pm 1 \pm 1} = \langle \delta a_{\pm 1}^\dagger \delta a_{\pm 1} \rangle, \quad F_{1-1} = \langle \delta a_1 \delta a_{-1} \rangle \tag{C.2}$$

and as the Hamiltonian conserves the magnetization, all the other two-point functions remain zero at all times. Moreover, since we have a symmetry between ± 1 modes, we will assume that we have $G_{11} = G_{-1-1}$ at all times. This gives rise to the following equations of motion:

$$i\frac{\mathrm{d}}{\mathrm{d}t}\phi_0 = \langle [a_0, \mathcal{H}] \rangle = 2U\bar{\phi}_0 F_{1-1} - 2U_0 \phi_0 G_{11} \tag{C.3}$$

$$i\frac{\mathrm{d}}{\mathrm{d}t}F_{00} = 2UF_{1-1} + 4UG_{00}F_{1-1} - 4U_0 F_{00} G_{11} \tag{C.4}$$

$$i\frac{\mathrm{d}}{\mathrm{d}t}F_{1-1} = U\left(\phi_0^2 + F_{00}\right)(1 + 2G_{11}) - U_0 F_{1-1}\left(1 + 2|\phi_0|^2 + 2G_{00} + 4G_{11}\right) \tag{C.5}$$

$$i\frac{\mathrm{d}}{\mathrm{d}t}G_{00} = 4Ui\mathrm{Im}\left(\bar{F}_{00}F_{1-1}\right) \tag{C.6}$$

$$i\frac{\mathrm{d}}{\mathrm{d}t}G_{11} = 2Ui\mathrm{Im}\left[\bar{F}_{1-1}\left(\phi_0^2 + F_{00}\right)\right]. \tag{C.7}$$

They form a set of classical coupled non-linear equations that we solve using a standard 4th-order Runge Kutta numerical scheme. For all the results presented in Chapter 5 using the GA approach, we checked the correctness of our equations by verifying the conservation of energy in time, which is given by:

$$\langle \mathcal{H} \rangle = 2U\mathrm{Re}\left(\left(\phi_0^2 + F_{00}\right)\bar{F}_{1-1}\right) - 2U_0\left(2\left(|\phi_0|^2 + G_{00}\right)G_{11} + G_{11}^2\right). \tag{C.8}$$

C.2 Phase uncertainty estimation with the Gaussian Ansatz

In order to estimate the uncertainty on the phase estimation with the Gaussian ansatz framework, we need to derive the expression of $\delta\theta^2$ in function of the previous correlation functions.

In particular, for the numerator of $\delta\theta^2$ we need to compute $\mathrm{Var}\left((J_\theta^z)^2\right)$ in the limit $\theta \to 0$ -as it give the best uncertainty. By definition, we have:

$$\mathrm{Var}\left((J_\theta^z)^2\right) = \langle (J_\theta^z)^4 \rangle - \langle (J_\theta^z)^2 \rangle^2 \tag{C.9}$$

with $J_\theta^z = \cos\theta J^z - \sin\theta J^y$. We first compute the square of J_θ^z:

$$(J_\theta^z)^2 = \cos^2\theta\,(J^z)^2 + \sin^2\theta\,(J^y)^2 - \cos\theta\sin\theta\,(J^zJ^y + J^yJ^z) \tag{C.10}$$

and we deduce its mean value by setting to zero all the terms that do no conserve the global magnetisation (here J^zJ^y and J^yJ^z):

$$\langle (J_\theta^z)^2 \rangle = \cos^2\theta \langle (J^z)^2 \rangle + \sin^2\theta \langle (J^y)^2 \rangle \tag{C.11}$$

Finally, we can take its square, and we obtain:

$$\langle (J_\theta^z)^2 \rangle^2 = \cos^4\theta \langle (J^z)^2 \rangle^2 + \sin^4\theta \langle (J^y)^2 \rangle^2 + 2\cos^2\theta\sin^2\theta \langle (J^z)^2 \rangle \langle (J^y)^2 \rangle. \tag{C.12}$$

Since we have only zero magnetisation states, all the powers of J^z remains zero during the dynamics which leads to the following expression:

$$\langle (J_\theta^z)^2 \rangle^2 = \sin^4\theta \langle (J^y)^2 \rangle^2. \tag{C.13}$$

We did check numerically that the the first, second and fourth powers of J^z remained zero at all times using the following expression:

$$\langle J^z \rangle = G_{11} - G_{11} = 0 \text{ by definition} \tag{C.14}$$

$$\langle (J^z)^2 \rangle = 2G_{11}^2 + 2G_{11} - 2|F_{1-1}|^2 \tag{C.15}$$

$$\begin{aligned}\langle (J^z)^4 \rangle = {} & 24G_{11}^4 + 24|F_{1-1}|^4 - 48G_{11}^2|F_{1-1}|^2 + 48G_{11}^3 - 48G_{11}|F_{1-1}|^2 \\ & + 26G_{11}^2 + 2G_{11} - 2|F_{1-1}|^2\end{aligned} \tag{C.16}$$

with the usual definition $J^z = a_1^\dagger a_1 - a_{-1}^\dagger a_{-1}$.

Then we can compute the fourth power of J_θ^z:

$$\begin{aligned}(J_\theta^z)^4 = {} & \cos^4\theta\,(J^z)^4 + \sin^4\theta\,(J^y)^4 \\ & + \cos^2\theta\sin^2\theta\,([J^zJ^zJ^yJ^y + J^zJ^yJ^zJ^y + \text{h.c.}] + J^zJ^yJ^yJ^z + J^yJ^zJ^zJ^y)\end{aligned}$$

where we kept only the terms conserving magnetisation (i.e. with en even number of J^y operators). As we can see, we have a zero-th order term in $\cos^4\theta$ that we expect to vanish since we have only zero magnetization states ($J^z = 0$), then a second-order term in $\cos^2\theta\sin^2\theta \sim \theta^2$ that will be our leading term, and finally a fourth order term in $\sin^4\theta \sim \theta^4$ that we will neglect. This gives the following expression at leading order:

$$\mathrm{Var}\left((J_\theta^z)^2\right) = \cos^2\theta\sin^2\theta\langle [J^zJ^zJ^yJ^y + J^zJ^yJ^zJ^y + \text{h.c.}] + J^zJ^yJ^yJ^z + J^yJ^zJ^zJ^y\rangle + O\left(\theta^4\right)$$

which can be rewritten in terms of the second-order correlation functions as follows:

$$\begin{aligned}\frac{\mathrm{Var}\left((J^z_\theta)^2\right)}{\cos^2\theta\sin^2\theta} &= \left(2G_{00}+2|\phi_0|^2+1\right)\left(4G_{11}^2-4|F_{1-1}|^2\right)G_{11}\\ &+\left(G_{00}+|\phi_0|^2\right)\left(12G_{11}^2-4|F_{1-1}|^2+6G_{11}+1\right)+3G_{11}^2+|F_{1\_1}|^2\\ &+8Re\left[\left(\phi_0^2+F_{00}\right)\left(G_{11}^2F^*_{1-1}-|F_{1-1}|^2F^*_{1-1}\right)\right]\\ &+2Re\left[\left(F_{00}+\phi_0^2\right)\left(4G_{11}F^*_{1-1}+F^*_{1-1}\right)\right]+O\left(\theta^2\right)\end{aligned}$$

where we used the usual definition of $J^y=\frac{\sqrt{2}}{2i}\left(a_1^\dagger a_0+a_0^\dagger a_{-1}-a_0^\dagger a_1-a_{-1}^\dagger a_0\right)$.

Finally, we must compute the denominator of $\delta\theta^2$, which is given by:

$$\left(\langle J^z_\theta J^y_\theta\rangle+\langle J^y_\theta J^z_\theta\rangle\right)^2 \tag{C.17}$$

with $J^y_\theta=\cos\theta J^y+\sin\theta J^z$. Again, we will discard all the terms that contains only J^z, or an odd number of J^y terms, which leaves only:

$$\left(-2\cos\theta\sin\theta\langle(J^y)^2\rangle\right)^2=4\sin^2\theta\cos^2\theta\langle(J^y)^2\rangle^2 \tag{C.18}$$

with $\langle(J^y)^2\rangle$ which can be expressed as a function of the correlation functions as follows:

$$\langle(J^y)^2\rangle=2G_{11}\left(G_{00}+|\phi_0|^2\right)+G_{11}+G_{00}+|\phi_0|^2+2Re\left(F^*_{1-1}\left(\phi_0^2+F_{00}\right)\right).$$

With this we have all the ingredients needed to compute the limit value of $\delta\theta^2$ when $\theta\to 0$, and we can compare it to the QFI of the state, which is given by $4\langle(J^x)^2\rangle=4\langle(J^y)^2\rangle$ since we have a $U(1)$ symmetry in the Hamiltonian and in the initial state.